SURFACE PLASMON RESONANCE IMAGING OF METASURFACES PATTERNED VIA PYRAMIDIAL INTERFERENCE LITHOGRAPHY

IMAGERIE PAR RÉSONANCE PLASMONIQUE DE MÉTASURFACES À MOTIFS PAR LITHOGRAPHIE INTERFÉRENTIELLE PYRAMIDALE

A Thesis Submitted to the Division of Graduate Studies of the Royal Military College of Canada by
Saim Bokhari

In Partial Fulfillment of the Requirements for the Degree of Master of Science in Physics

April 3rd, 2025

Acknowledgements

I would like to express my sincere gratitude to Professor Sabat for his invaluable guidance, unwavering support, and dedicated supervision throughout my research, as well as for giving me the opportunity to pursue graduate research under his mentorship. I am also incredibly grateful to Dr. Yazan Bdour for his patience and advice and for teaching me the inner workings of the lab. His support and willingness to lend a helping hand whenever I needed it has made a lasting impact on my learning and growth.

Special thanks to Mr. Pete Snell for manufacturing the custom pyramids, without which this study would not have been possible. I would also like to thank Dr. Olivier Lebel for generously providing the azobenzene material used in the fabrication of the thin films. I am also grateful to Dr. Paul Rochon for clarifying concepts during times of confusion and to Dr. Derek Russell for training me through the sample preparation process and teaching me how to properly spin coat my samples.

Finally, I would like to thank my family and friends for their continued encouragement and support.

Abstract

This study successfully demonstrates, for the first time, surface plasmon resonance (SPR) imaging of plasmonic metasurfaces using the pyramidal interference lithography (PIL) technique. The research focuses on designing, simulating, fabricating, and characterizing metasurfaces with various rotational symmetries. To accomplish this, azobenzene-based thin films were spin-coated onto glass substrates and patterned using PIL, employing pyramids with 3, 4, 6, and 8 faces to generate metasurfaces with corresponding rotational symmetries. Python-based simulations of multi-beam interference were employed to visualize pattern formations that closely resembled the experimental results from PIL. SPR spectrometry revealed distinct plasmonic responses for each metasurface, with observed deviations in SPR wavelengths and pitch values generally within a 10% margin of expected values. Notably, metasurfaces with 6-fold symmetry demonstrated excellent accuracy in the infrared range, with deviations of less than 1%. The study also introduces a dual-pyramid setup capable of generating larger pitch sizes suitable for infrared SPR measurements. In addition, this work developed a lens-pyramid system capable of fabricating metasurfaces with a range of periodicities and demonstrated its capability to achieve this on the micron scale. Overall, this work establishes PIL as a viable technique for fabricating plasmonic metasurfaces that can be imaged through SPR and supports the continued development of SPR imaging and sensing platforms.

Contents

List of Figures

List of Tables

List of Abbreviations

SP	Surface Plasmon
SPW	Surface Plasmon Wave
SPP	Surface Plasmon Polariton
SPR	Surface Plasmon Resonance
SPRi	Surface Plasmon Resonance Imaging
I-SPR	Interrogation Surface Plasmon Resonance
IR	Infrared
NIR	Near Infrared
PC	Photonic Crystal
PQC	Photonic Quasi-Crystal
PIL	Pyramidal Interference Lithography
EOT	Extraordinary Optical Transmission
ACG	Azimuthally Chirped Grating
TPPL	Two-photon photoluminescence
SHG	Second Harmonic Generation
ROI	Region of Interest
PCA	Photoconductive Antenna
TIR	Total Internal Reflection
EBL	Electron Beam Lithography
FIB	Focused Ion Beam Lithography
DUV	Deep Ultraviolet
UV	Ultraviolet
AFM	Atomic Force Microscopy
rpm	Revolutions per minute
FFT	Fast Fourier Transform
MEIRS	Metasurface-Enhanced Infrared Spectroscopy

Chapter 1: Introduction

All physical systems, including those found in nature, have inherent frequencies at which they tend to oscillate—and a collection of unbound, free-moving electrons on a metal surface is no exception. The natural oscillation frequency of free electrons within a conductive medium is called the plasma frequency [1]. When light strikes a conductive surface at frequencies near its plasma frequency, it drives the conduction electrons on the surface to collectively oscillate in resonance with the light's electromagnetic field [1, 2]. These electron oscillations, coupled with the light, effectively confine the electromagnetic energy to the surface [2]. This produces surface-bound electromagnetic waves known as surface plasmons (SPs) [2] , which can be interchangeably called surface plasmon waves (SPWs) [3]. Since these waves combine both light and electron oscillations, they can also be referred to as surface plasmon polaritons (SPPs) [2][3].

The phenomenon by which incident light excites SPWs at a metal-dielectric interface is known as surface plasmon resonance (SPR) [1, 2]. This resulting resonance condition is susceptible to changes in the surrounding refractive index, making it a powerful tool for optical sensing [4] , subwavelength optics [2] and surface-enhanced spectroscopy [5]. The sensitivity to variations in refractive index can be improved using structured surfaces, such as gratings, which provide a means to couple incident light to surface plasmons efficiently [6].

Gratings are periodic structures composed of repeating elements that diffract incident light into multiple orders, producing controlled alterations in its phase and/or amplitude [7]. The periodicity of the grating determines the resonance conditions for various optical phenomena, such as SPR and extraordinary optical transmission (EOT) [8]. Depending on their design, gratings can be used to amplify light-matter interactions. One of the techniques that utilizes amplified interactions due to SPR is called SPR imaging (SPRi).

SPRi utilizes reflected light intensity variations across a surface to detect changes in the refractive index at a metal-dielectric interface [9] . This technique has provided a way to probe nanoscale phenomena, making advancements related to sensing [10, 11] and nanophotonics [12]. This progress has been further propelled by the emergence of metasurfaces — engineered two-dimensional nanostructure arrays [13].

Over the past decade, the development of metasurfaces has expanded the capabilities of SPRi, providing a platform for control over electromagnetic wave propagation, such as demonstrating absorption over the visible spectrum [14] and enhanced biosensing [15, 16]. These metasurfaces, composed of dielectric or metallic nanostructures, manipulate light by inducing phase, amplitude, and polarization shifts at the interface [17, 18]. This allows for novel functionalities for controlling nonlinear optical responses [19], wavefront control for augmented reality [20], and enhanced light scattering [21].

The design of metasurfaces involves patterns in planar configurations and can be fabricated with methods such as lithography [22], pattern transfer [23], and methods involving the direct write approach [24, 25]. Among these methods is the construction of metasurfaces with photonic quasicrystals (PQCs). These patterned surfaces provide additional degrees of freedom in periodic [26, 27] and aperiodic structures [28] to further enhance surface plasmon generation [29]. PCs exhibit a well-defined periodic dielectric function that guides electromagnetic waves [26, 27, 30] while obeying rotational and translational symmetry. Meanwhile, PQCs introduce long-range order without strict periodicity [28], obeying rotational symmetry but not translational symmetry. Given these properties, integrating metasurfaces with SPRi has shown advancements in precision spectroscopy [31], rapid detection of viruses [32], and plasmonic metalenses [33]. However, realizing these capabilities in practical devices may necessitate elaborate fabrication methods.

These advanced functionalities rely on precise nanofabrication—the process of creating nanoscale structures on materials—which requires specialized techniques [34]. Among these is the interference-based fabrication methods, such as the Pyramidal Interference Lithography (PIL) technique, providing a highly precise and scalable approach for structuring metasurfaces [30]. This level of precision in nanofabrication partly depends on the thin films used, which serve as the foundational medium for interference-based lithography.

Thin films serve as the photosensitive or structurally modifiable layer where periodic nanostructures are inscribed and patterned [35, 36]. In some cases, it is possible to achieve sub-wavelength nanostructuring [37]. However, by leveraging interference patterns generated by multiple beams, thin films enable precise patterning with nanoscale resolution [38] and facilitate scalable fabrication of metasurfaces [39].

This thesis investigates the capabilities of the PIL technique in fabricating metasurfaces optimized for SPRi. By leveraging the PIL technique for the development of plasmonic metasurfaces that enable SPR detection, it provides a pathway toward more sensitive and cost-effective imaging technologies. The integration of a light-responsive thin film, in conjunction with the PIL technique, during the fabrication process enables dynamic control over the tunability and optical properties of the metasurfaces, making them suitable for a wide range of applications.

1.1 Grating-Based Plasmonics and Their Applications

Plasmonic gratings are metallic gratings designed to manipulate light through the excitation of SPWs [40]. Diffraction gratings give a compact approach to coupling incident light to surface plasmons for SPR excitation [41]. The operation of plasmonic gratings is presented in Figure 1.

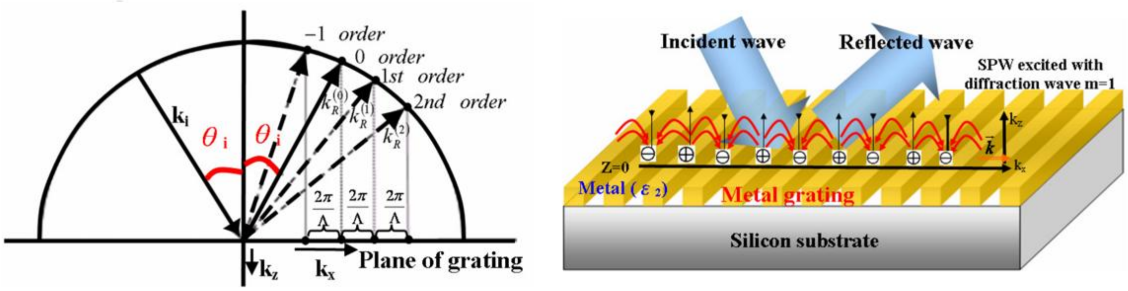

(a) (b)

Figure 1. (a) Illustration of angle formation for higher-order reflections from a grating structure. (b) Representation of surface plasmon wave (SPW) excitation on a metal grating with periodically structured gratings (1D gratings). Adopted from Nan-Fu Chiu [42]

The grating presented in Figure 1(b) consists of periodically structured metallic lines or grooves fabricated onto a dielectric substrate. These structures enable light to diffract into specific orders, providing the necessary in-plane momentum to excite surface plasmons.

The following explores various categories of grating-based plasmonic systems, each playing a distinct role in manipulating SPR phenomena. Amongst them are the one-dimensional plasmonic gratings, as shown in Figure 1, where light is reflected in different orders at an angle θ_i. The electric field of the light is polarized perpendicular to the grooves of the grating. The grating spacing (Λ) allows the momentum vector $\vec{k}_x$, along the plane of the interface, to gain an additional component of magnitude $K = \frac{2\pi}{\Lambda}$ [43]. The periodicity of the grating Λ and angle of incidence determine the resonance condition needed to excite surface plasmons, thus satisfying $k_{spr} = k_x \pm m\frac{2\pi}{\Lambda}$ [1].

Building on the concept of 1D gratings, 2D plasmonic gratings feature periodically arranged nanostructures along both the axes of the grating plane (being the *x* and *y* axes by Figure 1), enabling plasmon propagation in multiple directions along the plane of the gratings and supporting multi-modal SPR [44]. It is important to note, as mentioned in the introduction, that metasurface designs are typically based on planar configurations [22]. As such, two-dimensional plasmonic gratings can also be classified as plasmonic metasurfaces [45]. Furthermore, recent research explores the integration of 2D plasmonic gratings at the rear electrode of thin-film solar cells, demonstrating a high absorption rate as well as an increase in short-circuit current and efficiency through optimized periodicity, width, and depth of the grating structure [46].

Extending the concept of two-dimensional periodicity, another notable class of 2D plasmonic structures is nanohole arrays, which consist of regularly spaced perforations in a metallic film and have been shown to facilitate EOT through SPR [47]. A recent study developed a hybrid optical sensor that combines porous silicon monolayers with plasmonic nanohole arrays, achieving enhanced sensitivity through SPR effects and demonstrating strong potential for label-free detection of toxic substances [48].

Thus far, only cases with constant grating periodicity have been presented. However, the pitch value (Λ) can gradually vary, leading to what are known as chirped gratings—structures where the grating period changes along an axis. In $1D$ chirped gratings, the period varies along a single axis, while $2D$ chirped gratings exhibit variations along two separate axes, producing more complex diffraction patterns and enabling spatially dependent resonance effects. Such structures have been shown to achieve SPR in several different bandwidths [49] as well as broaden the SPR bandwidths [50]. Plasmonic Azimuthally Chirped Gratings (ACGs) extend this concept by introducing a radial variation in grating periodicity, allowing for spatially resolved broadband photon–plasmon coupling [51]. ACGs enhance nonlinear optical processes, such as two-photon photoluminescence (TPPL) and second harmonic generation (SHG) [51].

1.2 Recent Advances in Surface Plasmon Imaging and Metasurfaces

The advancement of metasurfaces has led to innovations and enhancements in plasmonic technologies. Recent studies have demonstrated that ultrathin metasurfaces can amplify SPR signals, improving detection sensitivity in biosensing applications [52]. Under optimized conditions, these enhancements have achieved single-molecule detection, expanding the potential for SPR-based techniques [52]. Furthermore, recent work has focused on overcoming the limitations of noise vulnerability and the narrow range of refractive index changes in traditional intensity-interrogation surface plasmon resonance (I-SPR), a specific method within surface plasmon resonance imaging (SPRi) that directly measures changes in reflected light intensity at fixed angles and wavelengths. In this study, rather than using a fixed wavelength, the system dynamically selects the optimal one for each region of interest (ROI) from a chip located on the sample's refractive index [53]. This system can track changes in refractive index over a much wider range than conventional I-SPR and has demonstrated the capability to detect multiple biomolecules simultaneously. Apart from optimization, research has also been dedicated to advancing the development of metasurfaces for influence over SPRi.

The development of active metasurfaces, which dynamically adjust their optical properties in response to external stimuli, has significantly expanded the functionality of plasmonic devices, unlike passive metasurfaces, whose properties remain fixed by design and material composition [54]. One prominent approach involves flexible substrates that stretch or compress, altering the spacing and coupling strength between nanostructures to tune resonance frequencies [55]. Electrostatic interaction provides another method, where applying a voltage induces displacement in nanostructures, modifying their optical properties [55, 56]. Furthermore, research into disordered metasurfaces and photonic structures has revealed novel light localization effects, extending the capabilities of SPR-based imaging techniques [57]. In addition, some studies have shown that the use of plasmonic gratings can improve interactions across spectral domains other than visible and infrared [58].

Recently, plasmonic grating structures have been explored for optimizing light-matter interactions in terahertz applications. Specifically, integrating a plasmonic grating structure into a large-aperture photoconductive antenna (PCA) resulted in a two-fold enhancement of terahertz radiation intensity compared to conventional designs where the performance increase is attributed to plasmonic effects [58]. Furthermore, the fabrication of two-dimensional gratings on azobenzene thin films demonstrated that their resonance behavior can actively control narrowband transmission peaks, tunable intensity, wavelength, and polarization conversion by external light due to the photomechanical response of the material [18].

Grating-based plasmonic structures and metasurfaces have advanced SPRi through precise control over light-matter interactions and the engineering of periodic patterns. From one-dimensional and two-dimensional gratings to nanohole arrays and chirped-pitch gratings, these innovations have provided advancements in SPR sensitivity, biosensing capabilities, and imaging [52]. Through optimized grating geometries improvements in resonance tuning [10, 11], high-contrast imaging [53] and nonlinear optical effects [19] have been achieved, thereby broadening the applications of SPR-based technologies. As metasurfaces and fabrication techniques continue to evolve, grating-based plasmonics will likely remain integral to the development of next-generation photonic devices.

1.3 Methods for SPR excitation

SPWs cannot be excited by direct illumination on a flat metal-dielectric interface due to the momentum mismatch between incident photons and surface plasmons [1]. To overcome this, various coupling techniques are employed to match the momentum and enable SPR excitation. The most widely used methods include prism coupling—specifically the Kretschmann and Otto configurations—where total internal reflection (TIR) is used to transfer energy to surface plasmons [1]. These two configurations are presented in Figure 2,

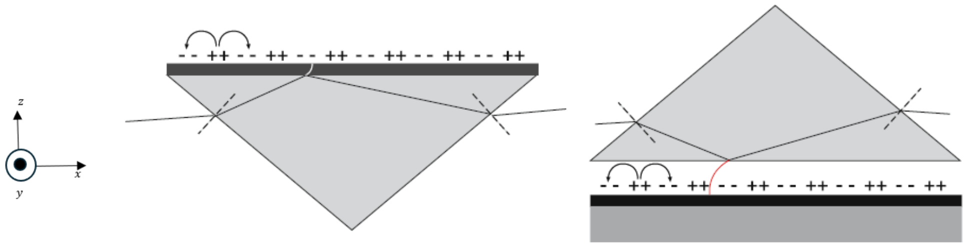

(a) (b)

Figure 2. Illustration of prism coupling method to achieve SPR through TIR in both the Kretschmann (a) and Otto (b) configurations, showing the light path for excitation of SPR adopted from Maier [1].

The Kretschmann configuration, presented in Figure 2 (a), depicts a thin metal film on a prism with a high index of refraction. Light is directed through the prism in its transverse magnetic mode, or P-polarized light (with the magnetic field vector pointing towards the y-axis), and undergoes TIR at the metal-dielectric interface [1]. At a critical angle of incidence, the electric field extends into the metal during TIR, and light traveling parallel to the interface matches the momentum of the surface plasmon wave [1]. This results in a dip in the reflected light intensity, indicating SPR coupling [1].

The Otto configuration, shown in Figure 2 (b) is another prism-based method for SPR excitation. Unlike the Kretschmann setup, the metal film is not in direct contact with the prism. Instead, a thin air gap separates the prism from the metal surface [1]. P-polarized light undergoes total internal reflection within the prism, generating an evanescent wave that decays through the air gap and interacts with the metal surface [1]. When the wave vector of this evanescent field matches that of the surface plasmons, it satisfies the resonance condition for SPR. The Otto configuration allows for the study of interfaces without direct contact between the prism and the metal [1].

Beyond prism coupling, the grating coupling method introduces a periodic structure, such as a grating, on the metal surface the operations of which were presented in section 1.1. However, one thing to note is that SPWs along a structured surface could also couple back into free-space radiation, transferring that energy as photons of light [1]. This can be captured as peaks, instead of dips, in light intensity. This will be an important part of carrying out some of the experiments in this thesis.

1.4 Azobenzene Thin Films

One of the tools used for fabricating nanoscale plasmonic gratings involves the use of azobenzene-based thin films. Azobenzene is a light-sensitive material that can change shape when exposed to light [59]. When azobenzene molecules are hit with specific wavelengths of light, such as one produced from a laser, they undergo a reversible transformation between two configurations—called trans and cis—isomers [59]. These two configurations are presented in Figure 3.

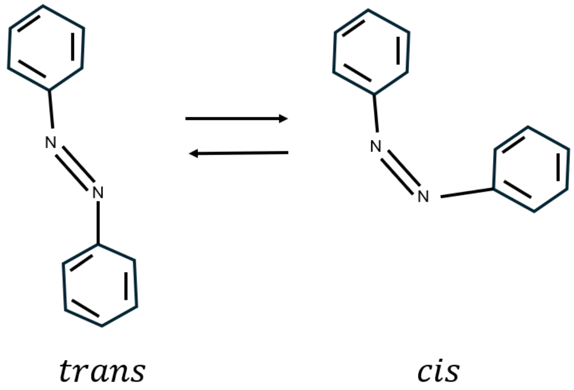

Figure 3.illustration of Isomers of azobenzene

This change in shape causes a physical movement within the material, which can lead to a shift in surface structure [60, 61]. When azobenzene is deposited as a thin film on a surface, this property can be used to pattern structures on the films[61]. One important application of this technique is in the fabrication of gratings and metasurfaces.

With azobenzene-based thin films, gratings can be created by interfering with two or more laser beams on the surface. The interference pattern creates alternating regions of light and dark, and the azobenzene responds by rearranging its molecules to form a pattern that mimics this light distribution. As a result, gratings or metasurfaces are formed directly on the film without needing any etching or physical photomasks [30], which are transparent plates with opaque patterns to block or transmit light in specific areas [62].

Azobenzene-based grating structures are especially useful in optics and plasmonics because they offer precise control over feature size and shape [39]. Moreover, the process is reversible, meaning the grating can be erased and rewritten, allowing for dynamic or reconfigurable optical elements [63] .

1.5 Pyramidal Interference Lithography (PIL) technique for Metasurface Fabrication

Conventional methods, such as electron beam lithography (EBL) and focused ion beam lithography (FIB), are widely used for microfabrication due to their ability to create precise patterns at the micro- and nanoscale. These techniques have demonstrated advancements in high throughput for large-area nanostructuring [64], multiscale fabrication of integrated photonic chips [65], and deterministic defect creation in silicon carbide for quantum applications [66]. These techniques are also instrumental in the fabrication of photonic crystals [67]. However, their reliance on sequential patterning and stitching processes can be time-consuming, especially when dealing with large areas for patterning. Furthermore, sequential inscription and overlay of patterning can damage and create errors in the fabricated structures [68]. Additionally, the high cost of exposure tools and masks makes these methods economically viable only for large-scale production.

Both prisms and phase masks can be used to generate interference patterns, but these techniques operate through different mechanisms. Prisms function by redirecting and splitting coherent light beams at specific angles, allowing the beams to overlap and form periodic interference fringes [69]. This approach enables precise control over the spacing of the resulting pattern based on the beam angle [69]. In contrast, phase masks use variations in thickness or refractive index to introduce phase shifts in a single incident beam, creating self-interference without the need for multiple beam paths [70].

Interference lithography is a method for fabricating periodic nanoscale structures without requiring complex photomasks or direct-write techniques [71]. Multi-beam interference lithography operates by splitting a large-diameter collimated laser beam into multiple coherent wavefronts using transmission phase masks [72]. The interaction of these beams creates a structured interference pattern, with the resulting periodic features determined by the design and orientation of the phase mask [72]. One of the key innovations in this field is Pyramidal Interference Lithography (PIL), which employs pyramidal prisms to generate multiple interference beams, and enable the fabrication of highly ordered 2D nanostructures [71]. Compared to the mask-based lithography, PIL offers a scalable and cost-effective approach for producing metasurfaces with nanoscale features [71].

PIL is an extension of multi-beam interference lithography, where a collimated laser beam is directed onto a pyramidal prism. The portion of the prism refracts the incoming beam, generating multiple wavefronts that interfere constructively and destructively, producing a high-contrast intensity pattern [69]. This interference pattern is recorded onto a photosensitive material (such as Azobenzene) and can be used to fabricate nanoscale photonic crystal structures to produce metasurfaces [73]. During laser inscription, the resulting patterns have rotational symmetry, which depend on the number of pyramid faces used [30]. Compared to conventional biprism-based methods, the pyramidal prism-based approach offers larger-area patterning with a reduced number of required optical components, making it highly suitable for metasurface fabrication [74, 75]. Experimental studies have demonstrated the ability to fabricate structures with pitch sizes below 500 nm using deep ultraviolet (DUV) light sources and pyramidal prisms with edge angles of 30.4° [71]. Holes with diameters around 187 nm and periodicities of 414 nm were successfully fabricated using a 266 nm UV laser and a fused silica prism [71].

1.6 Motivation and Significance of Research

The significance of this thesis is in its potential to bridge the gap between traditional nanofabrication methods and scalable, high-throughput techniques for metasurface production. By demonstrating a scalable approach for fabricating large-area plasmonic structures with fine control over their optical properties, this research will contribute to the advancement of SPR imaging. The ability to control plasmonic resonances has implications for biomedical diagnostics [76], environmental monitoring [77], and optical computing [78]. This research aims to deepen the understanding of light-matter interactions at the nanoscale, by investigating the interplay between SPR and engineered metasurfaces, furthering the development of next-generation photonic technologies. This thesis presents a comprehensive study on the fabrication of plasmonic metasurfaces using the PIL technique and, for the first time, investigates the SPR imaging of PIL-fabricated plasmonic metasurfaces. Integrating simultaneous multi-beam interference lithography with SPR spectroscopy and imaging, could pave the way for new plasmonic sensors and imaging systems, contributing to the broader field of nanophotonics. The following chapters will provide an in-depth analysis of the theoretical framework, fabrication processes, and experimental methodologies underlying this research.

1.7 Structure of Thesis

This thesis is structured into five main chapters. Chapter 2 delves into the theoretical framework, beginning with the dispersion relation for surface plasmon waves and progressing through related concepts such as irradiance, Malus’s Law, and multi-beam interference. This chapter also includes mathematical modeling for grating-based SPR coupling and detailed ray tracing analyses for various PIL configurations—single pyramid, dual pyramid, and lens-pyramid systems—highlighting their role in patterning periodic structures with tunable pitch sizes.

Chapter 3 focuses on the experimental procedures, describing the materials and methods used for nanofabrication, including fabrication of pyramids, spin-coating of azobenzene films, laser inscription using PIL technique, and subsequent gold deposition. It also covers the techniques used to measure the depth and pitch of the metasurfaces as well spectrometry.

Chapter 4 presents the spectrometry results obtained from metasurfaces patterned with different rotational symmetries, including 3-fold, 4-fold, 6-fold, and 8-fold. The results also show the SPR imaging for metasurfaces produced through PIL technique exhibiting 3-fold and 4-fold rotational symmetry. Furthermore, each structure's SPR characteristics are discussed and compared with expected values. Lastly, the effectiveness of PIL techniques in producing a metasurface of different pitch sizes is evaluated.

Chapter 5 concludes the thesis by summarizing key findings and proposing directions for future research.

Chapter 2: Theoretical Overview and Mathematical Modelling

2.1 Dispersion relation

As mentioned in Chapter 1, surface plasmon resonance (SPR) occurs at the metal-dielectric interface when incident light, under specific conditions, excites collective oscillations of free electrons on the metal's surface [1] . These oscillations are confined to the dielectric-metal interface and propagate along it, decaying exponentially perpendicular to the surface, [1] as shown in Figure 4,

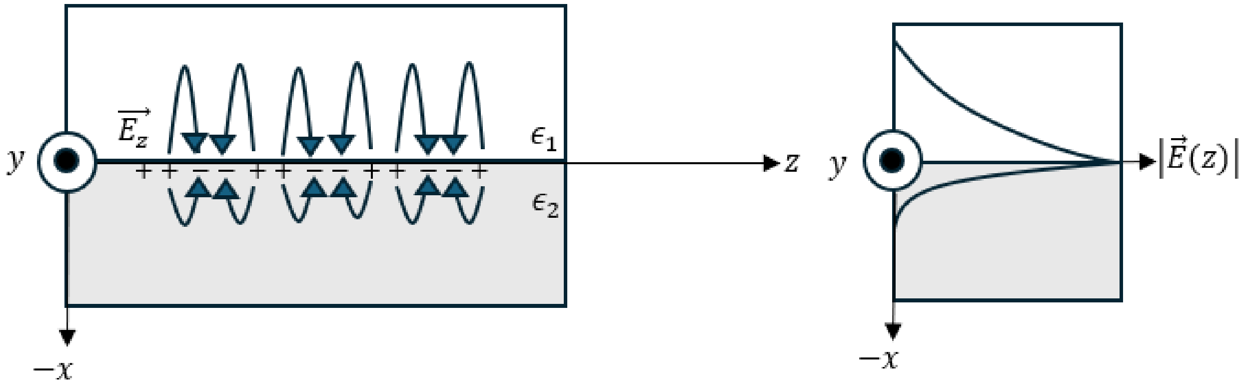

Figure 4. (a) Surface plasmon wave (b) Electric field amplitude near the surface.

The dispersion equation for surface plasmon waves describes the relationship between their frequency and wavevector, showing how these waves propagate along a metal-dielectric interface.

The in-plane momentum for SPW along the metal-dielectric interface (on the z axis) can be expressed with the generalized dispersion equation [1]:

$$k_z = k_{SPW} = \sqrt{\frac{k_0^2(\epsilon_{\mathrm{r},1}\epsilon_{\mathrm{r},2})}{\epsilon_{r,2}^2 - \epsilon_{r,1}^2}(\epsilon_{r,2}u_{r,1} - \epsilon_{r,1}u_{r,2})} \tag{1}$$

Here $\epsilon_{\mathrm{r},1}$ and $\epsilon_{\mathrm{r},2}$ are the electric permittivity for the dielectric and metal respectively, while $u_{r,1}$ and $u_{r,2}$ are the magnetic permittivity. It is important to note that k_o represents the momentum of incident light. Since the experimental format deals with gold as the metallic layer and air as the dielectric medium, both of which are non-magnetic, then $u_{r,1} = u_{r,2} = 1$. The dispersion equation (1) reduces to the following [1, 79]:

$$k_z = k_{SPW} = k_o\sqrt{\frac{(\epsilon_{\mathrm{r},1}\epsilon_{\mathrm{r},2})}{(\epsilon_{\mathrm{r},2} + \epsilon_{\mathrm{r},1})}} \tag{2}$$

It reveals that surface plasmons have higher momentum than incident light on the metal-dielectric interface, which is why special coupling methods are needed to excite them [1] . To further elaborate, this is considering the terms in front of k_o is greater than 1 the experimental determination of which is discussed in section 2.4. Substituting $k_o = \frac{\omega}{c}$, where ω is the light frequency and c is the speed of light, into (72) yields:

$$k_{SPW} = \frac{\omega}{c}\sqrt{\frac{(\epsilon_{\mathrm{r},1}\epsilon_{\mathrm{r},2})}{(\epsilon_{\mathrm{r},2} + \epsilon_{\mathrm{r},1})}} \tag{3}$$

It is important to note that $\epsilon_{\mathrm{r},2}$ is a complex quantity, which in turn makes the surface plasmon wavevector k_{SPW} complex [79]. As result, SPWs experience energy loss as they propagate, with their intensity diminishing over a characteristic distance known as the propagation length [79]. For metal-dielectric interfaces in the visible range, this length falls between 10 and 100 microns [79].

2.2 Irradiance and Malus's Law

Since the momentum vectors are not directly measured by instruments, it is useful to understand how light irradiance, sometimes referred to as intensity, can be modelled mathematically as the experimental observations rely on the irradiance of a given beam interacting with a surface. This can be done using Maxwell's equations in frequency space, with no free currents. Under these conditions, according to electromagnetic wave theory the electric field component E_x and magnetic field H_y component can be expressed as the following [80, 81]:

$$k_z H_y = -\epsilon_0 \epsilon_r \omega E_x \tag{4}$$

Here ϵ_0 is the permittivity of free space and ϵ_r is the relative permittivity. As such, k_z can be expressed as [80, 81]:

$$k_z = \frac{2\pi}{\lambda} = \frac{n\omega}{c} \tag{5}$$

Where, λ is the wavelength. By substituting (5) into (4) and assuming vacuum conditions with $n = 1$ and $c = \frac{1}{\sqrt{u_0\epsilon_0}}$ yields [80, 81]:

$$H_y = -\sqrt{\frac{\epsilon_0\epsilon_r}{u_0}} E_x \tag{6}$$

Here u_0 is the permeability of free space. Taking the magnitude of the ratio of $\frac{E_x}{H_y}$ the following expression is obtained [80, 81]:

$$H_y = \sqrt{\frac{u_0}{\epsilon_0\epsilon_r}} E_x = \frac{1}{Z} E_x \tag{7}$$

Where $Z = \frac{1}{\sqrt{\frac{u_0}{\epsilon_0 \epsilon_r}}}$ is the impedance. The instantaneous energy flow in an electromagnetic wave can be calculated from the pointing vector $\vec{S}$ [81].

The Poynting vector $\vec{S}$ is defined as the cross product of the electric field $\vec{E}$ and the applied magnetic field $\vec{H}$ as follows [80, 81],

$$\vec{S} = \vec{E} \times \vec{H} \tag{8}$$

thus, carrying out the cross-product for the Poynting vector gives the following,

$$\vec{S} = \vec{E} \times \vec{H} = \begin{vmatrix} \hat{x} & \hat{y} & \hat{z} \\ E_x & 0 & 0 \\ 0 & \frac{1}{Z} E_x & 0 \end{vmatrix} = \frac{1}{Z}(E_x)^2 \tag{9}$$

Since electromagnetic waves oscillate sinusoidally in time, the Poynting vector $\vec{S}$ also exhibits time-dependent oscillations [80, 81]. Measuring its instantaneous value is impractical; therefore, the time-averaged Poynting vector is computed over a full oscillation cycle as [80, 81]:

$$\langle \vec{S} \rangle = \frac{1}{T} \int_0^T \vec{S}(t)\, dt \tag{10}$$

Taking time average of the Poynting vector by substituting equation (9) into (10), the following is obtained [81]:

$$\langle |\vec{S}| \rangle = \frac{1}{Z} \langle (E_x)^2 \rangle_{rms} = \frac{1}{Z} \langle |\overrightarrow{E_x} \cdot \overrightarrow{E_x}| \rangle = \frac{(E_x)^2}{2Z} = \frac{1}{2}\, c\epsilon_0 n (E_x)^2 \tag{11}$$

Where $\langle (E_x)^2 \rangle_{rms}$ represents the root-mean-square of the electric field. The time-averaged Poynting vector, demonstrates that the irradiance I is proportional to the square of the amplitude [81]. Thus,

$$I = \frac{(E_x)^2}{2Z} \tag{12}$$

It is important to note that irradiance quantifies the radiant flux density $(\frac{W}{cm^2})$ incident on or exiting from a surface [7, 80, 81]. It can be expressed as the following:

$$I = \langle |\vec{S}| \rangle \cos(\beta) \tag{13}$$

Where β represents the angle between the beam incident on the surface and the vector normal to the surface.

Irradiance plays a crucial role in optical polarizers, as the transmission of already polarized light depends on the angle between the light's electric field and the polarizer's transmission axis [7, 80, 81]. This is represented in the following figure,

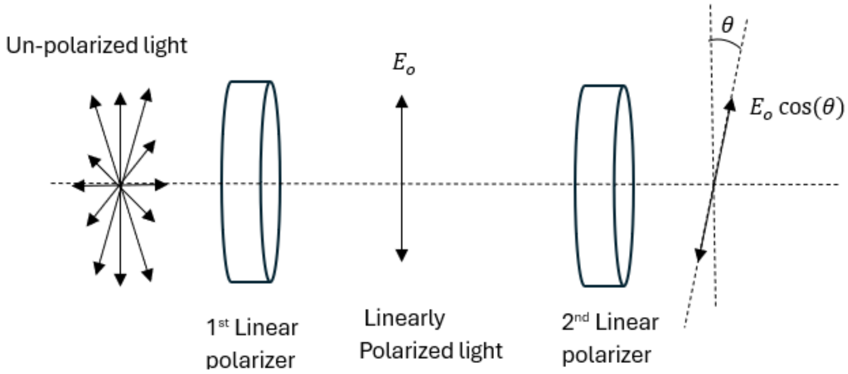

Figure 5. Malus's law for linearly polarized light.

Referring to Figure 5, unpolarized light becomes linearly polarized after passing through the first polarizer. If the amplitude of the electric field of the polarized light is represented as E_O , then after passing through the second polarizer, its amplitude is given by the projection of E_O onto the polarizer's transmission axis, ($E_O\cos(\theta)$) [7]. Substituting this projected amplitude into Equation (11) yields the result known as Malus's law [7, 80, 81]:

$$I = \langle|\vec{S}|\rangle = \frac{1}{2}c\epsilon_0 n(E_o\cos(\theta))^2 \tag{14}$$

It is important to notice that under $\theta = \frac{m\pi}{2}$, where m are all odd integer values, there should be no light. This will be important part of the experimental set-up dealing with crossed polarizers.

2.3 Two beam and multi-beam interference

The following section provides insight into how irradiance is affected when multiple light beams interfere. Figure 6 shows 2 beams incident on a surface,

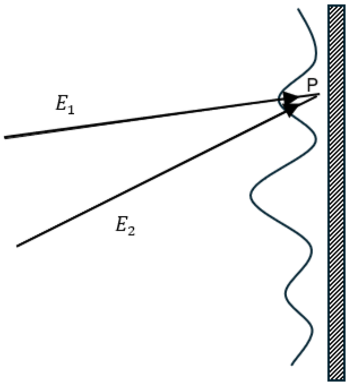

Figure 6. Two beam interference

In Figure 6, two plane waves intersect at a point P, with one wave having a phase difference of ϕ. The equation for the two-plane waves E_1 and E_2 is shown below:

$$E_1 = E_1 e^{i(k \cdot x - \omega t)} \tag{15}$$

$$E_2 = E_1 e^{i(k \cdot x - \omega t + \phi)} \tag{16}$$

As such the total electric field E_{total} can be expressed as the following,

$$\begin{aligned} E_{total} &= E_1 e^{i(k \cdot x - \omega t)} + E_2 e^{i(k \cdot x - \omega t + \phi)} = e^{i(k \cdot x - \omega t)}\left(E_1 + E_2 e^{i\phi}\right) \\ &= |E_T| e^{i(k \cdot x - \omega t)} \end{aligned} \tag{17}$$

Here the resultant amplitude of the total electric field is defined as $|E_T|$,

$$|E_T| = (E_1 + E_2 e^{i\phi}) \tag{18}$$

To determine the amplitude, the modulus is expanded using the complex conjugate, leading to the following expression:

$${E_T}^2 = \left(E_1 + E_2 e^{i\phi}\right)\left(E_1 + E_2 e^{-i\phi}\right) = (E_1)^2 + (E_2)^2 + E_1 E_2 (e^{i\phi} + e^{-i\phi}) \tag{19}$$

Applying the complex identity [1]:

$$\frac{e^{i\phi} + e^{-i\phi}}{2} = \cos(\phi) \tag{20}$$

This yields the following:

$$E_T{}^2 = (E_1)^2 + (E_2)^2 + 2E_1E_2\cos(\phi) \tag{21}$$

Furthermore, the proportionality relationship from equation (12) can be expressed as the following:

$$2ZI = (E_x)^2 \tag{22}$$

Now, substituting (22) into (21) simplifies the equation to:

$$E_T{}^2 = 2ZI_1 + 2ZI_2 + 2Z\sqrt{I_1I_2}\cos(\phi) \tag{23}$$

Thus, yielding the final expression for total irradiance [82]:

$$I_T = \frac{E_T{}^2}{2Z} = I_1 + I_2 + \sqrt{I_1I_2}\cos(\phi) \tag{24}$$

From this expression it can be noticed that depending on the phase ϕ, the irradiance will oscillate according to the cosine term between maximum and minimum values. If the two beams are of the same irradiance where $I_1 = I_2$ and $\phi = \frac{m\pi}{2}$ (where m are all odd integer values) this would result in complete destructive interference. Thus, scanning through all possible values of ϕ results in an interference pattern with dark and bright fringes. Furthermore, two beam interference can be extended to multiple beams. Although difficult to visualize, simulated images of interference patterns under special conditions are presented in Figure 7.

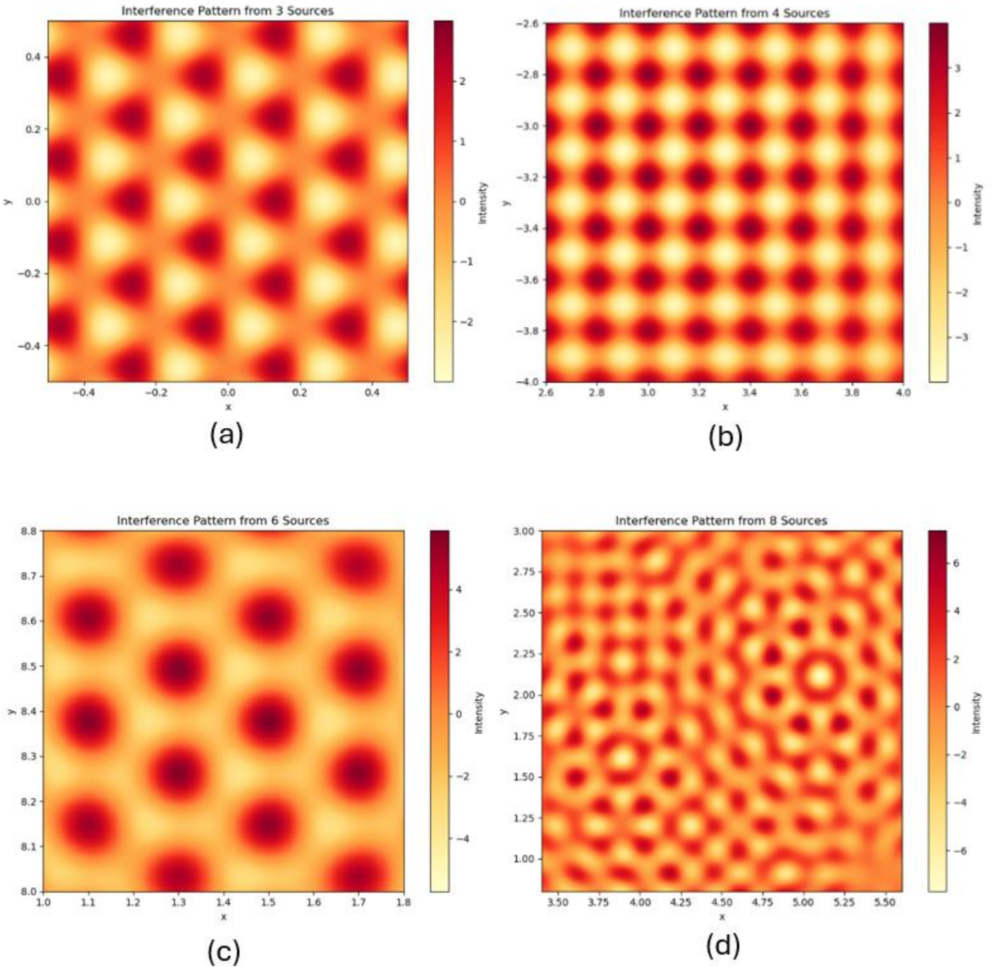

Figure 7. Interference patterns generated from coherent point sources. (a) 3-point source, (b) 4-point source, (c) 6-point source and (d) 8-point source.

To better understand and visualize the principles behind multi-beam interference patterns observed in PIL, the interference simulations presented in Figure 7 were carried out using Python. These simulations assumed multiple point sources evenly spaced along a circular perimeter. The result was a series of intricate two-dimensional interference patterns created by the constructive and destructive interference of circular wavefronts emitted by each source (code provided in Appendix). Interestingly, as the number of sources increased, the resulting interference patterns began to exhibit recognizable patterns—such as triangular patterns with three sources showing in Figure 7(a), square-like forms with four sources showing in Figure 7 (b), and more complex symmetries for higher numbers of sources. Specifically, a long-range order can be observed with 8-point sources shown in Figure 7(d). Studies have shown similar symmetries observed in PC structures and PQC structures fabricated using PIL on thin films as well as comparison of their work with similar simulations [30] [83].

2.4 Plasmonic Gratings

As mentioned in section 2.1 surface plasmons have higher momentum than incident light and require special coupling methods to excite them [1]. The grating coupling which provides a compact approach to couple light with SPWs [41]. The following will go over the mathematical modelling of this method.

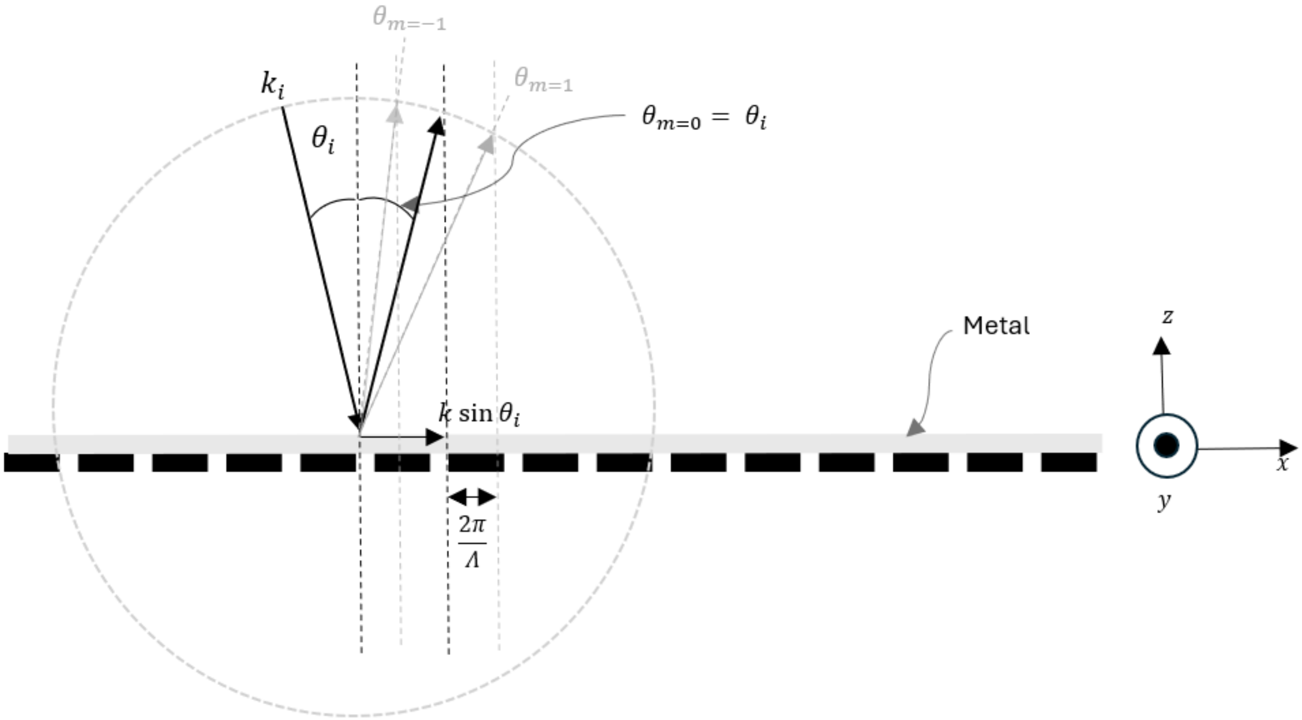

Figure 8. Plasmonic Gratings

As it can be seen from Figure 8, when a plane wave hits the grating structure at an incident angle θ_i with respect to the normal of the surface, its wavevector k can be decomposed into its component parallel to the grating surface for both the incident light $k_{x,i}$ and reflected light $k_{x,m}$ as the following [1, 84]:

$$k_{x,i} = k_0 \sin\theta_i \tag{25}$$

$$k_{x,m} = k_0 \sin\theta_m \tag{26}$$

Where k_0 is the momentum for incident light in free space and θ_m is the angle for the order of reflected light after it hits the grating. The spatial frequency component of the grating's periodic structure can be modeled as the following [1]:

$$mK = \frac{m2\pi}{\Lambda} \tag{27}$$

Where m is the reflection order, and Λ is the pitch of the grating. Since the momentum is conserved, in order for a shift in angle to take place, it must be transfer parallel to the plane yielding [85]:

$$k_{x,i} = k_{x,m} \pm mK \tag{28}$$

Where the $\pm$ covers the range for the order of reflection, where m can take positive or negative integer values. This means that additional in-plane momentum results from the grating's periodic structure. To excite the surface plasmon wave on the interface, the in-plane momentum $k_{x,i}$ should match the surface plasmon wave momentum k_{SPW}, thus the following equivalency can be made [1, 84-86]:

$$k_{x,i} = k_{SPW} \tag{29}$$

$$k_{SPW} = k_0 \sin\theta_i \pm m\frac{2\pi}{\Lambda} \tag{30}$$

Substituting equation (2) into (30) gives the following [85],

$$k_o\sqrt{\frac{(\epsilon_{\mathrm{r},1}\epsilon_{\mathrm{r},2})}{(\epsilon_{\mathrm{r},2}+\epsilon_{\mathrm{r},1})}} = k_0 \sin\theta_i \pm m\frac{2\pi}{\Lambda} \tag{31}$$

Expressing the equation in its spatial domain, where $k_0 = \frac{2\pi}{\lambda_{SPR}}$ yields:

$$\frac{2\pi}{\lambda_{SPR}}A = \frac{2\pi}{\lambda_{SPR}}\sin\theta_i \pm m\frac{2\pi}{\Lambda} \tag{32}$$

Where A is defined as the following:

$$A = \sqrt{\frac{(\epsilon_{\mathrm{r},1}\epsilon_{\mathrm{r},2})}{(\epsilon_{\mathrm{r},2}+\epsilon_{\mathrm{r},1})}} \tag{33}$$

This defined value for A is done for mathematical convenience to help keep track of algebraic manipulation when solving for λ_{SPR}.

Solving for λ_{SPR} :

$$\frac{1}{\lambda_{SPR}}A - \frac{1}{\lambda_{SPR}}\sin\theta_i = \pm m\frac{1}{\Lambda} \tag{34}$$

$$\frac{\Lambda}{m}\left(\frac{1}{\lambda_{SPR}}A - \frac{1}{\lambda_{SPR}}\sin\theta_i\right) = \pm\lambda_{SPR} \tag{35}$$

$$\frac{\Lambda}{m}(A \mp \sin\theta_i) = \lambda_{SPR} \tag{36}$$

Substituting equation (33) into (36) and restricting the reflection orders to $m = \mp 1$, yields the following [1]:

$$\lambda_{SPR} = \Lambda\left(\sqrt{\frac{(\epsilon_{\mathrm{r},1}\epsilon_{\mathrm{r},2})}{(\epsilon_{\mathrm{r},2} + \epsilon_{\mathrm{r},1})}} \mp \sin\theta_i\right) \tag{37}$$

For cases where incident light is at normal to the planer surface ($\theta_i = 0$), (37) reduces to the following [1]:

$$\lambda_{SPR} = \Lambda\left(\sqrt{\frac{(\epsilon_{\mathrm{r},1}\epsilon_{\mathrm{r},2})}{(\epsilon_{\mathrm{r},2} + \epsilon_{\mathrm{r},1})}}\right) \tag{38}$$

Recalling , the dielectric permittivity can be expressed as [1]:

$$n_{r,1} = \sqrt{\epsilon_{\mathrm{r},1}} \tag{39}$$

Substituting (39) into (38) yields the following [1] :

$$\lambda_{SPR} = \Lambda n_{r,1}\left(\sqrt{\frac{(\epsilon_{\mathrm{r},2})}{(n_{r,1}^2 + \epsilon_{\mathrm{r},1})}}\right) \tag{40}$$

It is important to note that Equations (38) and (40) will be used in Chapter 4 to compare the expected values with the experimentally obtained results. For the purposes of this thesis, the calculation of the SPR wavelength, λ_{SPR}, is based on known permittivity values for the metal and surrounding dielectric. Specifically, established permittivity values for gold [87] and air [88] are used to determine the proportionality constant between the grating pitch and the SPR wavelength. Substituting the referenced permittivity values in equation (33), this proportionality constant is calculated to be 1.064620562. However, it is important to mention that this value would change if a different metal was used instead of gold and would lead to different predictive values for the SPR wavelength. Furthermore, it should be considered from equations (38) and (40) that while this theoretical model accurately predicts the SPR wavelength, it does not provide any information regarding the intensity of the SPR response.

2.3 Ray tracing for pyramidal interference lithography (PIL)

As mentioned in Pyramidal Interference Lithography (PIL) offers an alternative approach to conventional nanofabrication techniques, distinguished by simultaneous patterning of an entire surface [89]. This section will focus on the mathematical modeling of the PIL techniques using ray tracing. Specifically, the examination of the way PIL functions with a collimated laser beam and how different pyramid configurations can achieve specific pitch sizes—eliminating the need to fabricate new pyramids for each desired pitch. Furthermore, a model for lens-pyramid system is developed to provide further flexibility in achieving various pitch sizes without requiring new pyramid structures. Although the analysis here considers a simple case, involving a Fresnel biprism consisting of only two faces, the model can be extended to multifaced pyramids.

2.3.1 PIL using Fresnel's biprism

Fresnel's biprism consists of two thin prisms joined at their bases, creating an isosceles triangular structure [90]. A ray of light enters the biprism at an arbitrary incident angle θ , passing through a medium of the prism with an index of refraction n_2 and a slope angle α from the base, as illustrated in Figure 9,

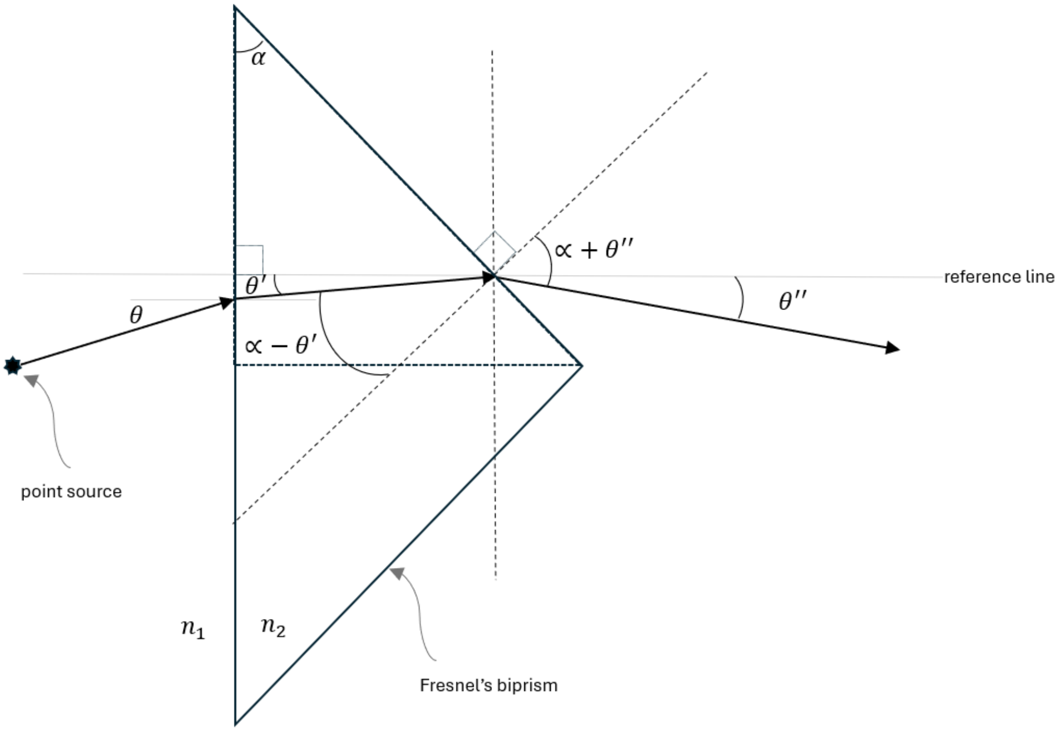

Figure 9. Ray tracing for a Fresnel's biprism

Where n_1 represents the index of refraction for the medium outside the prism, then the ray passing from the outside medium to the medium inside the prism is modeled using Snell's law [7]

$$n_1\, sin(\theta) = n_2\, sin(\theta') \tag{41}$$

From which the refracted angle θ' is expressed as the following,

$$\theta' = sin^{-1}\left(\frac{n_1}{n_2} sin(\theta)\right) \tag{42}$$

As the ray exits the prism and re-enters the surrounding environment, the normal to the interface shifts by an angle α. This change allows for the evaluation of θ'' based on the new geometry:

$$n_2\, sin(\propto -\theta') = n_1\, sin(\propto \pm \theta'') \tag{43}$$

The $\pm$ symbol indicates whether θ' is positioned above or below the reference line. The (-) sign applies when θ' is above, while the (+) sign is used when it is below. This distinction depends on the refractive index of the surrounding medium n_1. Solving for θ'' yields the following,

$$\theta'' = sin^{-1}\left(\frac{n_2}{n_1} sin(\alpha - \theta')\right) \pm \alpha \tag{44}$$

Substituting (42) into equation (44) expresses the equation in terms of θ as:

$$\theta'' = sin^{-1}\left(\frac{n_2}{n_1} sin\left(\alpha - \ sin^{-1}\left(\frac{n_1}{n_2} sin(\theta)\right)\right)\right) \pm \alpha \tag{45}$$

For experiments where the surrounding medium is air, it is assumed that $\mathrm{n_1} < \mathrm{n_2}$ then $\theta' < \theta$. This is a reasonable assumption since the index of refraction for air under standard temperature and pressure (STP) is very close to 1 ($\mathrm{n_{air}} = \frac{c}{v_{air}} = 1.000273$) [91]. Approximating that $n_{air} = n_1 \approx 1$, the equation simplifies to the following:

$$\theta'' = sin^{-1}\left(n_2\, sin\left(\alpha - \ sin^{-1}\left(\frac{1}{n_2} sin(\theta)\right)\right)\right) \pm \alpha \tag{46}$$

Further if the light ray from the source entered the base of the prism is at normal to the interface would mean $\theta = 0^o$, as such the equation would simplify further as shown below,

$$\theta'' = \sin^{-1}(n_2\, sin(\alpha)) \pm \alpha \tag{47}$$

This is a reasonable assumption undertaken for this research, since the experiment entails a collimated laser beam which inherently low divergence and high directionality [92]. This will simplify the $\pm$ sign to being only negative since transitioning from higher to lower refractive index medium will yield refraction away from the normal and thus below the reference line shown in figure 9. Following these assumptions would simplify (47) to [69]:

$$\theta'' = \sin^{-1}(n_2\, sin(\alpha)) - \alpha \tag{48}$$

In circumstances where α is small $(\alpha \ll 10^o)$ and that $|n\alpha| \ll 1$, assuming the index of refraction for the biprism is of reasonable value, then the equation can reduce to [69]:

$$\theta'' = (n_2 - 1)\alpha \tag{49}$$

Where the inverse trigonometric term $(\sin^{-1}(n_2\, sin(\alpha))$ is approximated using Taylor series expansion, neglecting the cubic term in the expansion polynomial [93]. Notice that this equation provides a linear relationship, a theoretical comparison of the refracted angle is presented in figure 10:

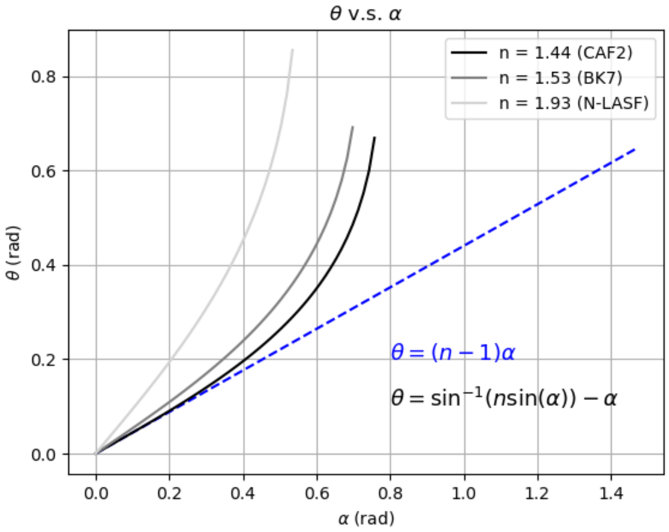

Figure 10. Simulated dependency of refracted angle θ over base angle α for 3 different glass materials. The blue dashed line shows the linear dependency for an index of refraction value of 1.44.

From figure 10 the linear model works well for small base angles α, however for larger values of α the model starts diverging exponentially, for which equation (49) is no longer a reasonable approximation [69]. In such a case, the use of equation (48) is needed for more accurate predictions for the refractive angle θ [69]. Furthermore, additional information can be gained about the diffraction pattern by accessing for the wavefront passing through the prism. When a single wavefront encounters the Fresnel's biprism, its top half refracts down while the bottom half refracts to the top. This causes the two refracted wavefronts to overlap, creating a region where their superposition leads to an interference pattern, as if they originated from two virtual sources [90]. This is shown in the Figure 11,

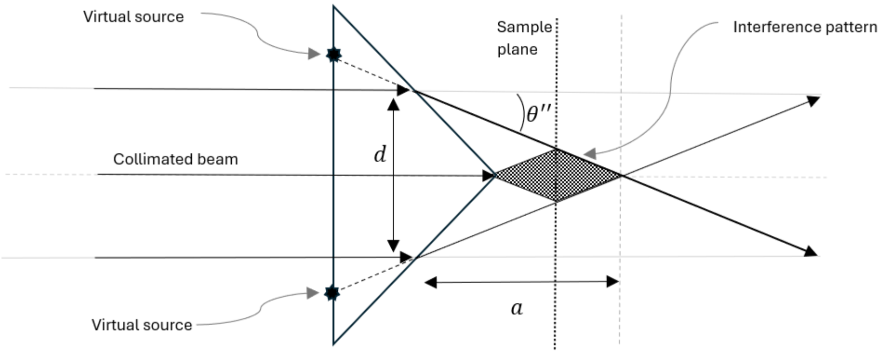

Figure 11. Region of Interference generated from a Fresnel's biprism for a collimated beam passing through a pyramid.

The wavevectors of the two beams have components along the sample plane, the in-plane component of each wavevector is illustrated below,

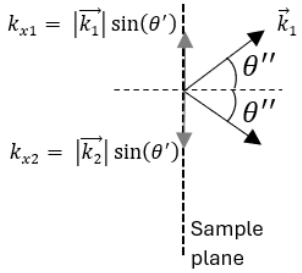

Figure 12. Wavevectors on a point in the sample plane.

In Figure 11 and Figure 12 it should be noted that the sample plane is parallel to the base of the prism and situated in the interference region. The periodicity of the interference fringes is determined by the spatial frequency projected along the sample, which is given by adding the magnitudes of the wavevector components of the two beams. Recognizing that [84]:

$$k_{x1} = k_{x2} = k = \frac{2\pi}{\lambda}\sin(\theta') \tag{50}$$

The components can be added up as presented below [84]:

$$k_{x1} + k_{x2} = \frac{2\pi}{\lambda}\sin(\theta'') + \frac{2\pi}{\lambda}\sin(\theta') = \frac{4\pi}{\lambda}\sin(\theta'') \tag{51}$$

The interference pattern on the sample plane is a result of the path difference, or phase shift, between the two projected waves. The resulting spatial period of the interference pattern is the pitch (Λ) which can be expressed as the following:

$$\frac{4\pi}{\lambda}\sin(\theta'') = \frac{2\pi}{\Lambda} \tag{52}$$

Leading to the pitch equation as shown [69]:

$$\Lambda = \frac{\lambda}{2\sin(\theta'')} \tag{53}$$

Substituting equation (48) into equation (53), gives the spatial period of the interference fringes Λ as [69]:

$$\Lambda = \frac{\lambda}{2\sin(\sin^{-1}(n_2\,sin(\alpha)) - \alpha)} \tag{54}$$

2.3.2 Ray tracing for PIL using dual-pyramid configuration

Equation (54) shows that achieving interference fringes of a specific pitch requires a dedicated pyramid. Fabricating a new pyramid for each pitch variation increases both time and cost. Greater flexibility can be introduced by combining two pyramids, producing pitch sizes that one of the two pyramids alone cannot produce. The following analysis examines ray tracing for this dual-pyramid configuration. Consider two Fresnel biprisms, each with a different slope angle α, aligned along the same optical axis, as illustrated in Figure 13.

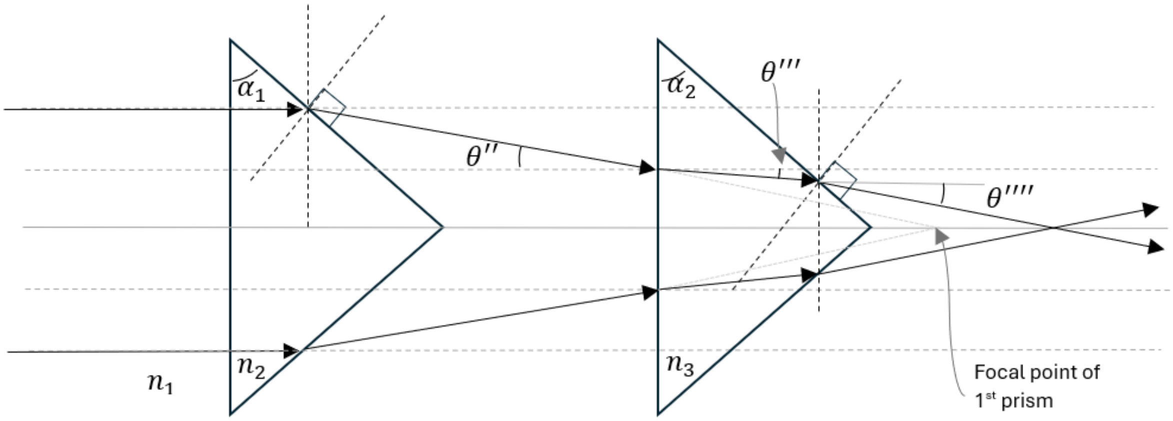

Figure 13. Dual-pyramid configuration

Analysis of the single biprism can be extended to a double prism system, where the incoming light ray into the second prism is incident at θ'' as shown in the Figure 13. Applying the same ray tracing procedure as presented in Figure 9, in correspondence with equations (42) and (44), the following equation for the refracted angle θ''' and θ'''' can be developed as:

$$\theta''' = sin^{-1}\left(\frac{n_1}{n_2} sin(\theta'')\right) \tag{55}$$

$$\theta'''' = \pm\, sin^{-1}\left(\frac{n_3}{n_1} sin(\alpha_1 \pm \theta''')\right) \mp \alpha_2 \tag{56}$$

Here the ± defines whether the second pyramid is located before or after the focal point of the first on the optical axis. If the biprism is placed before then the operations are sequenced as + followed by + then followed by -, and the reverse order (-, -, +) if the biprism is placed after the focal point starting with a negative sign (–). As an example, if the biprism is placed before the focal point, the equation (56) will yield:

$$\theta'''' = sin^{-1}\left(\frac{n_3}{n_1} sin(\alpha_2 + \theta''')\right) - \alpha_2 \tag{57}$$

These formulas can be expressed in terms of α_1 and α_2 only, by substituting equation (48) into the θ'' term in (55)

$$\theta''' = sin^{-1}\left(\frac{n_1}{n_2} sin(\sin^{-1}(n_2\, sin(\alpha_1)) - \alpha_1)\right) \tag{58}$$

Similarly, by substituting (58) into (57) yields:

$$\theta'''' = \pm\, sin^{-1}\left(\frac{n_3}{n_1} sin\left(\alpha_2 \pm sin^{-1}\left(\frac{n_1}{n_2} sin(\sin^{-1}(n_2\, sin(\alpha_1)) - \alpha_1)\right)\right)\right) \mp \alpha_2 \tag{59}$$

Substituting (59) into the corresponding pitch equation (53) yields the pitch equation for the dual-pyramid system as:

$$\begin{aligned} \Lambda &= \frac{\lambda}{2\sin(\theta'''')} \\ &= \frac{\lambda}{2\sin\left(\left|\pm\, sin^{-1}\left(\frac{n_3}{n_1} sin\left(\alpha_2 \pm sin^{-1}\left(\frac{n_1}{n_2} sin(\sin^{-1}(n_2\, sin(\alpha_1)) - \alpha_1)\right)\right)\right) \mp \alpha_2\right|\right)} \end{aligned} \tag{60}$$

The absolute value ensures the refracted angle remains positive. A theoretical comparison of the refracted angle for the specific case of dual-pyramid system to a single pyramid system is presented in Figure 14 below,

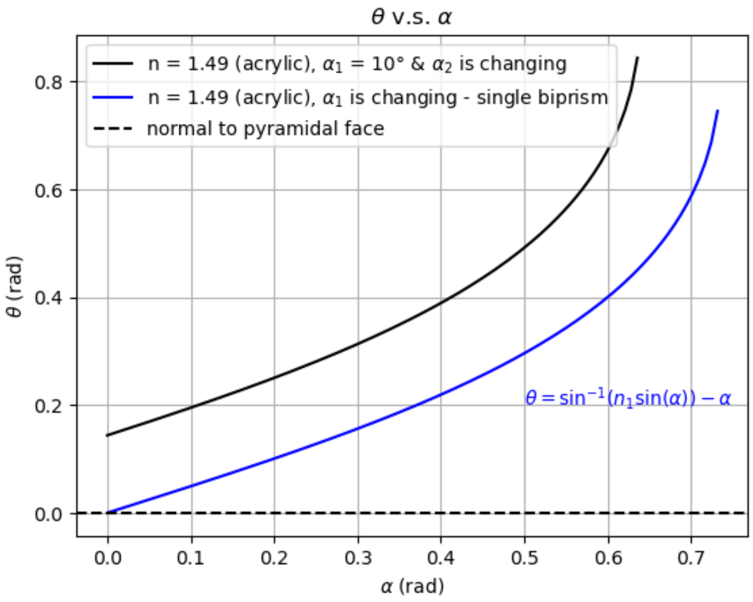

Figure 14. Comparison of change in refraction angle θ over prism angle α for a single biprism system (in blue) vs a dual prism setup where the second prism is placed before the focal point (+, +, -) shown in black.

The results for the black curve are computed considering the set-up was done with the second pyramid positioned before the focal point. The value used for index of refraction for acrylic in the computation was 1.49 [94], and it was assumed that $n_3 = n_2$. It can be seen from Figure 14 that the dual pyramidal system yields a greater refracted angle. Knowing the inverse relationship between refracted angle and pitch value presented in equation (60), in theory it could result in lower spatial periods for the interference region. The results for the computed pitch values are shown in Figure 15 and Figure 16 below,

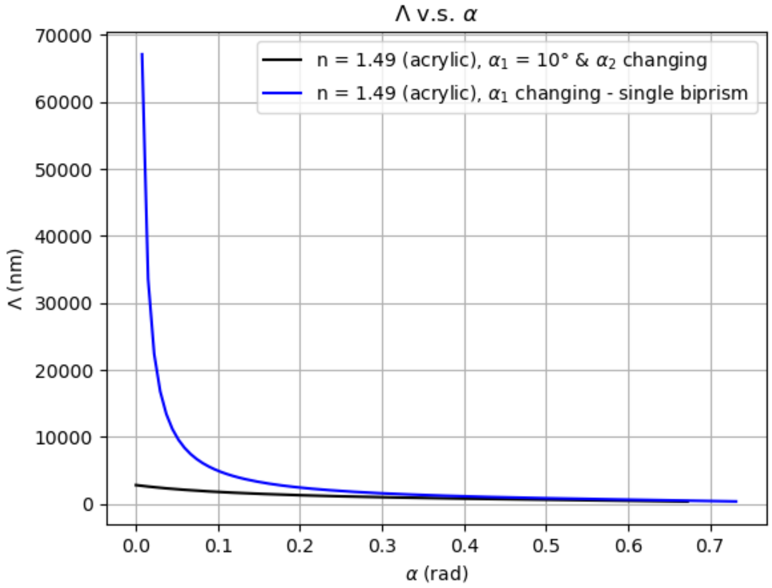

Figure 15. Comparison of pitch value Λ over prism angle α for a single biprism system (in blue) vs a (+, +, -) dual prism setup (in black).

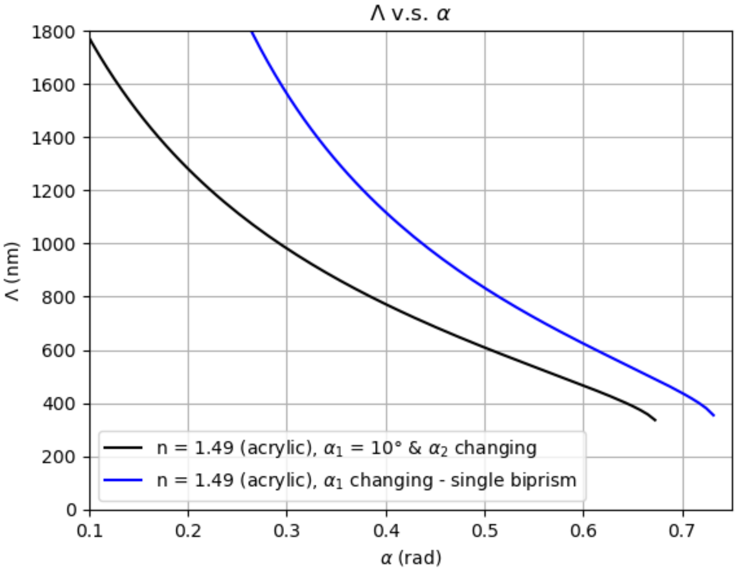

Figure 16. Zoomed in comparison of the change in pitch value Λ over prism angle α from Figure 15. Showing different in pitch values for the visible region.

It can be seen from Figure 15 that the reduction in pitch value is extremely prominent for spatial periods in the far infrared. However, in Figure 16 this reduction is far less but still present for regions in the even in the near infrared (NIR), visible and ultraviolet (UV). It should be notes that the these are simulated results and do not account for certain physical parameters such as UV absorption.

2.3.3 Ray tracing for PIL using lens-pyramid configuration

In the previous section, mathematically demonstration showed that a dual-pyramid system could enables the generation of smaller pitch (Λ) values without requiring the fabrication of a new prism. However, this approach is only feasible if an appropriate combination of two prisms is available. Covering a broad range of pitch values would necessitate multiple prism combinations, requiring many pyramids. Despite this, the resulting grating patterns would remain confined to a narrow wavelength range within the electromagnetic spectrum.

To address this limitation, an alternative approach is explored that allows for tunable pitch values without the need for additional pyramid fabrication. This method involves a lens-pyramid configuration, which is analyzed in this section.

To this mathematical model, a biconvex lens is examined without small angle approximation. This optical component has two outwardly curved spherical surfaces that share the same radius of curvature, R. This geometry enables the lens to converge parallel incoming light rays to a single focal point beyond the lens [95].

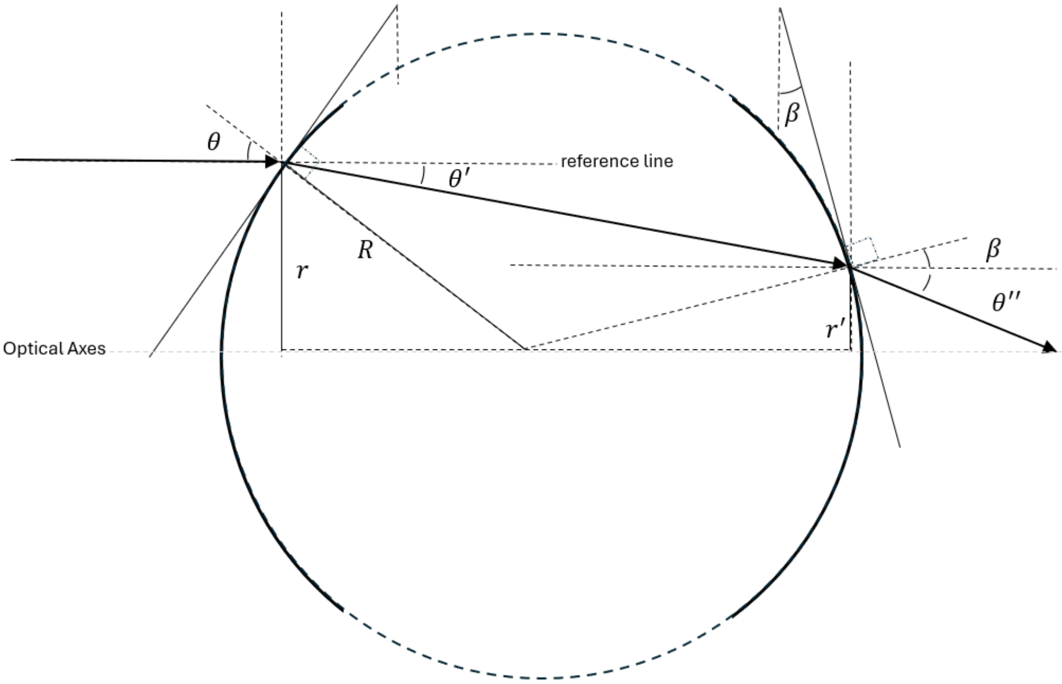

Figure 17. Ray Tracing for Convex Interfaces Without Paraxial Approximation.

Based on the geometry presented in Figure 17, an incoming ray entering the lens with an incident angle θ with respects to the tangent plane on the curved surface, and can be evaluated as the following,

$$\theta = \frac{\pi}{2} - sin^{-1}\left(\frac{r}{R^2 - r^2}\right) \tag{70}$$

The refraction angle θ' as the ray enters the lens can be determined as shown,

$$\theta' = \theta - \sin^{-1}(n_2\, sin(\theta)) \tag{71}$$

Substituting equation (70) into (71) gives an expression of θ' in terms of r as shown:

$$\theta' = \frac{\pi}{2} - sin^{-1}\left(\frac{r}{R^2 - r^2}\right) - \sin^{-1}\left(n_2\, sin\left(\frac{\pi}{2} - sin^{-1}\left(\frac{r}{R^2 - r^2}\right)\right)\right) \tag{72}$$

Where r is the radial distance from the optical axis to the entrance point of the ray. Furthermore, β can be calculated as the following,

$$\beta = \frac{\pi}{2} - sin^{-1}\left(\frac{r'}{R^2 - r'^2}\right) \tag{73}$$

The geometry of the exit point shows, θ'' can be obtained with as the following,

$$\theta'' = sin^{-1}\left(\frac{n_2}{n_1} sin(\theta' + \beta)\right) - \beta \tag{74}$$

Substituting (70) and (72) into (74) leads to the following equation,

$$\begin{aligned}\theta'' = sin^{-1}\Bigg(\frac{n_2}{n_1} sin\Bigg(\pi - sin^{-1}\left(\frac{r}{R^2 - r^2}\right) - \sin^{-1}\left(n_2\, sin\left(\frac{\pi}{2} - sin^{-1}\left(\frac{r}{R^2 - r^2}\right)\right)\right) \\ - sin^{-1}\left(\frac{r'}{R^2 - r'^2}\right)\Bigg)\Bigg) - \frac{\pi}{2} - sin^{-1}\left(\frac{r'}{R^2 - r'^2}\right)\end{aligned} \tag{75}$$

From (75) the diffraction angle θ'' changes with respect to the radial distance from optical axis r and r', where the ray enters at r and exits at r'. This means that based on where the sample plane is positioned, it will have the projection angles change moving away from or along the optical axis.

In a case where the incoming ray is either not collimated or parallel to the optical axis then the expression for θ in (70) no longer applies. In the specific case, where the incoming ray is above the reference line shown in Figure 17, then θ' will be determined in accordance with the following equation:

$$\theta' = sin^{-1}\left(\frac{n_1}{n_2} sin(A)\right) - \theta_1 + A \tag{76}$$

Where A is an offset angle from the reference line. Furthermore, in the case where the lens is positioned after the pyramid and in line on the optical axis – considering the lens is located before the focal point of the pyramid – then A will equate to (48) yielding:

$$A = \sin^{-1}(n_2\, sin(\alpha)) - \alpha \tag{77}$$

Substituting (77) into (76) would give:

$$\theta' = sin^{-1}\left(\frac{n_1}{n_2} sin(\sin^{-1}(n_2\, sin(\alpha)) - \alpha)\right) - \theta_1 + \sin^{-1}(n_2\, sin(\alpha)) - \alpha \tag{78}$$

This would in term changes equation (75) on substitution of (78) into (74). For cases where lens is positioned before the pyramid, the following figure shows the momentum vector analysis on a sample plane position inside the interference region created by the lens-pyramid configuration as shown in Figure 18,

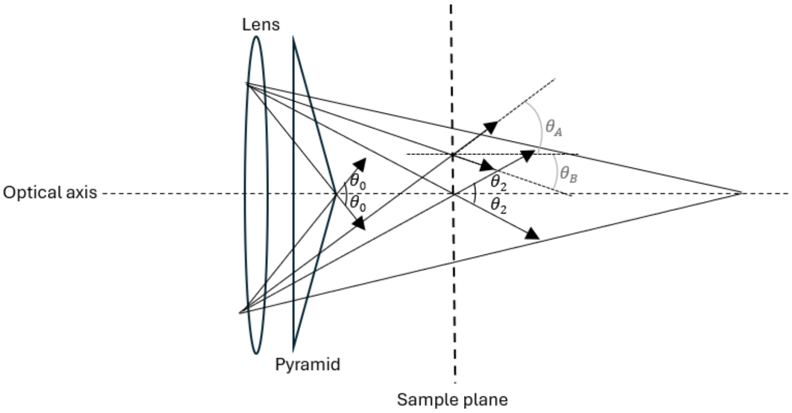

Figure 18. Momentum vector analysis on the sample plane. Where the arrows depict the momentum vectors.

From the above Figure 18, analyzing the projected vectors at an arbitrary point corresponding to momentum associated with θ_A and θ_B the following expression can be formulated:

$$k(sin\,\theta_A + sin\,\theta_B) = K \tag{79}$$

This leads to the following spacing equation with different angles,

$$\frac{2\pi}{\lambda}(sin\,\theta_A + sin\,\theta_B) = \frac{2\pi}{\Lambda} \tag{80}$$

$$\Lambda(sin\,\theta_A + sin\,\theta_B) = \lambda \tag{81}$$

Close to the tip of the pyramid along the optical axis, the pitch values can be approximated as a single pyramid system as expressed in (54). This is because the rays close to the optical axis are well collimated, hitting the entrance of the pyramid at near normal incidence to the pyramid base and thus the pitch can be expressed as the following [69]:

$$\Lambda_0 \approx \frac{\lambda}{2\sin(\sin^{-1}(n_2\, sin(\alpha)) - \alpha)} \tag{82}$$

Where Λ_0 is the pitch on a sample plane close to the pyramid's tip. This allows to solve for the wavelength of the laser beam λ which is considered a constant value, substituting (81) into (82) yields:

$$\Lambda = \frac{\lambda}{(\sin\theta_A + \sin\theta_B)} = \frac{2\sin(\theta_0)}{(\sin\theta_A + \sin\theta_B)}\Lambda_0 \tag{83}$$

Here, the θ_0 and Λ_0 is the refracted angle and the pitch of a pyramid system without any lens, while Λ is the pitch generated by lens-pyramid system. In essence, equation (83) demonstrates the scaling of Λ_0 by a factor of $\frac{2\sin(\theta_0)}{(\sin\theta_A+\sin\theta_B)}$ due to the lens-pyramid system.

An illustration of the ray tracing in the interference region of a lens-pyramid system is shown in Figure 19.

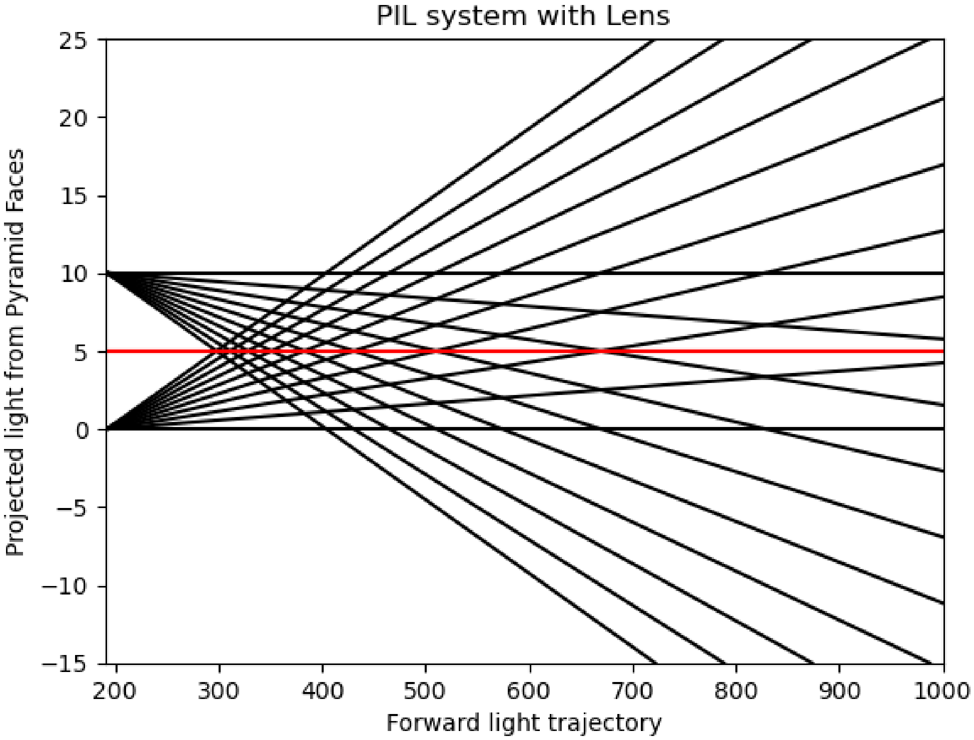

Figure 19. Raytracing simulation for an interference region generated by a lens-pyramid system where the lens is positioned before the pyramid. The virtual point sources are located equidistant from each other at 0 and 10 on the y-axis. The red line depicts the optical axis. The black lines represent the trajectories of rays emanating from the virtual point sources.

It is important to note that in either case of the lens being positioned before or after the pyramid, both θ_A and θ_B change with respect to r' and r in accordance with equation (75). However, considering pitch value residing on the optical axis then the following condition applies:

$$\theta_A = \theta_B \tag{84}$$

As such equation (81) simplifies to the following:

$$\Lambda = \frac{\lambda}{2\sin\left(\theta(x)\right)} \tag{85}$$

Here $\theta(x)$ describes the angle as a function of x , where x is the distance between the tip of the pyramid and the sample plane. According to the ray tracing analysis presented, it is hypothesised that $\theta(x)$ should be inversely proportional to x in accordance with the following:

$$\theta(x) \propto \frac{1}{x^n} \tag{86}$$

Where n could be any real number. Substituting equation (86) into (85) gives the following hypothesised pitch equation:

$$\Lambda_H = \frac{\lambda}{2\sin\left(\frac{1}{x^n}\right)} \tag{87}$$

Chapter 3: Experimental Procedure

The fabrication process for metasurfaces involves a multi-step procedure that encompasses thin film coating, laser pattern inscription, and metal deposition. As outlined in section 1.7, this chapter details the experimental procedures used to develop and analyze metasurfaces. The materials and methods used in the fabrication of plasmonic metasurfaces will be presented. In particular, this chapter covers the preparation of the azobenzene solution, cleaning of the glass substrate, and the formation of thin films via spin coating. The chapter also describes the laser inscription process using the PIL technique to form metasurfaces, the fabrication of pyramids, the methods employed to measure the depth and pitch of the metasurfaces, the deposition of gold onto the surface, and the spectral analysis techniques used to study their optical properties.

3.3 Manufacturing of Pyramids

The pyramids utilized for performing PIL were fabricated at the Royal Military College of Canada by Mr. Snell (Department of Physics and Space Science, RMC, Ontario, Canada)[30]. Depending on the number of faces the pyramid has, during the laser inscription process, the resulting interference patterns produced have up to 8-fold rotational symmetry, as shown by previous work done in the lab [30]. Pyramids with 2, 3, 4, 6, and 8 faces were constructed in the lab from clear acrylic rods (n = 1,495). They were shaped using a milling machine equipped with a dividing head and then polished in the same setup using a rotary lap. Furthermore, to achieve smooth surfaces, a 3-μm diamond paste was applied for polishing [30]. The angles between the faces and the base of each pyramid were 10 degrees ($\alpha = 10^{o}$) and 30 degrees ($\alpha = 30^{o}$). An example of a 3-face acrylic pyramid with $\alpha = 30^{o}$ is shown in Figure 20.

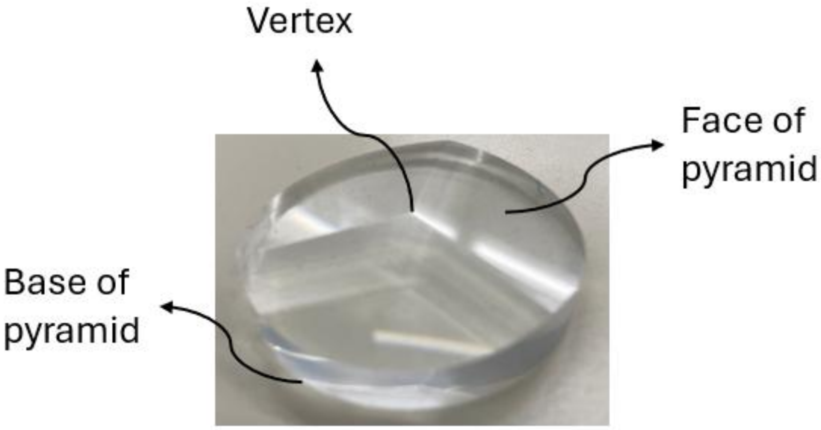

Figure 20. A 3-face pyramid made in-house for the PIL technique.

3.1 Azobenzene Thin Film

The accuracy of nanofabrication in interference-based lithography largely relies on the quality of the thin films, which act as the essential layer where patterns are formed. The initial step involved in forming uniform thin films on clean glass substrates is preparing the azobenzene solution. The azobenzene molecular glass was synthesised through the established literature procedures [96].

Forming thin films on glass substrates required careful cleaning to ensure consistent film quality. The substrates used were 38 × 38 mm glass microscope slides (Corning 0215, Ted Pella, Redding, CA, USA). To ensure uniform thin-film deposition, the glass slides must be free of dust, oils, and other contaminants. These slides were first washed with dish soap and water to remove surface oils and debris. After rinsing, they were dried using clean, compressed air to eliminate any remaining moisture or dust particles. The glass slide was submerged in acetone (C_3H_6O) to dissolve water and remove it from the substrate. The resulting substrate was then dried using a stream of sterile, moisture-free air to remove any remaining microscopic debris.

Thin films of azobenzene molecular glass (gDR1) were prepared by spin coating 3 wt% solution of gDR1 in dichloromethane on the glass substrate, which is based on established literature procedures [97, 98]. To achieve a uniform film covering the entire substrate, parameters for the specific RPM and amount of solution to be used were carefully selected.

To have a thin film on the glass slide, a 70 µL aliquot of the prepared azobenzene solution was used for each sample by gently depositing it on top of the glass substrate placed on the spin-coater (Headway Research Inc., Texas, USA) head, which was set at 1300 RPM, resulting in a thin film approximately 400 nm thick. The coated slides were then dried in an oven at 70 °C for 15 min to ensure complete solvent evaporation.

3.2 Laser Inscription

The movement of azobenzene molecules across a thin film induced by light is used to pattern metasurfaces [99]. For this inscription process, a 488 nm Argon gas laser (Lexel model 95L-UV, Cambridge Lasers Laboratories, Fremont California) is used in conjunction with the PIL technique.

The laser first passed through a quarter-wave plate, converting the light from linear to circularly polarized. This is done to ensure all azobenzene molecules, of any given orientation, within the thin film will interact equally with the laser beam over time [100]. After passing through the waveplate, the laser beam goes through a spatial filter to remove noise and imperfections in the beam intensity profile. The laser is then collimated using a lens, as per established literature procedures [30, 49, 50]. Here, the collimating lens expanded the beam to approximately 11 cm in diameter. The beam diameter is then controlled using a variable iris positioned right in front of the lens.

Next, the beam goes through an acrylic pyramid with a base angle of $\alpha = 30$. The pyramids used in the experiment had varying base diameters and areas. However, the beam diameter was consistently kept smaller than the pyramid's base to maintain a uniform interference pattern. It is also important to note that the vertex of the pyramid was aligned with the center and pointed in the direction of the collimated beam. As mentioned in section 1.5, the pyramid splits the beams at specific angles, allowing them to overlap, forming an interference region [69]. This interference region is used to pattern the photo-responsive thin film on the sample.

The sample with azobenzene thin film is placed inside the laser interference region and oriented such that the plane of the sample is parallel to the base of the pyramid. The exposure time of the laser beam on the sample varied between 60 seconds to 190 seconds depending on the metasurfaces being fabricated. The irradiance of the incident collimated laser beam on the pyramid was maintained at two different values: 167 mW/cm^2 or 85 mW/cm^2. These irradiance values, along with the exposure times, were determined through trial and error, as a specific combination of the two yielded the optimal depth for SPR. The schematic for the setup discussed is provided in Figure 21.

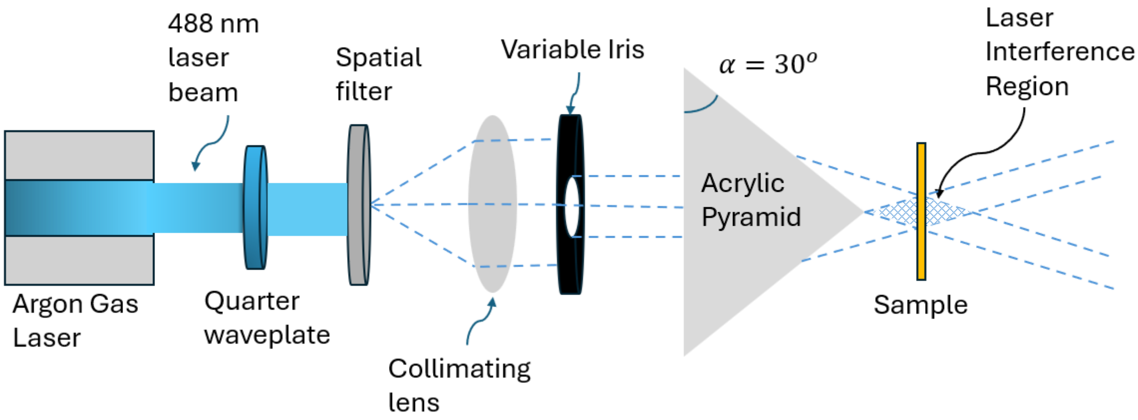

Figure 21. Schematic of laser exposure and interference pattern formation on gDR1 using a single pyramid system

The setup shown in Figure 21 enables the patterning of metasurfaces with periodicity in the visible range, as specified by equation (54), provided in section 2.3.1. For patterning greater periodicity in the IR region, the dual-pyramid system was used. In this set-up, another acrylic pyramid with $\alpha = 10^o$ is added in the path of the beam. With this setup, the position of both pyramids matter, as it could result in increasing or decreasing the periodicity in the final pattern. To achieve pitch sizes in the infrared (IR) region, the setup employs a dual-pyramid configuration—modeled using Equation (59) , as described in Section 2.3.7, and following the sign convention (−, −, +)—in which the second pyramid is positioned beyond the focal point of the first. The schematic of the modified dual-pyramid setup is provided in Figure 22.

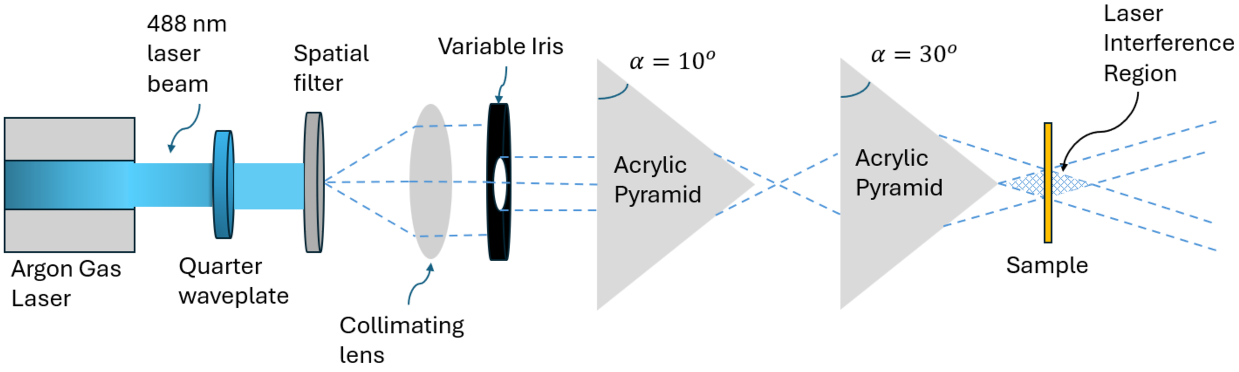

Figure 22. Laser Exposure and Interference Pattern Formation on gDR1 using a dual-pyramid system

It can be seen from Figure 22 that the second pyramid with base angle $\alpha = 30^o$ is positioned after the focal point of the pyramid with the base angle of $\alpha = 10^o$ indicated by the intersecting blue lines between the two pyramids. Figure 23 shows an actual image of this setup in the laboratory.

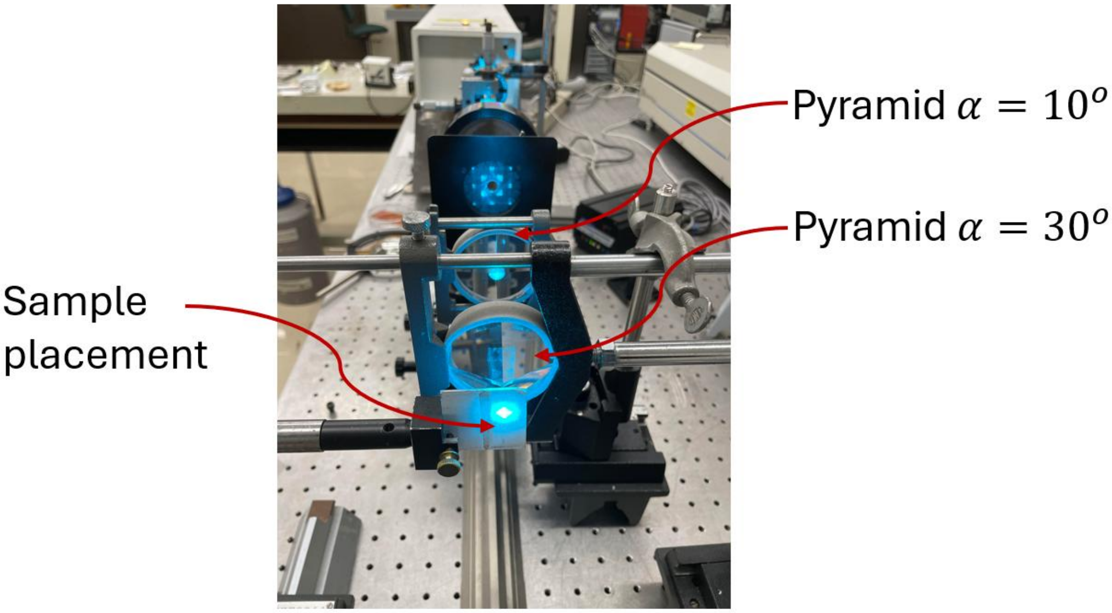

Figure 23. Shows the experimental setup for a dual-pyramid system for a 4-face PIL to produce metasurfaces with 4-fold symmetry and periodicity in IR

Regarding Figure 23, the location of the sample placement is marked by a white screen, which is used to display the interference region, as indicated by the projected blue dot.

3.3 Depth and periodicity measurements

Following the laser inscription process, the fabricated metasurfaces were analyzed for their depth and periodicity (pitch) values. They are critical design parameters that will directly affect the optical response of a metasurface. Measuring them ensures the fabricated structure matches the intended design, especially when using the PIL technique, where beam angles and interference patterns define the structure, as established by prior research [30].

3.3.1 Depth measurements

Depth measurements were taken using an atomic force microscope (Dimension Edge AFM, Bruker, San Jose, CA, USA). The microscope used a peak force tapping mode, where the AFM needle tip vibrates just over the sample surface and scans a given area line by line to generate a 3D image of the surface topography, as per established literature procedures [49] [101] . For each metasurface, AFM scans were taken at three different areas around the center of fabrication. The AFM was set to scan an area of $10 \times 10\, um^2$ or $20 \times 20\, um^2$ depending on the metasurfaces being studied. The scan rate was set to 1 Hz per line. The captured AFM images were then corrected using a built-in 2D plane fit function to level the surface. A rotated section was selected to measure the scanned depth. Here, the number of sections taken for data collection depended on the order of symmetry for the patterned metasurfaces. For each section, the maximum and minimum depths were recorded, and the average of these two values was calculated. Furthermore, each section is indicated by a section line. An example of how this was carried out for a metasurface with 3-fold rotational symmetry is shown in Figure 24.

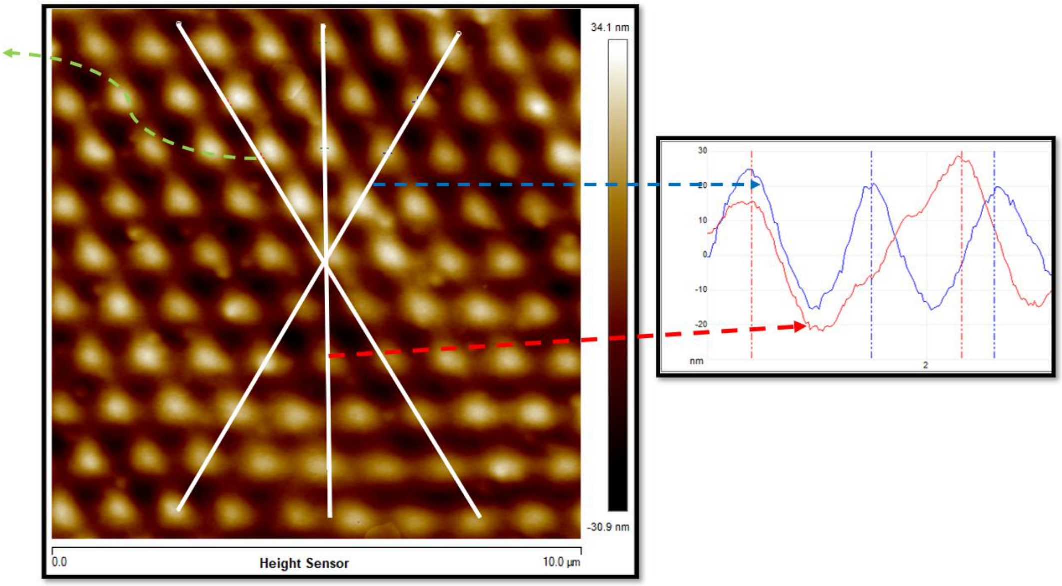
Rotated section line

Figure 24. Example measurement of a metasurface with 3-fold rotational symmetry produced in the lab.

3.3.2 Periodicity (pitch) measurements

The periodicity of the metasurface is a key factor as it influences how the metasurface responds to light. Therefore, accurately measuring the pitch is essential to ensure alignment with the intended design and to validate the fabrication process. As such, after taking depth measurements, the periodicity of the metasurfaces was determined by observing diffraction patterns in transmission, which were projected onto a screen behind the sample. To verify the resulting pitch, a 5 mW He-Ne laser with a wavelength of 632 nm was diffracted through the patterned metasurface. The diffraction angles between the $m \pm 1^{st}$ diffraction orders (m) were measured using the grating equation:

$$\Lambda = \frac{m\lambda}{2\,sin\,\theta} \tag{88}$$

where Λ is the grating pitch, λ is the laser wavelength, and θ is the diffraction angle. By mounting the metasurface on a motorized rotating stage, the angles corresponding to $m = 0, m = -1$ and $m = +1$ diffraction orders were recorded, as established by prior research [30]. The angles were recorded by rotating the stage until the $m = \pm 1$ diffraction orders aligned with the position of the 0^{th} order. The setup to carry out this measurement is presented in Figure 25 below.

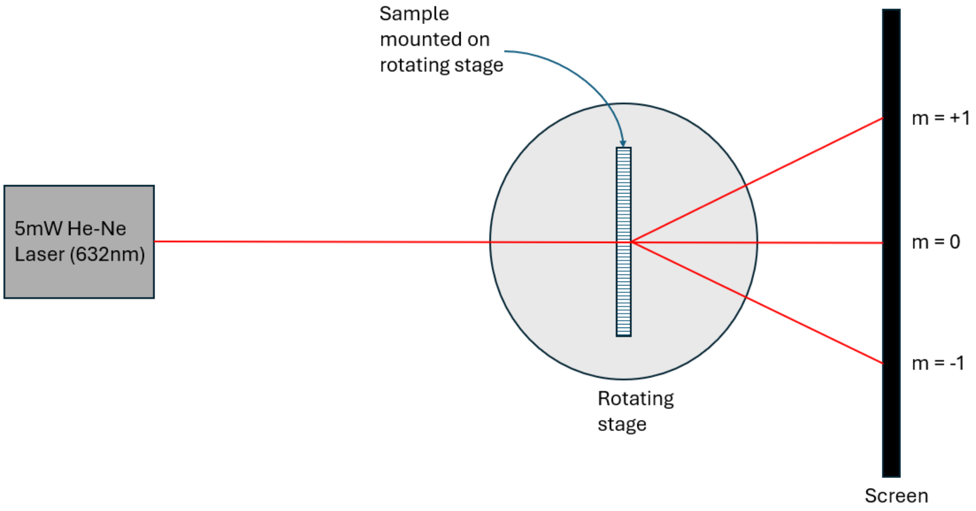

Figure 25. Optical setup used to verify metasurface periodicity

It should be noted that although the stage is equipped with a dial to measure the change in angle, this process was automated using LabView, which directly inputs the corresponding angle values into Equation (88) to calculate the grating pitch Λ.

3.4 Gold (Au) Deposition

As discussed in Chapter 1, SPR excitation requires a metal–dielectric interface [1], making it necessary to metalize the metasurfaces patterned on the azobenzene film. Following verification, the final fabrication step involved depositing a thin metal layer. For this thesis, a thin layer of gold was sputter-coated onto the gDR1 thin film using a plasma coater (Q150V ES Plus, Quorum, Laughton, East Sussex, UK). A gold film thickness of 50 nm was selected for the experiments in this thesis, in accordance with values reported in previous work [97]. Finally, the fabrication process for preparing metasurfaces is summarized in Figure 20 below.

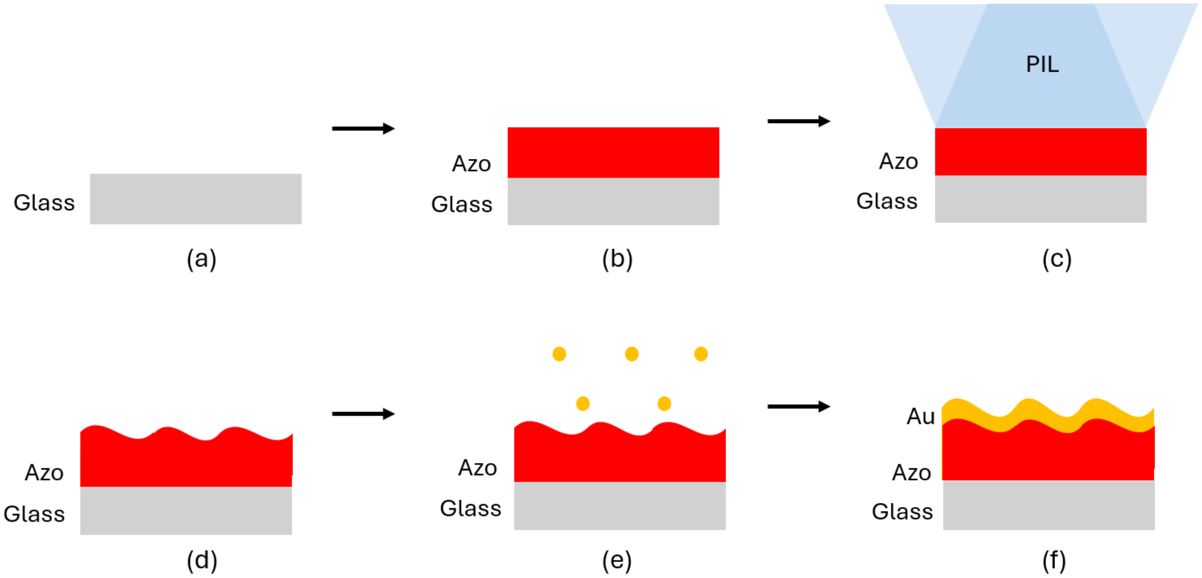

Figure 26. Fabrication process for plasmonic metasurfaces. (a) Preparation of glass slide - substrate cleaning (b) Preparation of Azobenzene solution, Spin-coating and oven drying (c) Inscription using PIL (d) Characterization (e) Au deposition using sputter coater (f) Final sample.

3.5 SPR Spectrometry and Imaging of Metasurfaces

Spectrometry is a crucial component of experimental measurements as it identifies the specific wavelengths at which surface plasmons are excited, providing precise spectral information about the optical response of metasurfaces. Equally important, SPR imaging offers spatial information, revealing how the plasmonic behavior varies across different regions of the metasurface. Performing both measurements simultaneously enables a comprehensive analysis by correlating the spatial distribution of SPR activity with its corresponding excitation wavelength, thereby providing more information about the resonance behavior in relation to the fabricated structure.

SPR responses can be detected from plasmonic metasurfaces as absorption dips when acquired in reflection mode [102]. When light interacts with the plasma, a portion of it is dissipated into heat, and a portion of it is decoupled back as light [1]. When light is reflected off a flat surface, it is phase shifted by π [80]. This means that the spectrometer sensor, due to conservation of energy, should register relatively the same irradiance as the incident beam assuming perfect reflection. However, if light was to couple into the plasma undergoing the SPR phenomenon, then only a portion of that light will be decoupled into free space [1] and, therefore, be registered by the spectrometer at lower irradiance than the incident beam. Thus, in reflection, this will be registered as a dip compared to light being reflected off the sample outside the fabricated metasurface.

In this thesis, all spectrometer readings will be taken under reflection. However, only with SPR imaging under the cross-polarizer setup will a peak be observed rather than a dip. The details of which will be discussed in section 3.5.2.

3.5.1 Optical set-up for SPR spectrometer measurements

For this study, spectral data were collected in reflection using a spectrometer (QE Pro, Ocean Insight, Orlando, FL, USA). A halogen white light source (Oriel Corp., Newport Corporation, California, USA) was collimated using a biconvex lens and then passed through a variable iris, which adjusted the beam to a diameter of less than 0.5 cm. The collimated beam then passed through a linear polarizer. This linearly polarized light was directed onto a glass slide positioned at an angle that allowed equal portions of the light to be transmitted and reflected. The reflected portion was focused using a lens with a 20 cm focal length onto a fiber optic sensor connected to the spectrometer. Meanwhile, the transmitted light traveled toward the sample and was reflected back along the same optical path. This reflected signal passes through the glass slide again and goes through the focusing lens before being collected by the spectrometer for analysis. The sample itself was mounted on a rotating stage to allow for a degree of adjustability in light incidence angles. A schematic for this optical setup is provided below,

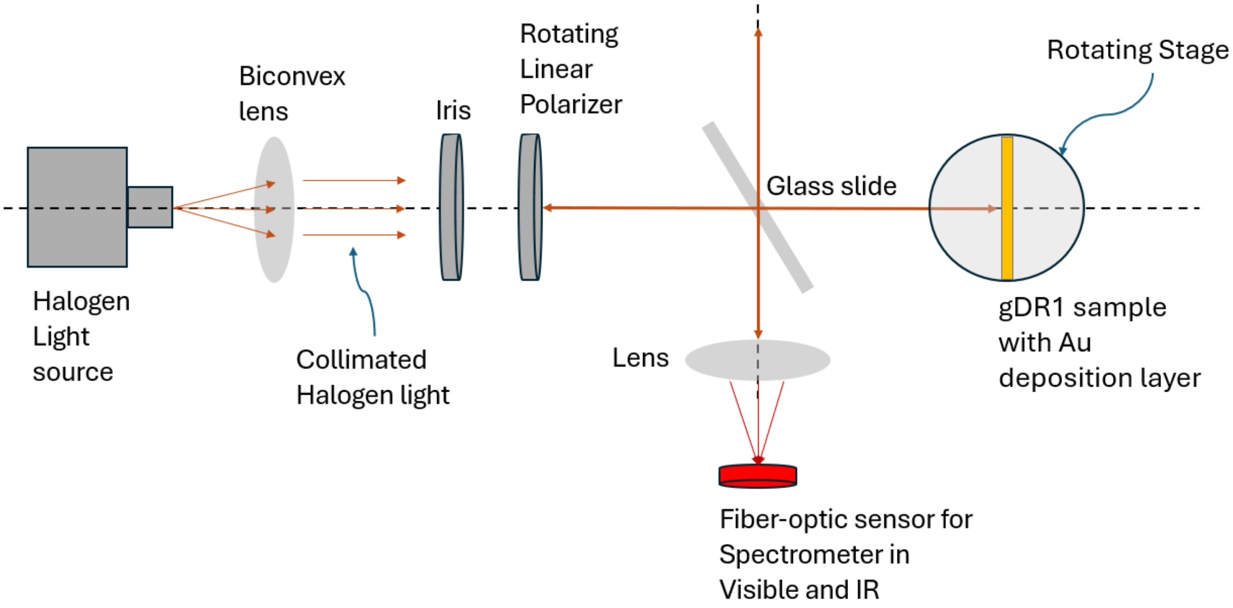

Figure 27. Set-up for spectrometry in reflection. This setup is compatible with both visible and infrared detection. The half-mirror allows the reflected light from the sample to be detected by the spectrometer.

As shown in Figure 27, any out-of-phase light resulting from SPR coupling will be detected by the sensor. Here, light first strikes the air-metal interface of a metasurface; a portion of the light is reflected into the spectrometer, while the rest is transmitted through the grating. As mentioned earlier, this intensity difference can be detected as a dip in the absorption spectrum. To capture this change in intensity, the incident light is first normalized on the flat sample surface (i.e., the non-patterned surface) and then directed into the patterned region. This is because, under non-resonance conditions, most of the light is reflected back into the spectrometer. This is why the spectrometer is normalized or referenced outside the grating before light is directed onto the metasurfaces.

3.5.2 Optical set-up for SPR imaging

SPR imaging was conducted using a CMOS NIR camera (G-130 TEC1 Goldeye, Allied Vision, Stadtroda, Thuringia, Germany). To perform imaging for the metasurfaces, collimated light from a halogen lamp was first directed through a rotating linear polarizer. The polarized beam was then incident on a glass slide positioned to equally split the light—partially reflecting it away from the sample and partially transmitting it toward the sample. The transmitted beam was reflected back along the same optical path after interacting with the sample, which comprised the metasurface. The beam then passed through a second linear polarizer, which was oriented perpendicular to the first (cross-polarized configuration). Any light transmitted through this second polarizer indicated a change in polarization state caused by interaction with the metasurface, thereby highlighting SPR activity. Finally, the beam passes through a second glass slide, where a portion of the light is reflected into the spectrometer, and the remainder is transmitted toward the IR camera for imaging. The schematic for this optical setup is shown in Figure 28.

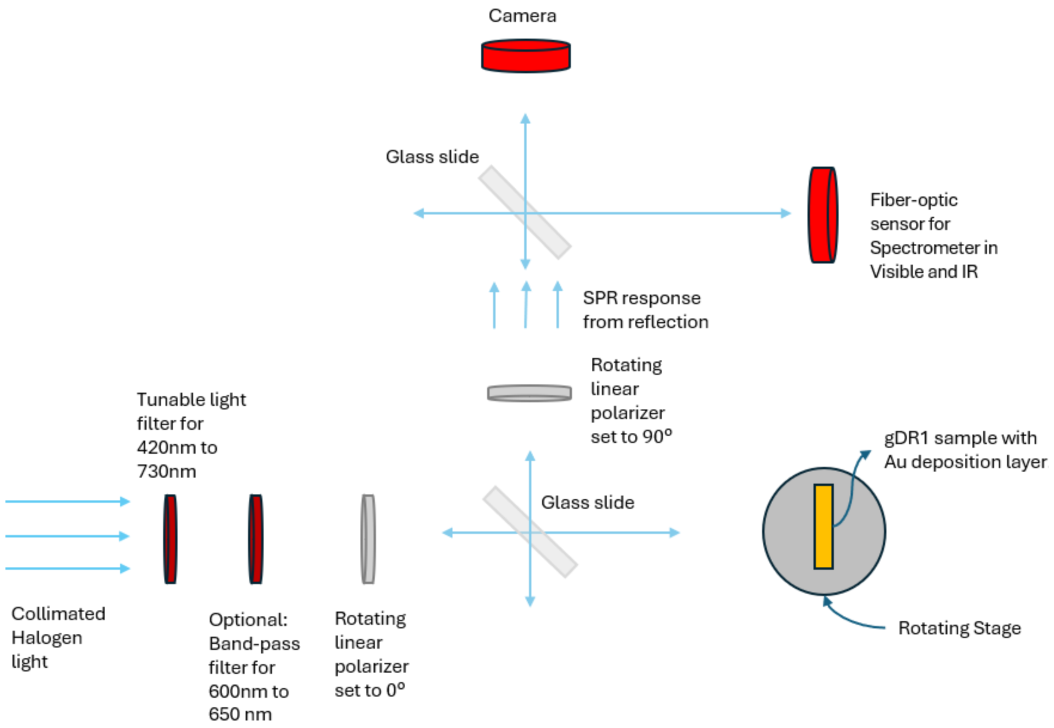

Figure 28. Shows optical set-up for SPR imaging in reflection. This setup works for both visible and infrared imaging, allowing either the visible light filter to be kept or replaced. The cross-polarizer setup allows only for light emitted due to SPR to be registered by the Camera.

Regarding Figure 28, the cross-polarizers are adjusted to a perpendicular polarization axis, allowing the minimum amount of light to pass through, as per Malu's Law, which is registered as dark pixels on the camera. Thus, any enhancement in light is picked up as bright pixels on the camera. Furthermore, an optional band-pass filter and a tunable light filter are also available. The band-pass filter is used to eliminate noise and focus on a specific bandwidth of interest regarding the SPR response. There is also a tunable light filter, which can be used to tune to specific wavelengths in the visible region while filtering out the rest. Additionally, regarding the spectrometer, all measurements were recorded with an integration time of 100 milliseconds. It is also important to note that the gDR1 sample is positioned on a stage, and any experimental results moving forward will be carried out with R_{H} expressing rotations about the horizontal axis and R_{v} expressing rotations about the vertical axis relative to the rotating stage. This is illustrated in Figure 29 below.

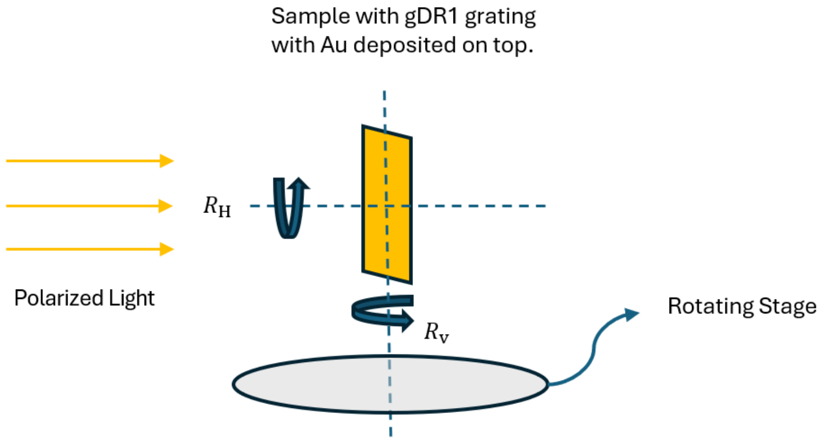

Figure 29. R_H *expresses rotation about the horizontal axis, while* R_v *expresses rotation about the vertical axis.*

Furthermore, an image of the actual sample mounted on the stage is provided in Figure 30.

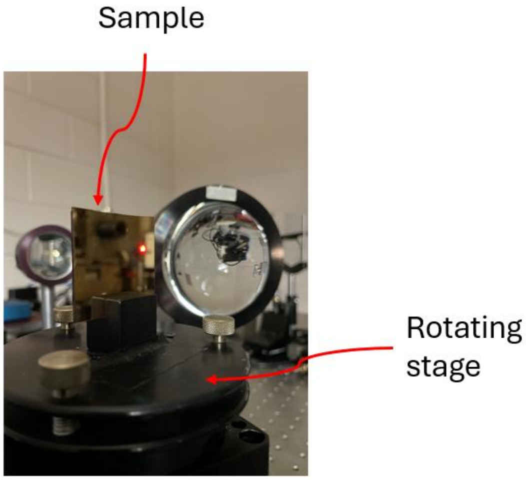

Figure 30. Sample positioning on the rotating stage.

Chapter 4: Experimental results and discussion

This chapter presents and discusses the data collected using the experimental setup and methods described in Chapter 3. In particular, this chapter presents spectrometry results from metasurfaces patterned with various rotational symmetries, including 3-fold, 4-fold, 6-fold, and 8-fold rotational symmetries. The SPR responses, as well as pitch values, are analyzed and compared to expected values for each metasurface. This chapter also presents SPR imaging results from plasmonic metasurfaces patterned using the PIL technique, which exhibit 3-fold and 4-fold symmetry. In addition, the chapters also presents a proof of concept for a dual pyramid system in predicting periodicity, as well as a proof of concept for PIL with a lens-pyramid system and its ability to produce varying pitch sizes.

4.1 Results for PIL using dual pyramid system

The following demonstrates a proof of concept for the dual pyramid system, which was primarily used for developing metasurfaces with periodicities in the infrared (IR) region. To demonstrate its feasibility, the experiment was conducted using two Fresnel biprisms (pyramids composed of two faces) made of Acrylic. The optical setup for the dual pyramid system for PIL is the same as the one presented in Figure 22, provided in Section 3.2. More specifically, a 488nm laser with an irradiance of $167\frac{mW}{cm^2}$ was used with an exposure time of 190 seconds. The system follows the configuration in which the second pyramid is placed beyond the focal point of the first, and it is modeled using equation (56), which incorporates the respective sign convention provided in Section 2.3.2. The values used for the base angles are $\alpha_1 = 10^o$ and $\alpha_2 = 30^o$. To focus more on the path taken by the laser beam, a simplified version of the setup is provided in Figure 31.

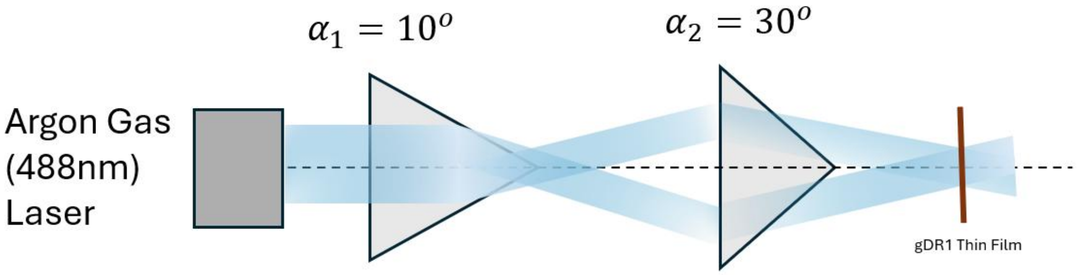

Figure 31. Optical setup for PIL with dual pyramid system. Showing the path taken by the laser beam.

The resulting pitch measurement can be compared to the theoretical pitch measurement calculated according to Equation (60) (provided in Section 2.3.2) and graphed alongside its single pyramid system counterpart; the results are presented in Figure 32.

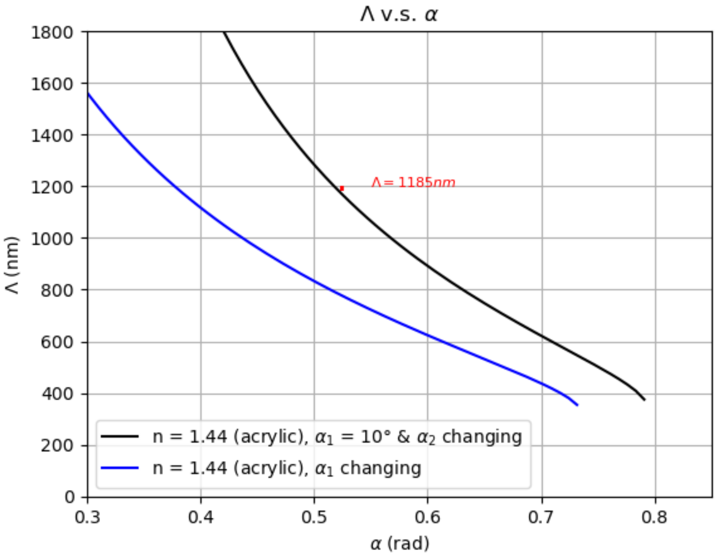

Figure 32. Dual pyramid fabrication results. Having the first prism angle at 10^0 and the second prism angle at 30^0. The red dot represents the experimental pitch value of 1185nm.

Figure 32 shows the results for a grating pitch fabricated using a dual-prism optical setup. As mentioned, the equation (60) was used to calculate the pitch. Under the sign convention presented for a system where the second pyramid is beyond the focal point of the first, the equation to plot the theoretical graph shown by the black line in Figure 32 is presented below,

$$\Lambda = \frac{\lambda}{2\sin\left(-\,sin^{-1}\left(\frac{n_3}{n_1}sin\left(\alpha_1 - sin^{-1}\left(\frac{n_1}{n_2}sin(\sin^{-1}(n_2\,sin(\alpha)) - \alpha_1)\right)\right)\right) + \alpha_2\right)}$$

Substituting values for the base angle $\alpha_1 = 10^o\left(\frac{\pi}{180}\right)$ and $\alpha_2 = 30^o\left(\frac{\pi}{180}\right)$ as well as the wavelength of the laser used as $\lambda = 488\ nm$, the following theoretical pitch value can be evaluated,

$$\Lambda = \frac{488\ nm}{2\sin\left(-\,sin^{-1}\left(\frac{n_3}{n_1}sin\left(10^o\left(\frac{\pi}{180}\right) - sin^{-1}\left(\frac{n_1}{n_2}sin\left(\sin^{-1}\left(n_2\,sin\left(10^o\left(\frac{\pi}{180}\right)\right)\right) - 10^o\left(\frac{\pi}{180}\right)\right)\right)\right)\right) + \alpha_2 = 30^o\left(\frac{\pi}{180}\right)\right)}$$

$$= 1174.52\ nm \approx 1175\ nm$$

The experimentally determined pitch for the dual-pyramid system is 1185nm and is indicated by the red point in Figure 32. As mentioned at the beginning of this section, the prisms being used for this experiment are Fresnel biprisms, which are composed of 2-faces, and its percent error calculation is as follows

$$\%\ error = \frac{|Experimental\ - Theoretical|}{Theoretical} \times 100 = \frac{|\ 1175 - 1185|}{1175} \times 100 = 0.85\ \%$$

A deviation of 0.85% from the experimental results confirms the system's ability to produce gratings with a pitch size of 1174 nm—something unattainable using any single pyramid alone in this experiment. Moreover, the difference between the experimental and theoretical values obtained indicate an uncertainty of approximately ±10 nm, which could present challenges for smaller-scale fabrications. This method of determining periodicity with dual-pyramid systems can be extended to pyramids with a high number of faces for developing patterns of allowed symmetries [30], which comprise those metasurfaces produced using the 3-face, 4-face, 6-face, and 8-face PIL technique. This method will be used extensively to develop pitch sizes in IR for the upcoming sections. While the dual pyramid system allows some flexibility in tuning the pitch, having the capacity to produce a range of different pitch sizes using only two optical elements requires a lens-pyramid system, which will be evaluated in Section 4.13.

4.2 SPR measurements for metasurface with 3-fold symmetry in the visible region

SPR measurements from a plasmonic metasurface with 3-fold rotational symmetry are presented here. Below is an image of the metasurface produced using a 3-face PIL technique, exhibiting pitch sizes in the visible region.

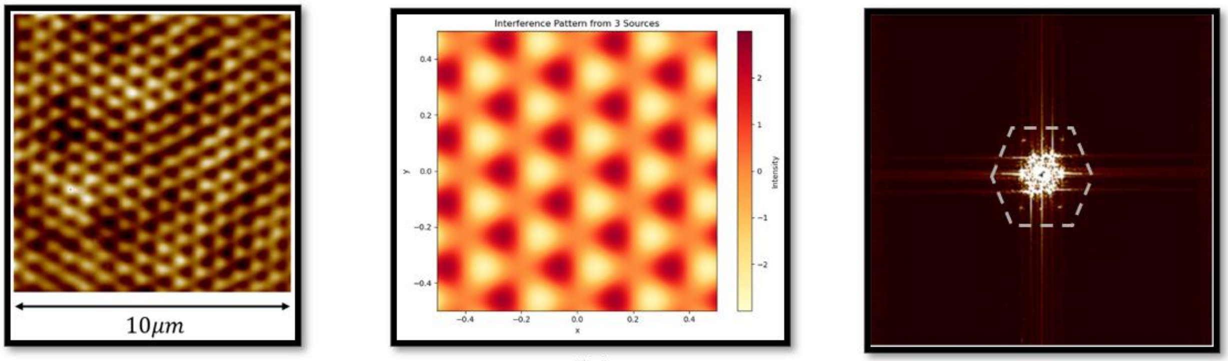

(a) (b) (c)

Figure 33. Image of metasurface with 3-fold rotational symmetry. (a) $10\ \mu m \times 10\ \mu m$ *AFM image of metasurface with 3-fold rotational symmetry with pitch sizes in the visible. (b) Simulated pattern for a 3-face PIL technique. (c) Fast Fourier Transform (FFT) of the corresponding image showing the emergent hexagonal pattern outlined by the dashed lines.*

The metasurface seen in Figure 33 (a) was produced with a 488nm laser with an irradiance of $167\frac{mW}{cm^2}$ and an exposure time of 140 seconds. The metasurface has a pitch Λ value of $682\ nm$ with an average depth of the gratings between 30 nm and 40 nm. The patterns were produced using a single pyramid system with a base angle $\alpha = 30^o$. The simulated image of the 3-face PIL, shown in Figure 33(b), exhibits a high degree of similarity to the actual metasurface, as depicted in Figure 33(a). Furthermore, performing a Fast Fourier Transform (FFT) on the metasurface image in Figure 33 (a) reveals a periodic arrangement of points that is consistent with the expected signature in frequency space of a pattern exhibiting 3-fold rotational symmetry [83]. Additionally, to gain an understanding of the topography of the patterned surface, a 3D AFM image is provided in Figure 34 below.

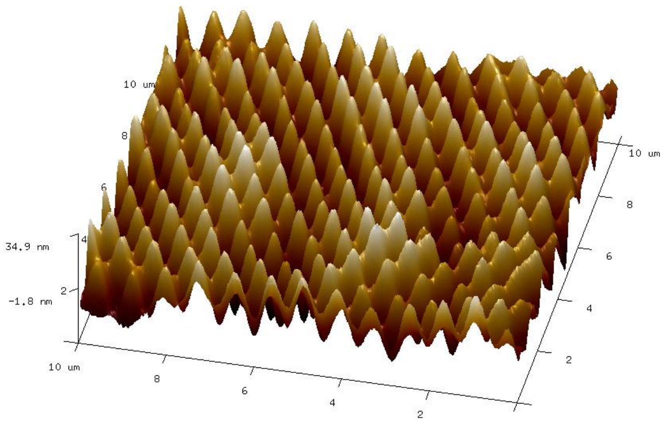

Figure 34. 3D AFM image of triangular structures showing the topography of $10\ \mu m \times 10\ \mu m$ *area of the metasurface presented in Figure 31.*

As shown in Figure 34, the surface is not perfectly flat, exhibiting variations in height across different regions. To obtain SPR spectrometer measurements for a metasurface with 3-fold rotational symmetry in the visible region, the experimental data were collected using the optical setup presented in Section 3.5.1. The data was obtained with the polarizer rotated in increments of 45^o up to 90^o, which is equivalent to rotating the sample about R_{H} in increments of 45^o. This was to observe if there was any shift in the SPR response when the orientation of the metasurface was changed. At $R_{\mathrm{H}} = 0^o$, a distinct response was observed at $\lambda_{SPR} = 702\ nm$. According to the SPR measurements taken, the intensity also appears to decrease, and the peaks seem to split as the polarization axis is changed. The SPR measurements taken for the metasurface with 3-fold symmetry, as shown in Figure 33(a), are presented in Figure 35 below.

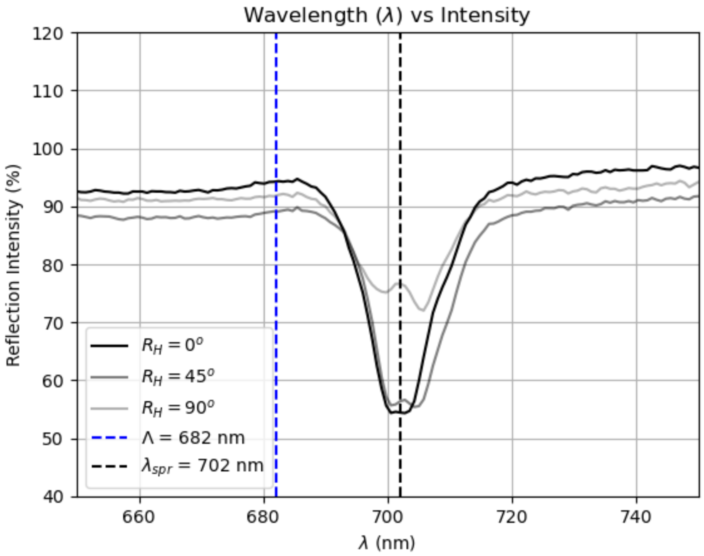

Figure 35. Shows the corresponding SPR reading taken from the spectrometer for the metasurface shown in Figure 33 (a). All readings are done at a normal to the sample surface ($R_v = 0^o$ *). Note that the peak here is shown to be in the middle of the gap where the peaks split, that is, approximately 4nm wide at* $R_H = 0^o$ *.*

The intensity change effect, as shown in Figure 35, can be attributed to the geometry of the metasurface, which has only 3-fold rotational symmetry. Consequently, it is hypothesised that the coupling between the incident electric field and the surface plasmon modes depends strongly on the alignment of the electric field with the periodic structural features of the metasurface. SPR is strongest when the polarization of the incoming light is aligned with the direction of the grating vector; it does not occur when the polarization is oriented perpendicular to it, as established by previous research [103]. As such, according to the rotational symmetry of the pattern, which is only symmetric at 120°, it is theorized that the structure doesn't respond equally to all polarization directions. Furthermore, it is presumed that rotating the polarization reduces this alignment, thereby weakening the SPR response. Past research has shown that the excitation of SPWs strongly depends on the shape, symmetry, and orientation of the nanostructures relative to the polarization of incoming light [104]. Therefore, the observation in Figure 35 can be attributed to the polarization dependence on the symmetry of the metasurface, which also highlights the directional sensitivity of SPW excitation when the surface interacts with linearly polarized light.

Furthermore, the expected values for the intended design of the pitch, as well as the expected values for the SPR response, were compared to the experimentally observed values. Equation (38), the following expected SPR wavelength λ_{SPR} can be calculated:

$$\lambda_{SPR} = \Lambda\left(\sqrt{\frac{(\epsilon_{r,1}\epsilon_{r,2})}{(\epsilon_{r,2}+\epsilon_{r,1})}}\right) = \approx 677\ nm\ (1.064620562)\ \approx 720\ nm$$

$$\%\ error = \frac{|Experimental\ - Expected|}{Expected} \times 100 = \frac{|\ 702 - 720|}{720}\ \times 100\ \approx 2.5\%$$

In terms of the SPR response, a 2.5% error indicates a strong agreement with the expected behavior of the metasurface structure. The expected pitch value used in the above λ_{SPR} the calculation was determined based on the pattern's geometry. Further details on the comparison of observed pitch values to the expected pitch values are provided below.

Experimental pitch observed:

$$\Lambda_O = 682\ nm$$

The process for calculating the expected pitch for Λ_O in accordance with equation (54) is as follows:

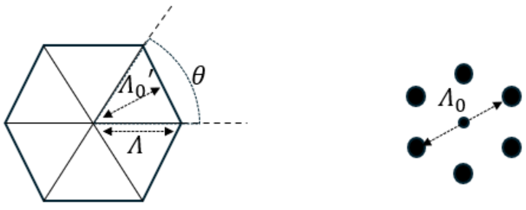

(a) (b)

Figure 36. (a) Shows an illustration of the structured 3-fold symmetric pattern, while (b) shows an illustration of the projected diffraction pattern from the He-Ne laser passing through the metasurface.

Here the pitch Λ_O was measured from point to point, as shown in Figure 36 (b). However, based on equation (54), the expected pitch value $\Lambda_0{}'$ is determined from Λ as follows:

$$\Lambda = \frac{488nm}{2\sin(\sin^{-1}(n_2\, sin(0.52\, rad)) - 0.52\, rad)} \approx 783\, nm$$

$$\theta = \frac{360^0}{6} = 60^0$$

$$\Lambda_0{}' = \Lambda\, cos\left(\frac{\theta}{2}\right) = 783\, nm\left(\frac{\sqrt{3}}{2}\right) = 678\, nm$$

As such, 678nm pitch is the expected value. Thus, observation can be compared to expectation as follows:

$$\%\, error = \frac{|Experimental\ - Expected|}{Expected} \times 100 = \frac{|\ 682\, nm - 678\, nm\ |}{678\, nm} \times 100\ \approx 0.58\, \%$$

This 0.58% variation in periodicity is a plausible contributor to the observed 2.5% discrepancy in the SPR response observed. This percentage deviation can be attributed to the topographical variations observed in Figure 34, which reveals that the surface is not perfectly flat but instead exhibits noticeable undulations across different regions. This highlights a key distinction between the theoretical and experimental SPR: theoretical models typically assume an ideal, flat interface, whereas in reality, as demonstrated by Figure 34, this is not the case.

4.3 SPR measurements for metasurface with 3-fold symmetry in the IR region

Below is an image of the metasurface produced using a 3-face PIL technique with a dual pyramid system, exhibiting pitch sizes in the infrared (IR) region.

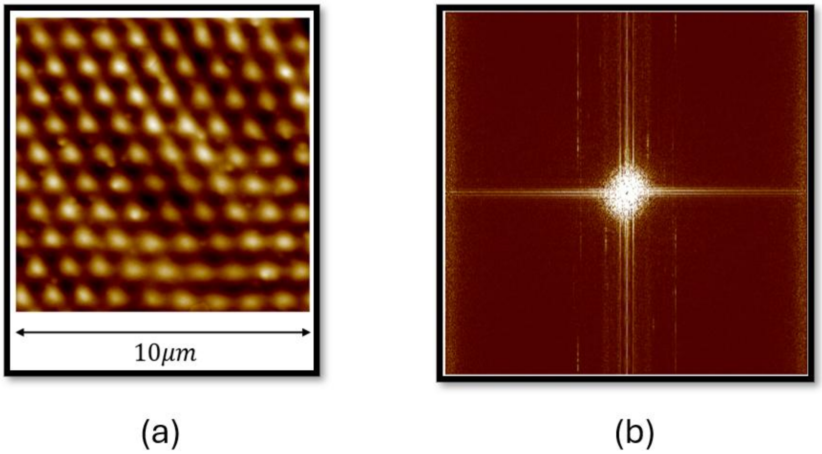

Figure 37. (a) The $10\ \mu m\ \times\ 10\ \mu m$ *AFM image of metasurface with 3-fold rotationally symmetric patterns in IR. (b) The corresponding FFT image.*

The metasurface shown in Figure 37 (a) was produced with a 488nm laser with an irradiance of $167\,\frac{mW}{cm^2}$ and an exposure time of 180 seconds. The metasurface has a pitch (Λ) value of $968\ nm$ with an average depth of the gratings ranging from 26 nm to 35 nm. This metasurface was patterned using the dual pyramid system to achieve the IR grating pitch. The two pyramids used have a base angle of $\alpha_1 = 10^o$ and $\alpha_2 = 30^o$ respectively. Where the pyramid with base angle $\alpha = 30^o$ was positioned after the focal point of the first pyramid. Additionally, the FFT of Figure 37(a) yields minimal structural information, as illustrated in Figure 37(b). This can be attributed to the inverse relationship between spatial domain and frequency domain [93]. For the larger pitch (968 nm), the corresponding frequency components are closely spaced, resulting in overlapping features at a central point in the frequency domain. It is important to note that while scanning a larger area with the AFM could have improved the clarity of the FFT image, it would not have been consistent with the experimental conditions documented in Figure 37(a). Furthermore, inspecting the topography of the metasurface revealed noticeable changes in depth and shape from the intended pattern design.

The AFM was used to evaluate the depth of the patterned structure, as shown in Figure 38,

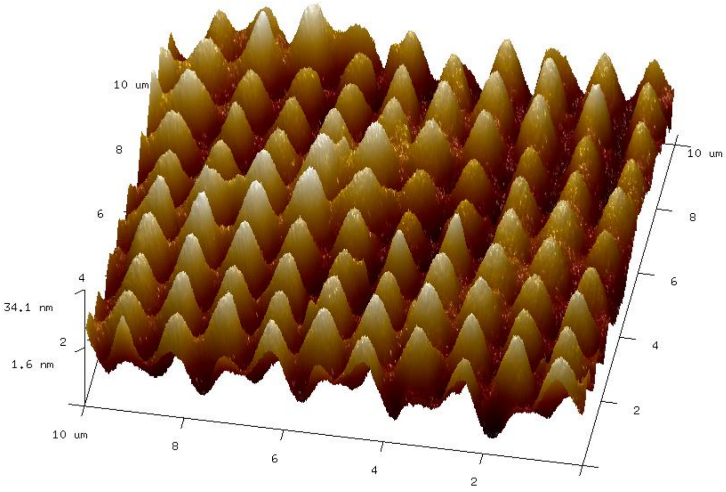

Figure 38. 3D AFM image of metasurface with 3-fold symmetry in IR showing the topography of $10\ \mu m\ \times\ 10\ \mu m$ *area of the metasurface.*

To obtain SPR spectrometer measurements for a metasurface with 3-fold rotational symmetry in the IR region, the experimental data were collected using the optical setup presented in Section 3.5.1. The data was collected with the polarizer fixed at $R_{\mathrm{H}} = 0^o$ because even though rotating it reduced the SPR dip, it was difficult to understand the change in intensity due to background noise fluctuation. Furthermore, two SPR measurements were taken with the spectrometer set to capture responses in the 900 nm to 1000 nm and 900 nm to 1500 nm ranges. The corresponding SPR measurements taken for the metasurface are shown in Figures 39 and 40.

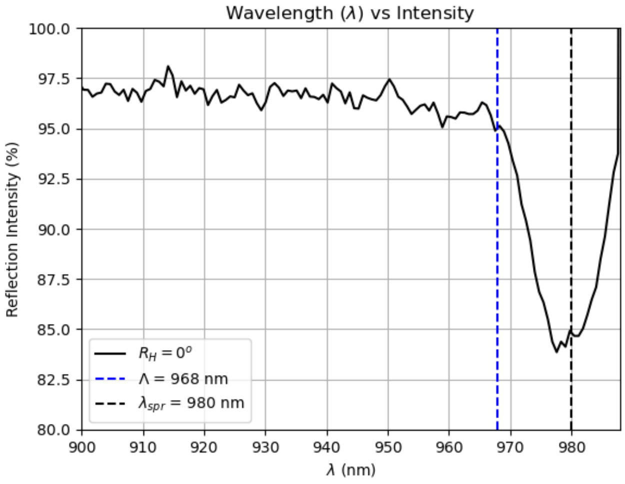

Figure 39. Shows the corresponding SPR reading for the sample shown in Figure 37, taken from the spectrometer set to read in the 900 nm to 1000 nm range. All readings are taken at a normal to the sample surface ($R_v = 0^o$*). Note that the dip appears to be at 980 nm. This was taken with a spectrometer set to read for the visible range.*

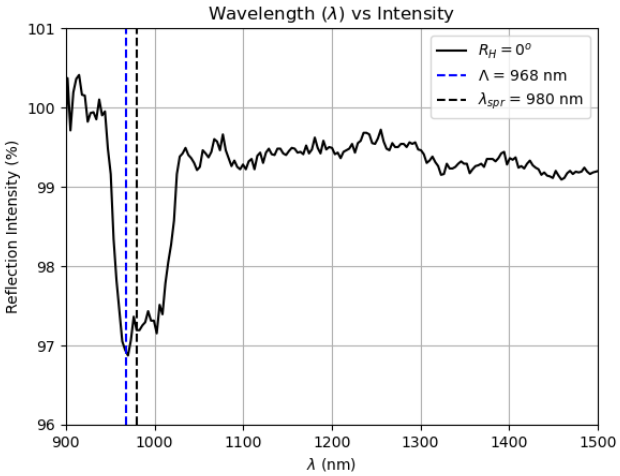

Figure 40. Shows the corresponding SPR reading for Figure 37 and was taken with a spectrometer set to read in NIR (900 nm to 1500 nm range). All readings are done at a normal to the sample surface ($R_v = 0^o$). Note that the dip here is shown to be at 980 nm.

Just as was done in section 4.2, the expected λ_{SPR} can be calculated in accordance with equation (38) and then compared with the experimental observed value as follows:

$$\lambda_{SPR} = \Lambda\left(\sqrt{\frac{(\epsilon_{r,1}\epsilon_{r,2})}{(\epsilon_{r,2}+\epsilon_{r,1})}}\right) = 1017nm(1.064620562) \approx 1083\ nm$$

$$\%\ error = \frac{|Experimental\ - Expected|}{Expected} \times 100 = \frac{|\ 968 - 1083|}{1083} \times 100\ \approx 10\ \%$$

However, unlike section 4.1, the expected pitch Λ'_o calculation is based on equation (60) following a (-, -, +) sign convention:

$$\Lambda = \frac{\lambda}{2\sin(\theta(\alpha_2, \alpha_1))} = \frac{488}{2\sin(\theta(30^o, 10^o))} = 1175\ nm$$

$$\theta = \frac{360^0}{6} = 60^0$$

$$\Lambda'_o = \Lambda\ cos\left(\frac{\theta}{2}\right) = 1175\ nm\left(\frac{\sqrt{3}}{2}\right) = 1017\ nm$$

Experimental pitch observed:

$$\Lambda_O = 968\ nm$$

$$\%\ error = \frac{|Experimental\ - Expected|}{Expected} \times 100 = \frac{|\ 968 - 1017|}{1017} \times 100\ \ \%\ \approx 4.8\ \%$$

As can be seen from the above calculation, the measured pitch deviated by 4.8% from the intended design. However, the observed SPR peak exhibited a 10% error relative to the expected SPR wavelength. Here, the high error in the SPR response can be attributed to the non-uniformity of the metasurface and/or the alignment of polarization axes. The first hypothesis is that the theoretical model assumes perfect periodicity and uniform feature dimensions, whereas in practice, fabrication imperfections are evident, as shown in Figure 38. These could include variations in feature size, shape, or periodicity, which can alter SPR responses according to Equation (38). Past research has reported that fabrication imperfections in the metasurface result in spatial non-uniformity in the resonance spectrum of the plasmonic response across the metasurface [104]. The second hypothesis is the polarization dependence of the structure (as discussed in section 4.1), implying a slight misalignment between the polarization axis and the grating vectors on the metasurface. Perhaps future research can further investigate the reasons for the significant deviation in the SPR wavelength.

Furthermore, the SPR response observed in the IR region appears weaker and less pronounced compared to the visible counterpart in Section 4.2. This might be attributed to a combination of increased material losses in gold at longer wavelengths and potentially reduced coupling efficiency of the metasurface at those wavelengths [113]. Additionally, the spectral power of the halogen light source may decrease in the NIR, further contributing to the lower relative intensity of the measured signal [114].

4.4 SPR measurements for metasurface with 4-fold symmetry in the visible region

SPR measurement from plasmonic metasurfaces with 4-fold rotational symmetry is shown here. Below is the image of the metasurface produced with the 4-face PIL technique with a pitch size residing in the visible region,

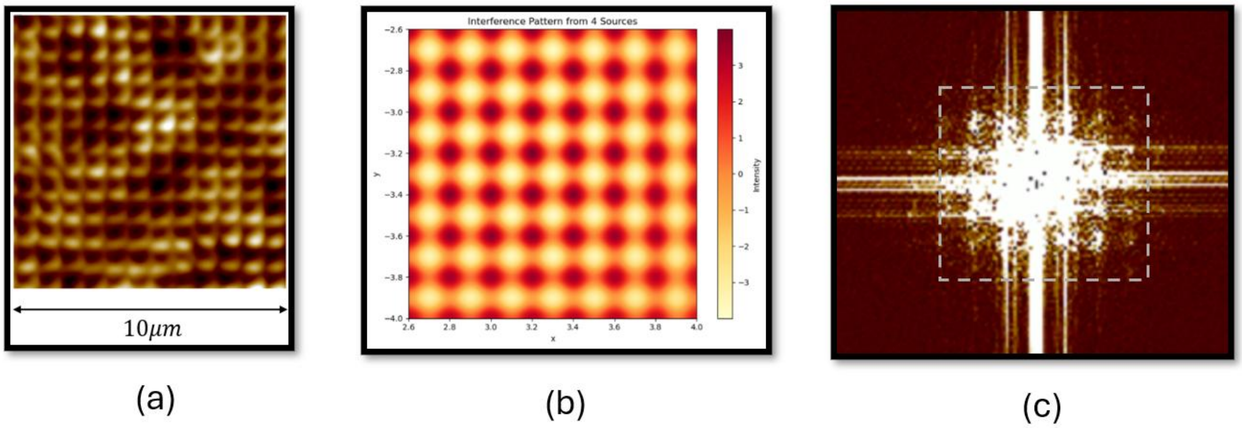

Figure 41. (a) $10\ \mu m \times 10\ \mu m$ *AFM image of metasurface exhibiting 4-fold symmetry in the visible (b) Simulated pattern for a 4-face PIL (c) The corresponding FFT image of the metasurface showing square grid point pattern as outlined by the dashed square.*

The metasurface shown in Figure 41 (a) was produced with a 488nm laser with an irradiance of $85 \frac{mW}{cm^2}$ and an exposure time of 120 seconds. The metasurface has a pitch Λ value of $831\ nm$ with an average depth of the gratings ranging between 30 nm and 45 nm. The patterns were produced using a single pyramid system. Comparing the simulated image of the 4-face PIL shown in Figure 41(b) with the actual metasurface shown in Figure 41(a), the patterns exhibit a high degree of similarity. The square structures don't appear as prominent in the simulation as they do in actual fabrication. Furthermore, the FFT of Figure 41(a) is shown in Figure 41 (c) and displays a grid arrangement of points, which is expected of a pattern in frequency space exhibiting 4-fold rotational symmetry [83].

As was done in previous sections of this chapter, using the optical setup presented in section 3.5.1, measurements of SPR wavelengths were taken using the spectrometer with the polarizer rotated in increments of 45^o up to 90^o, which is equivalent to rotating the sample about R_{H} in increments of 45^o. Interestingly, at $R_{\mathrm{H}} = 0^o$ two distinct responses were observed: $\lambda_{SPR} = 843\ nm$ and $\lambda_{SPR} = 615\ nm$. Furthermore, despite changing the polarization rotation, the change in intensity appears to remain constant. These findings are presented in Figure 42.

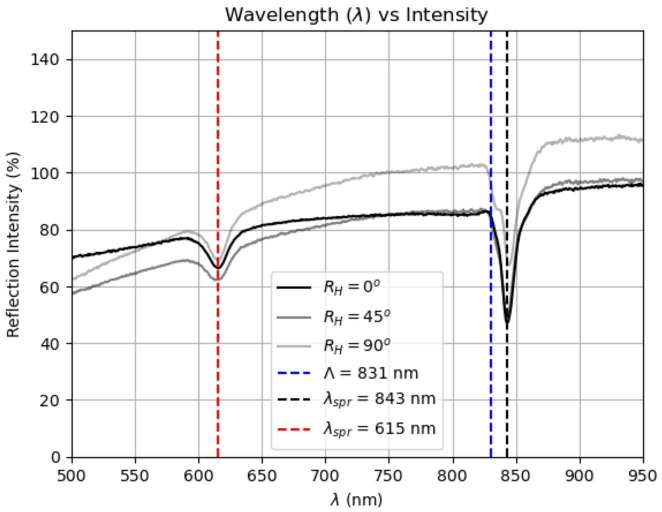

Figure 42. Shows the corresponding SPR reading for Figure 39 (a) and was taken with a spectrometer set to read in NIR. All readings are done at a normal to the sample surface ($R_v = 0^o$).

Just as was done in previous sections of this chapter, the expected λ_{SPR} can be calculated by equation (38) as the following,

$$\lambda_{SPR} = \Lambda\left(\sqrt{\frac{(\epsilon_{r,1}\epsilon_{r,2})}{(\epsilon_{r,2}+\epsilon_{r,1})}}\right) = 783\ nm(1.064620562) \approx 833\ nm$$

$$\%\ error = \frac{|Experimental\ - Expected|}{Expected} \times 100 = \frac{|\ 843 - 833|}{833} \times 100\ \approx 1.2\ \%$$

Here, the expected pitch Λ_o' calculation is based on equation (54) as the following:

$$\Lambda_o' = \frac{488nm}{2\sin(\sin^{-1}(n_2\, sin(0.52\ rad)) - 0.52\ rad)} \approx 783\ nm$$

Experimental pitch observed:

$$\Lambda_O = 831\ nm$$

$$\%\ error = \frac{|Experimental\ - Expected|}{Expected} \times 100 = \frac{|\ 783\ nm - 831\ nm|}{831\ nm} \times 100\ \approx 5.8\ \%$$

However, as shown in Figure 42, a more minor secondary SPR absorption dip is observed at 615 nm. To explain this, the hypothesis is that the secondary response at 615 nm is generated due to the square geometry of the patterned structure. The geometrical assessment of the secondary pitch is presented below.

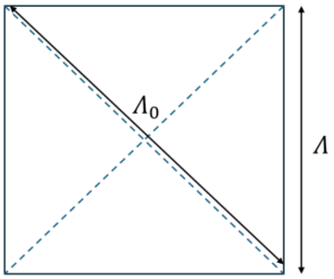

Figure 43. Representation of a single square nanostructure, with the height and width expressed as the pitch Λ

Based on Figure 43, the following expected value of Λ can be evaluated:

$$\Lambda = \ sin(45^{o})\,\Lambda_{o}' = \ 783nm(0.707) \approx 553\ nm$$

λ_{SPR} can be calculated in accordance with equation (38) as the following,

$$\lambda_{SPR} = \ \Lambda\left(\sqrt{\frac{(\epsilon_{\mathrm{r},1}\epsilon_{\mathrm{r},2})}{(\epsilon_{\mathrm{r},2}+\epsilon_{\mathrm{r},1})}}\right) = \ 553\ nm(1.064620562) \approx 588\ nm$$

$$\%\ error = \frac{|Experimental\ \ - Expected|}{Expected} \times 100 = \frac{|\ 615 - 588|}{588} \times 100\ \ \approx 4.6\ \%$$

Based on this calculation, the measured secondary SPR response deviates by 4.6%, providing a compelling explanation for the secondary response observed. However, there was a 5.8% error in primary pitch deviation, despite an SPR wavelength having a1.2% deviation. The deviation for the primary pitch could be due to instrumentation uncertainty, as the helium-neon laser used to measure pitch can be offset by 10 nm. Accounting for an additional 10nm for the percent error calculation would put the deviation below 5%. Furthermore, from Figure 42, no shift in the SPR wavelength was observed with regards to a 45^{o} increment shift in the polarization angle. It is hypothesized that rotating by intermediate angles, such as 45^{o} may not result in a noticeable change due to the higher-order 4-fold symmetry. Past research has explored the polarization properties of optical metasurfaces with different ordered symmetries [105], which could explain the lack of change in the SPR response and/or provide an avenue for future research to explore the link between higher symmetry orders and lack of change in SPR responses. Although speculative, this may be attributed to the presence of a higher number of grating vectors, which may enable improved alignment with the polarization axes and thereby minimize any noticeable difference in the SPR wavelength.

4.5 SPR measurements for metasurface with 4-fold symmetry in the IR region

Below is the image of the metasurface produced with the 4-face PIL technique using a dual-pyramid setup with a pitch size residing in the infrared (IR)region,

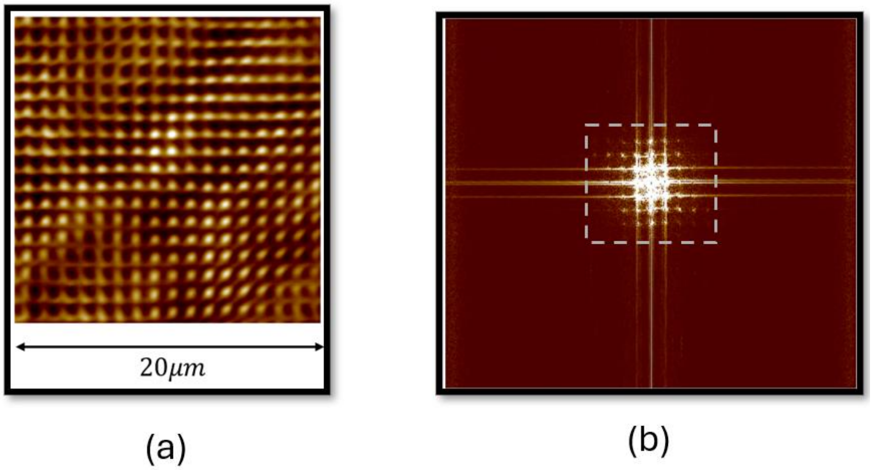

Figure 44. (a) $20\ \mu m \times\ 20\ \mu m$ *AFM image of metasurface with 4-fold symmetry in the IR region. (b) The corresponding FFT image of the metasurface showing square grid point pattern as outlined by the dashed square.*

The metasurface shown in Figure 44(a) was produced with a 488nm laser with an irradiance of $85\frac{mW}{cm^2}$ and an exposure time of 180 seconds. The metasurface has a pitch Λ value of $1104\ nm$ with an average depth of the gratings ranging between 30 nm and 45 nm. The patterns were produced using a dual pyramid system. The two pyramids used were of $\alpha_1 = 10^o$ and $\alpha_2 = 30^o$ respectively, where the pyramid with base angle $\alpha = 30^o$ was positioned after the focal plane of the first. As was the case in Section 4.3, taking the FFT of Figure 44(a) reveals patterns consistent with a 4-fold rotational symmetry, as shown in Figure 44(b). For spectrometer measurements, as described in previous sections of this chapter, using the optical setup presented in Section 3.5.1, an SPR dip was observed at 1180 nm, with the results presented below.

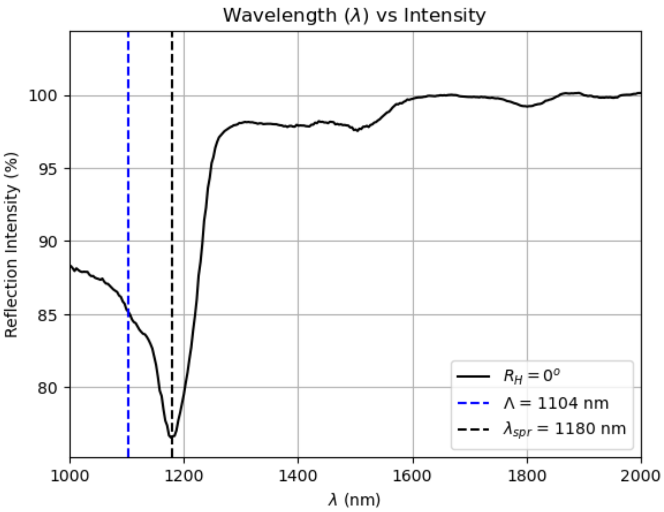

Figure 45. Shows the corresponding SPR reading for Figure 44 and was taken with a spectrometer set to read in NIR. All readings are done at a normal to the sample surface ($R_v = 0^o$).

As done in previous sections of this chapter, the expected λ_{SPR} can be calculated in accordance with equation (38) as the following,

$$\lambda_{SPR} = \Lambda\left(\sqrt{\frac{(\epsilon_{\mathrm{r},1}\epsilon_{\mathrm{r},2})}{(\epsilon_{\mathrm{r},2}+\epsilon_{\mathrm{r},1})}}\right) = 1175nm(1.064620562) \approx 1250\, nm$$

$$\%\, error = \frac{|Experimental\ - Expected|}{Expected} \times 100 = \frac{|\, 1180 - 1250|}{1250} \times 100\ \approx 5.6\,\%$$

Where the expected pitch Λ calculation is based on equation (60) following a (-, -, +) sign convention:

$$\Lambda = \frac{\lambda}{2\sin(\theta(\alpha_2, \alpha_1))} = \frac{488nm}{2\sin(\theta(30^o, 10^o))} = 1175\, nm$$

Experimental pitch observed:

$$\Lambda_O = 1104\, nm$$

$$\%\, error = \frac{|Experimental\ - Expected|}{Expected} \times 100 = \frac{|\, 1104 - 1175|}{1175} \times 100\ \%\ \approx 6\,\%$$

As shown through the calculations, the deviation for the SPR wavelength is 5.6% from the expected response, and the pitch value deviates by 6% from the intended design. In addition to the possible sources of error discussed in Section 4.4—specifically, slight misalignment with the polarization axis and uncertainty in pitch measurements—the relatively high deviations observed in this fabrication may also be attributed to the complexity associated with the dual-pyramid system. Since this setup relies on the precise alignment of both pyramids, even minor misalignments during the optical configuration (as shown in Figure 22, Section 3.2) could have contributed to the observed error.

Furthermore, it should be noted that, unlike the SPR measurements for the metasurface presented in Figure 42 (provided in section 4.4), a second SPR response with lower order resonance was not observed on the spectrometer. If there were a secondary response, it would be slightly above the visible spectrum at approximately 830 nm. However, no SPR response was observed in that region with the spectrometer set to visible. This could be due to the secondary response being extremely weak and obscured by the background noise.

4.6 SPR measurements for metasurface with 6-fold symmetry in the IR region

SPR measurement from plasmonic metasurface with patterns exhibiting 6-fold rotational symmetry is shown here. Below is the image of the metasurface produced with the 6-face PIL technique from a dual pyramid system with a pitch size residing in the IR region,

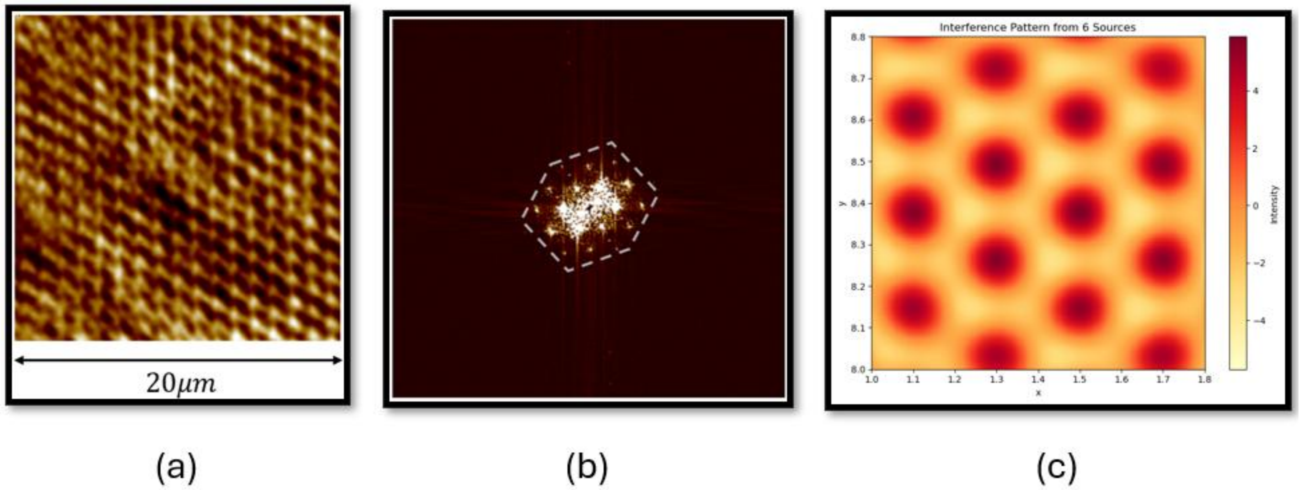

Figure 46.(a) $20\ \mu m\ \times\ 20\ \mu m$ *AFM image of metasurface with 6-fold rotational symmetry in the IR region. (b) Fast Fourier Transform (FFT) of the corresponding image showing the emergent hexagonal pattern outlined by the dashed lines (c) Simulated pattern for a 6-face PIL.*

The metasurface shown in Figure 46 (a) was produced with a 488nm laser at an irradiance of $167\frac{mW}{cm^2}$ and an exposure time of 60 seconds. The metasurface has a pitch Λ value of $1171\ nm$, with an average depth of the gratings ranging between 22 nm and 50 nm. The patterns were produced using a dual pyramid system. The two pyramids used were of $\alpha_1 = 10^o$ and $\alpha_2 = 30^o$ respectively, where the pyramid with base angle $\alpha = 30^o$ was positioned after the focal point of the first. Comparing the simulated pattern for 6-face PIL in Figure 46 (c) to the actual pattern in Figure 46 (a), it is noticeably different. However, upon further inspection, taking the FFT of the image reveals a tilted and compressed hexagonal structure, as shown in Figure 46(b). This may be due to a slight change in beam polarization [30]. Another possible reason is the area chosen for the AFM image, as the pattern appears to vary from one location to another on the fabricated surface.

The SPR measurements were collected using the optical setup illustrated in Figure 27 (see Section 3.5.1), where the polarizer was rotated in 45° increments up to 180°, which is equivalent to rotating the sample around the RH axis by the same increments. At $R_{\mathrm{H}} = 0^o$, two distinct SPR responses were observed at wavelengths of 1245 nm and 1082 nm. While the overall intensity of the reflection appeared to change with changes in the polarization angles, the positions of the SPR dips remained essentially unchanged, suggesting that the resonance conditions were not significantly affected by the change in polarization angle. The SPR measurement results for the metasurface patterned with 6-fold rotational symmetry are presented in Figure 47.

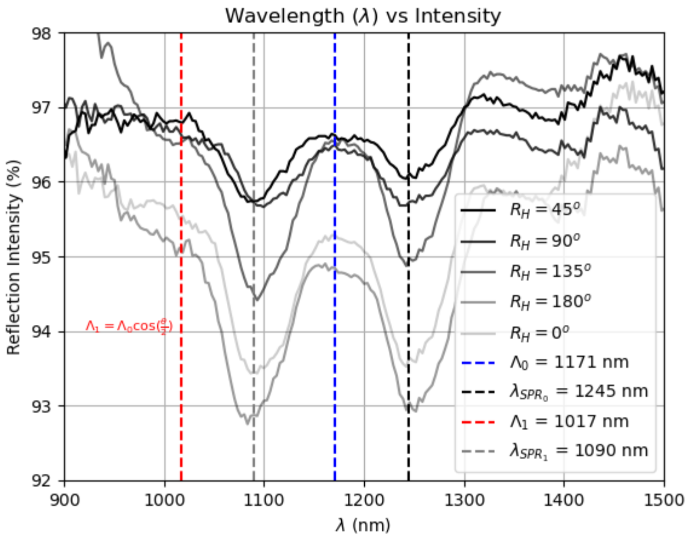

Figure 47. Shows the corresponding SPR reading for Figure 43 (a) and was taken with a spectrometer set to read in NIR. All readings are done at a normal to the sample surface ($R_v = 0^o$).

As can be seen from figure 47, the linear polarization of the incident light was rotated in increments of 45^o up to $R_H = 180^o$ rotation. The SPR dips shown in Figure 47 are indicated by the black and grey dashed lines. It is also evident that the reflection intensity varies with the polarization angle, likely for the same reason discussed in Section 4.2. The periodic structure does not couple equally to all polarization directions and surface undulations. As the polarization is rotated, its alignment with the dominant grating vectors decreases, resulting in weaker SPR excitation and reduced resonance intensity. Another explanation for the change in intensity is variations in metasurface depth resulting from the fabrication process. Previous research has shown that in interference-based lithography, the exposure profile can produce differences in structure depth [106]. Considering that SPR coupling is affected by both symmetry and feature depth, these factors may be the reasons behind the observed intensity changes. In the graph shown in Figure 47, the blue line shows the observed pitch value, while the red line shows the expected pitch value for the secondary absorption dip. This secondary dip appears consistently across measurements, prompting further investigation into its origin, which may be linked to the nanostructure geometry present in the metasurface. As such, it is hypothesized that the presence of a secondary absorption dip is connected with the geometry of the hexagonal pattern, the illustration of which is presented Figure 48.

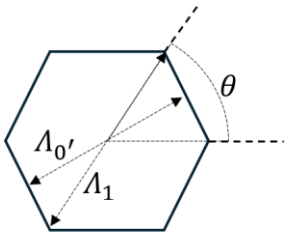

Figure 48. Hexagonal structure geometry with representation of the primary pitch $\Lambda_{0'}$ and the lower order pitch Λ_1.

As shown in Figure 48, the pitch size Λ_0 indicates the pitch measured for the structure, while Λ_1 represents a lower order pitch for the hexagonal structure. The lower order pitch can be determined using trigonometry. Where the expected pitch Λ_O the calculation is based on Equation (60), following a (-, -, +) sign convention. Here Λ_1 Is calculated first:

$$\Lambda_1 = \frac{\lambda}{2\sin(\theta(\alpha_2, \alpha_1))} = \frac{488}{2\sin(\theta(30^o, 10^o))} = 1175\, nm$$

Based on the geometry shown in Figure 46, the following can be calculated for the expected pitch $\Lambda_{O'}$:

$$\theta = \frac{360^0}{6} = 60^0$$

$$\Lambda_{O'} = \Lambda_1\, cos\left(\frac{\theta}{2}\right) = 1175\, nm\left(\frac{\sqrt{3}}{2}\right) = 1017\, nm$$

If the secondary dip observed is a result of the geometry of the patterned structures, then the expected SPR response for that pitch should be close to the one observed. As such, similar to work done in the previous section of this chapter, the expected λ_{SPR} can be calculated by equation (38) as the following,

$$\lambda_{SPR_1} = \Lambda_1\left(\sqrt{\frac{(\epsilon_{\mathrm{r,1}}\epsilon_{\mathrm{r,2}})}{(\epsilon_{\mathrm{r,2}} + \epsilon_{\mathrm{r,1}})}}\right) = 1017nm(1.064620562) \approx 1082\, nm$$

$$\%\, error = \frac{|Experimental\ - Expected|}{Expected} \times 100 = \frac{|\, 1090 - 1082|}{1082} \times 100\ \approx 0.7\ \%$$

Experimental pitch observed for the primary pitch Λ_o :

$$\Lambda_o = 1171\, nm$$

$$\%\, error = \frac{|Experimental\ - Expected|}{Expected} \times 100 = \frac{|\, 1171 - 1175|}{1175} \times 100\ \%\ \approx 0.3\ \%$$

Theoretical calculation of SPR absorption dips in accordance with equation (38):

$$\lambda_{SPR_O} = \Lambda_0\left(\sqrt{\frac{(\epsilon_{\mathrm{r,1}}\epsilon_{\mathrm{r,2}})}{(\epsilon_{\mathrm{r,2}} + \epsilon_{\mathrm{r,1}})}}\right) = 1175nm(\, 1.064620562) \approx 1250\, nm$$

$$\%\, error = \frac{|Experimental\ - Expected|}{Expected} \times 100 = \frac{|\, 1245 - 1250|}{1250} \times 100\ \approx 0.4\ \%$$

As shown through the calculations, the deviation for the lower SPR wavelength (λ_{SPR_1}) is 0.7% from the expected response, with its associated pitch (Λ_o) having a deviation 0.3%. In addition, the higher SPR wavelength (λ_{SPR_0}) has a deviation of 0.4% from the experimentally observed value. Furthermore, the SPR response was also measured using non-polarized light; the results are presented below.

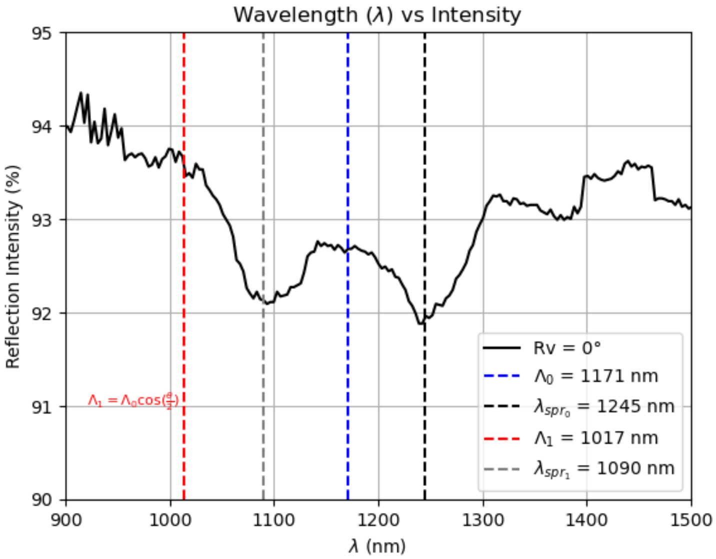

Figure 49. Shows the corresponding SPR reading for the metasurface presented in Figure 46 (a) and was taken with a spectrometer set to read in NIR. The main distinction here is that the readings were taken from non-polarized light reflecting off the metasurface. All readings are done at a normal to the sample surface ($R_v = 0^o$).

As can be observed from Figure 49, the SPR responses occur at the same wavelength as those shown in the experimental results in Figure 47. Furthermore, attempts to fabricate 6-fold symmetric metasurfaces with periodicities in the visible range using the PIL technique were unsuccessful. The reasons for this pertain to the single-pyramid setup shown in Figure 21 (provided in Section 3.2), where the 488 nm laser beam was aligned directly along the optical axis, such that it propagated toward the vertex of the acrylic pyramid with $\alpha = 30^o$ base angle. This configuration caused the beam to concentrate near the vertex, producing an interference region where the azobenzene thin film resides. Upon visual inspection, it was observed that the optical quality near the vertex was compromised due to imperfections, possibly resulting from wear during prior experiments or insufficient polishing during fabrication. Any scratches or surface roughness at the vertex could have distorted the wavefronts, leading to further distortions in the interference pattern. A non-uniform patterned surface was still observed; however, the pattern quality was insufficient to support SPR after gold sputtering. In contrast, the dual-pyramid setup shown in Figure 22 (Section 3.2) directed the beam toward the outer regions of the second pyramid's faces, avoiding the vertex and instead interacting with areas of higher optical quality near the edges. This likely led to uniform interference patterns and more effective plasmonic structures, which successfully produced distinct SPR responses, as shown in Figures 47 and 49.

4.7 SPR measurements for metasurface with 8-fold symmetry in the IR region

Below is the image of a metasurface with 8-fold rotational symmetry in the IR region, produced using an 8-face PIL with a pitch size residing in the IR region.

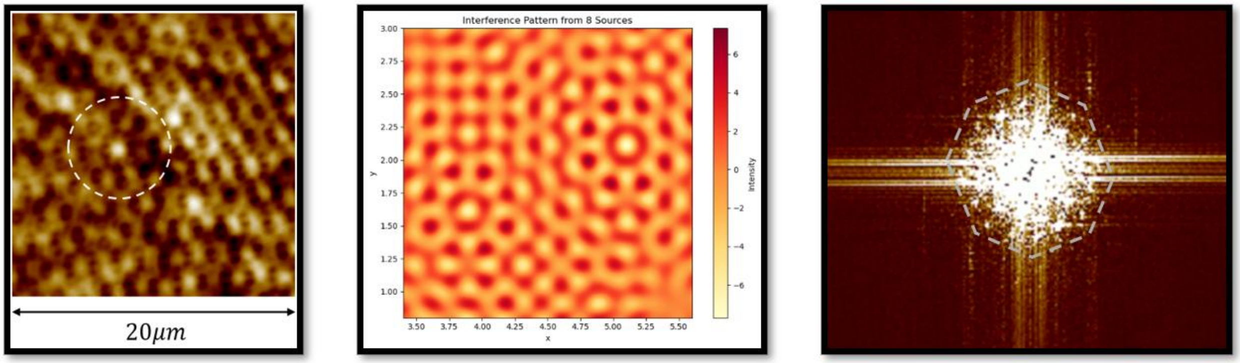

(a) (c) (b)

Figure 50. 20 μm × 20 μm AFM image of metasurface with 8-fold symmetry in the IR region. (b) Simulated pattern for a 8-face PIL (c) The corresponding FFT image of the metasurface showing the emergent octagonal pattern outlined by the dashed lines.

The metasurface shown in Figure 50 was produced with a 488nm laser with an irradiance of $95\,\frac{mW}{cm^2}$ and an exposure time of 90 seconds. The metasurface has a pitch Λ value of $1546\ nm$ for the long-range periodic order and an average depth of the patterned structure between 22 nm and 50nm. The patterns were produced using a single pyramid system with a base angle of $\alpha = 30^o$. Comparing the simulated image of the 8-face PIL shown in Figure 50(b) with the actual metasurface shown in Figure 50(a), the patterns exhibit similarity. Upon further inspection, the FFT of the image reveals a tilted octagonal structure, as shown in Figure 50(c). Figure 51 shows corresponding SPR measurements.

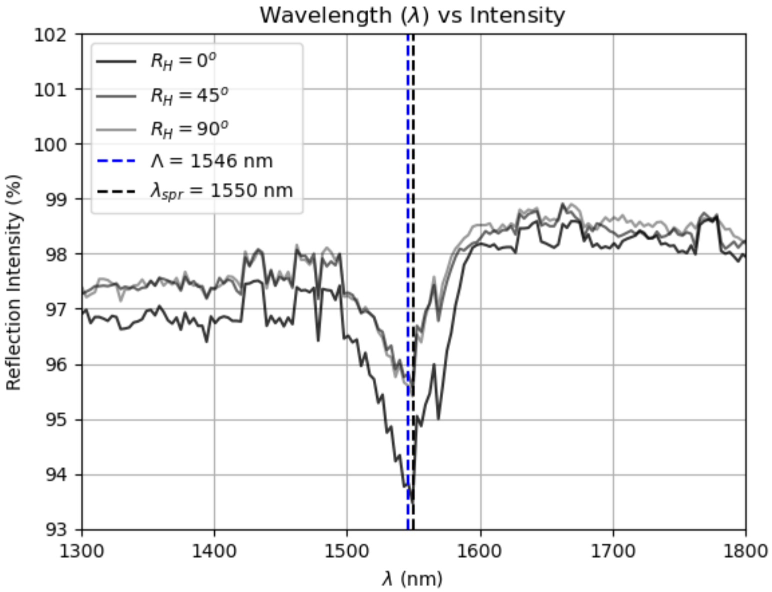

Figure 51. Shows the corresponding SPR reading for the metasurface presented in Figure 36 and was taken with a spectrometer set to read in NIR. The reading was taken with linearly polarized light reflecting off the fabricated surface area. All readings are done at a normal to the sample surface ($R_v = 0^o$)

Regarding the experimental results presented in Figure 51, the SPR absorption dip occurs at 1550nm when $R_H = 0^o$. Furthermore, the light polarization was rotated in increments of 45^o up to $R_H = 90^o$. No shift in the wavelength response was observed under these rotations. The blue dashed line denotes the pitch value of the grating, and the black dashed line indicates the wavelength at which the peak of the observed SPR response lies.

Since this is a quasi-crystal pattern, it lacks translational periodicity [30]. However, the analysis here is still based on what would have been expected considering that the intended design follows with pitch value as per equation (38) to compare with symmetries that do follow translational periodicity. The expected λ_{SPR} can be calculated by equation (38) as the following,

$$\lambda_{SPR} = \Lambda\left(\sqrt{\frac{(\epsilon_{\mathrm{r},1}\epsilon_{\mathrm{r},2})}{(\epsilon_{\mathrm{r},2}+\epsilon_{\mathrm{r},1})}}\right) = 783\,nm(1.064620562) \approx 833\,nm$$

$$\%\,error = \frac{|Experimental\ - Expected|}{Expected} \times 100 = \frac{|\,1550 - 833|}{833} \times 100\ \approx 86\,\%$$

Expected pitch Λ_O calculation based on equation (54) as the following:

$$\Lambda = \frac{488nm}{2\sin(\sin^{-1}(n_2\,sin(30^o)) - 30^o)}\ \approx\ 783\,nm$$

Experimental pitch observed:

$$\Lambda = 1546\ nm$$

$$\%\ error = \frac{|Experimental\ - Expected|}{Expected} \times 100 = \frac{|\ 1546 - 783|}{783} \times 100\ \approx 97\ \%$$

Based on the above deviations of 86% for the SPR response λ_{SPR} and 97 % for the pitch value Λ, it is reasonable to assume that the metasurface with 8-fold rotational symmetry necessitates a different model to predict periodicity and SPR occurrence more accurately. Surface plasmons on such metasurfaces showing quasi periodic structures have been studied in the past [107] and may provide a better insight or predictive methods for matching experimental data. Research looking into patterns for two-dimensional quasicrystals, specifically accessing for 8-fold rotational symmetry, have shown to exhibit scaling (or ratio) of periodicity between neighbouring points by a factor of either $\sqrt{2}$ and $1 + \sqrt{2}$ [108]. Using this factor, a hypothesised value for a pitch can be made by considering a long-range periodicity for an octagonal geometry as illustrated below in Figure 52.

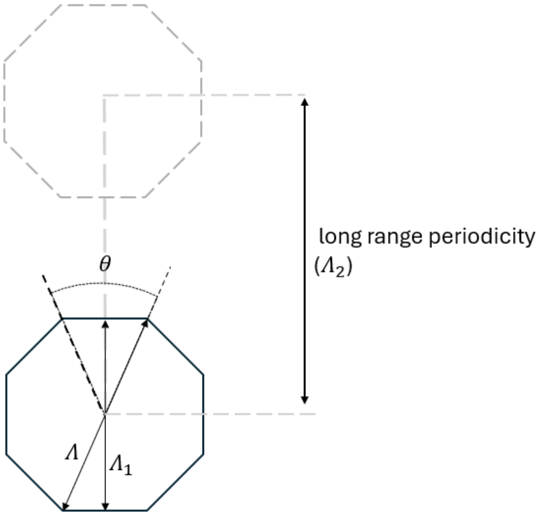

Figure 52. Octagonal structure geometry with representation of the expected primary pitch Λ and the lower order pitch Λ_1. The illustration assumes a long-range periodicity of the metasurface with value of Λ_2.

Based on the geometry presented in Figure 52, the lower order pitch (Λ_1) can be calculated as the following,

$$\theta = \frac{360^0}{8} = 45^0$$

$$\Lambda_1 = \Lambda\ cos\left(\frac{\theta}{2}\right) = 783\ nm(0.924) = 723\ nm$$

Supposing that the SPR response observed in the experiment is due to an average of the two scaling factors of $\sqrt{2}$ and $1+\sqrt{2}$, then the long-range periodicity can be determined as:

$$\Lambda_2 = \Lambda_1 \left(\frac{\sqrt{2}+1+\sqrt{2}}{2}\right) = 723\, nm \left(\frac{1}{2}+\sqrt{2}\right) \approx 1384\, nm$$

Comparing this with the experimental pitch observed yields the following percent error:

$$\%\, error = \frac{|Experimental\ - Expected|}{Expected} \times 100 = \frac{|\, 1546 - 1384|}{1384} \times 100\ \approx 12\,\%$$

Furthermore, the expected SPR response associated with the long order periodicity (Λ_2) can be calculated as:

$$\lambda_{SPR} = \Lambda \left(\sqrt{\frac{(\epsilon_{\mathrm{r},1}\epsilon_{\mathrm{r},2})}{(\epsilon_{\mathrm{r},2}+\epsilon_{\mathrm{r},1})}} \right) = 1384\, nm(\, 1.064620562) \approx 1473\, nm$$

Now, comparing the experimental SPR response to the expected yields the following:

$$\%\, error = \frac{|Experimental\ - Expected|}{Expected} \times 100 = \frac{|\, 1550 - 1473|}{1473} \times 100\ \approx 5\,\%$$

Based on the hypothesized pitch value, and assuming long-range order in the quasicrystal pattern, the calculated results yield a 12% deviation for the pitch value Λ_2 and a 5% deviation for the SPR response λ_{SPR} . It is important to note that quasicrystal patterns, such as those with 8-fold rotational symmetry [108], do not exhibit simple periodicity. Instead, they contain a multitude of periodicities which may be different from the one observed in this experiment and could account for the relatively high deviations. Nevertheless, these values represent a significant improvement compared to earlier estimates, which showed deviations of 86% and 97%, respectively. While the reduction in error is encouraging, the remaining discrepancies underscore the need for more accurate and robust predictive models to describe SPR behavior in quasicrystal patterned metasurfaces. Furthermore, the spectrometer measurements were also taken with non-polarized light. The data for which is presented in figure below.

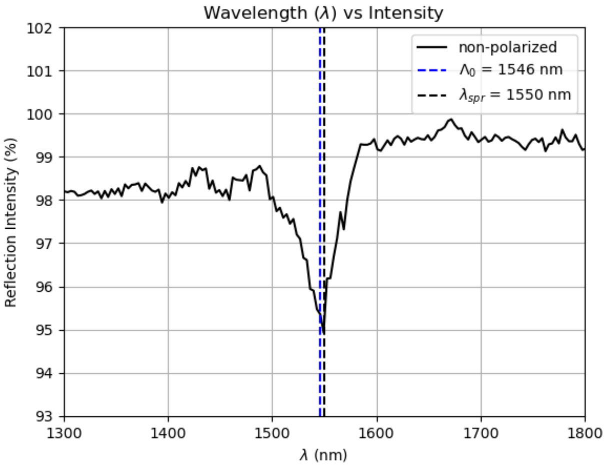

Figure 53. The reading was taken with non-polarized light reflecting off the fabricated surface area. All readings are done at a normal to the sample surface ($R_v = 0^o$).

The data presented in Figure 53 shows no change in the SPR response when non-polarized light was reflected off the metasurface.

4.8 Summary of SPR measurements for metasurfaces

To consolidate the findings from section 4.2 to 4.8, the following section presents a comprehensive summary of the key experimental results obtained from the fabricated metasurfaces. This includes the measured periodicities, surface plasmon resonance (SPR) wavelengths, and corresponding deviations from theoretical predictions across different metasurface symmetries and configurations. This data is organized in Table 1 below, showing a clear overview of how well the fabricated structures align with theoretical expectations.

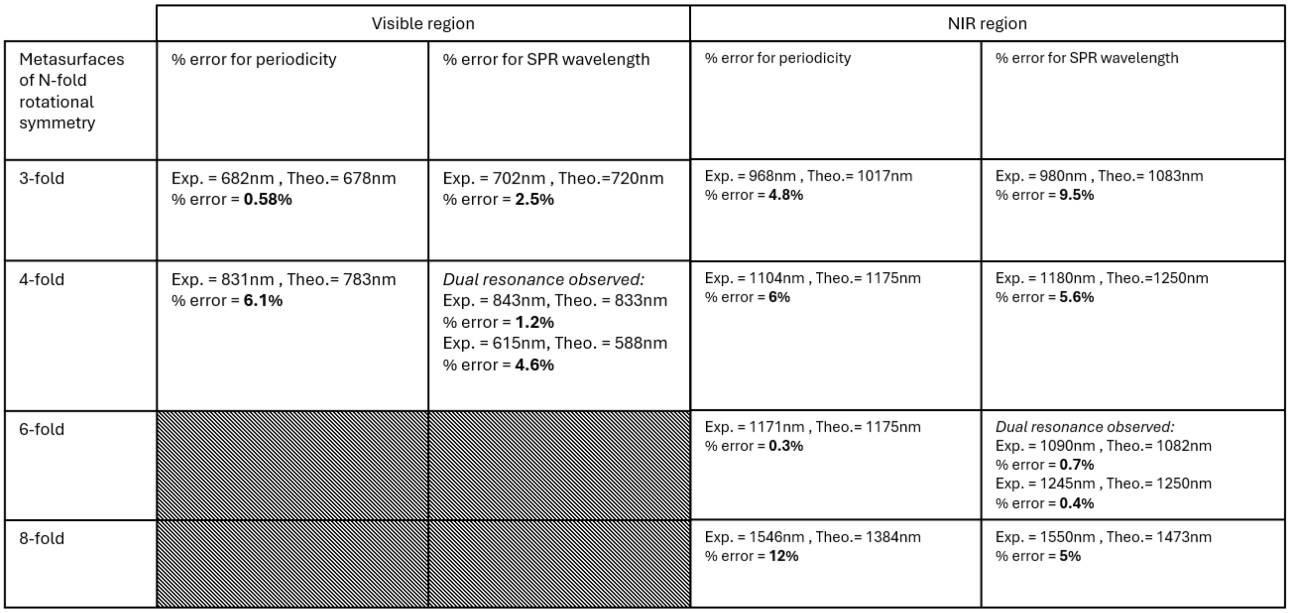

	Visible region		NIR region	
Metasurfaces of N-fold rotational symmetry	% error for periodicity	% error for SPR wavelength	% error for periodicity	% error for SPR wavelength
3-fold	Exp. = 682nm , Theo.= 678nm % error = **0.58%**	Exp. = 702nm , Theo.=720nm % error = **2.5%**	Exp. = 968nm , Theo.= 1017nm % error = **4.8%**	Exp. = 980nm , Theo.= 1083nm % error = **9.5%**
4-fold	Exp. = 831nm , Theo.= 783nm % error = **6.1%**	*Dual resonance observed:* Exp. = 843nm, Theo. = 833nm % error = **1.2%** Exp. = 615nm, Theo. = 588nm % error = **4.6%**	Exp. = 1104nm , Theo.= 1175nm % error = **6%**	Exp. = 1180nm , Theo.=1250nm % error = **5.6%**
6-fold	▨	▨	Exp. = 1171nm , Theo.= 1175nm % error = **0.3%**	*Dual resonance observed:* Exp. = 1090nm , Theo.= 1082nm % error = **0.7%** Exp. = 1245nm , Theo.= 1250nm % error = **0.4%**
8-fold	▨	▨	Exp. = 1546nm , Theo.= 1384nm % error = **12%**	Exp. = 1550nm , Theo.= 1473nm % error = **5%**

Table 1. Summary of periodicity and SPR responses for each metasurface.

As shown in table 1, during the analysis of the metasurface with 3-fold rotational symmetry, it was observed that the percentage deviation of the measured periodicities and the corresponding SPR wavelengths appeared larger for measurements taken in the near-infrared (NIR) region compared to those in the visible range. However, given that this observation was specific to a single metasurface configuration and was not consistently replicated across other metasurfaces with different rotational symmetries, it is likely a result of experimental variability rather than an inherent trend. This experimental variability may include minor misalignments in optical elements as their adjustment relied purely on visual inspection and any small offset can cause the metasurface structure to vary slightly from intended design. As such, no definitive correlation between increasing periodicity and error magnitude can be established from the current data. Further investigations across a broader set of samples would be required to determine whether this behavior is coincidental or indicative of a systematic effect.

4.9 SPR imaging for metasurface with 4-fold symmetry in the visible region

In this experiment, as mentioned in Section 3.5.2, light from a halogen source first passes through a linear polarizer, ensuring that only linearly polarized light reaches the sample. The sample is a gold metasurface exhibiting 4-fold symmetry with an underlying azobenzene layer. Upon reflection from the metasurface, the light then encounters a second polarizer, which has its polarization transmission axis oriented 90^o from the first. According to Malus Law, as presented in equation (14), this setup only allows light to pass through if the reflected light from the sample surface has undergone polarization rotation after reflection and is no longer parallel to the polarization axes of the second polarizer. In that case, the only way an image of the surface can be observed is if the plasmonic metasurface is altering the polarization state of the reflected light. To further acknowledge this, recent research has demonstrated that plasmonic metasurfaces can modify the polarization of light, effectively transforming it into a circularly polarized wave, which is a function typically achieved using a waveplate [109]. Thus, the metasurface can be imaged through similar polarization-altering behavior in reflection.

The following section presents the resulting SPR image produced from the metasurface with 4-fold rotational symmetry. The image was captured using the optical setup illustrated in Figure 27 (see Section 3.5.1), with incident light kept normal to the sample surface ($R_{\mathrm{v}} = 0^o$). However, the setup did not have a tunable light filter or a bandpass filter, meaning only polarized white light from the halogen source was reflected of the fabricated surface. The resulting image is presented in Figure 54 below.

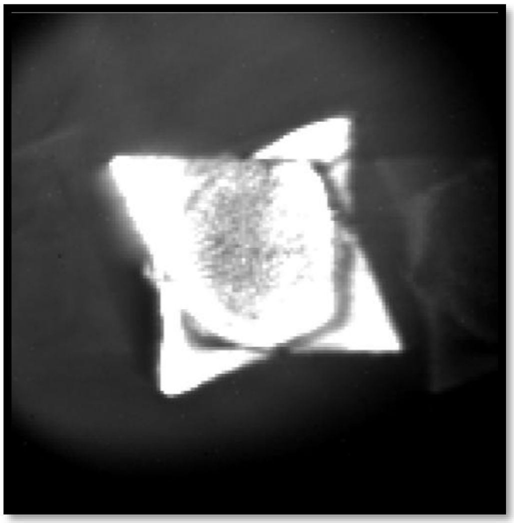

Figure 54. SPR image of metasurface with 4-fold symmetry captured with non-filtered light.

The image shown in Figure 54 is of the metasurface first presented in Figure 42(a), which is provided in Section 4.3. Since the optical setup used also includes a SPR spectrometer, the corresponding spectrometer reading for Figure 54 was obtained. These readings are presented in Figure 55.

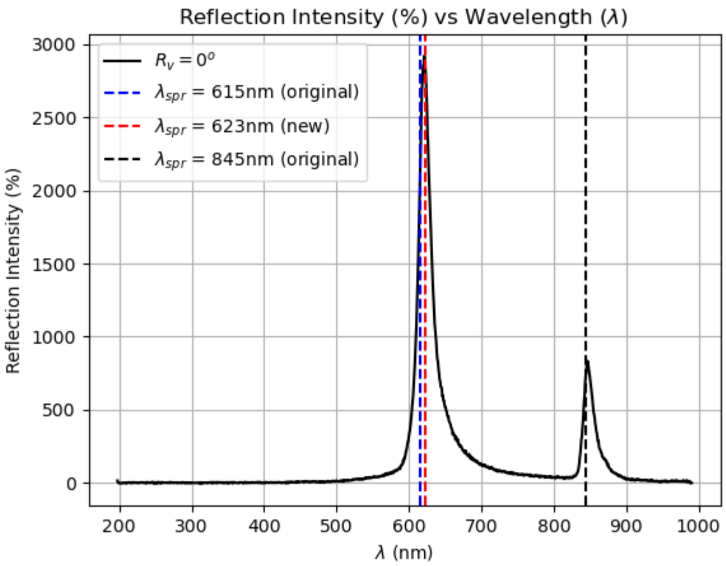

Figure 55. The spectrometer displays SPR peaks at 623 nm and 845 nm. Here, two reflection peaks are observed instead of absorption dips, as the setup blocks directly reflected light unless there is a change in the polarization state.

The graph shown in Figure 55 indicates that the SPR measurement for the secondary response, designated by the red dashed line, is slightly shifted from the previous measurement of the SPR wavelength for the metasurface, as indicated by the blue dashed line (see section 4.4, Figure 42). The black dashed line indicates the measurement for the primary response at 845nm and is still relatively the same as the one observed in Figure 42. However, compared to Figure 42, it appears to be shifted upward by 2 nm (from 843 nm to 845 nm).

Furthermore, it is essential to clarify that the unusually high reflection intensities reported in Figure 55—specifically, 1000% at an SPR wavelength of 845 nm and 3000% at 623 nm—which should be taken as artifacts of the referencing method rather than being indicative of enhanced SPR effects. These values result from referencing the measured intensities against a black background with minimal baseline illumination. In this setup, the reference spectrum was obtained by attempting to block as much light as possible, resulting in a reference intensity that approached zero. Consequently, when even modest amounts of reflected light were measured, the calculated relative intensity appeared artificially high. These elevated percentage values should, therefore, be interpreted with caution and not be attributed to physical enhancement mechanisms beyond standard SPR behavior.

Another interesting observation regarding this spectrometer data is that, despite the metasurface having an intended pitch design for 845 nm, the most prominent peak occurs at the secondary response.

4.10 SPR imaging for metasurface with 4-fold symmetry in the visible region using tunable filter

In Figure 55, the data collected was for the metasurface response to unfiltered light from the halogen source. However, to identify the specific wavelengths and to understand which regions of the surface are responsible for the SPR response, a tunable light filter can be introduced. The setup used for this experiment is the one presented in Figure 23 (provided in Chapter 3.5.2); however, the bandpass filter is not present. The results obtained using this setup are given below.

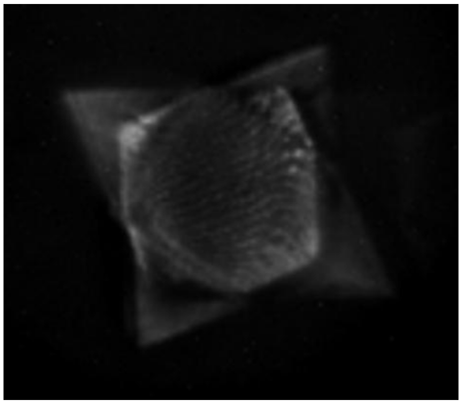

Figure 56. SPR image of metasurface patterned with 4-fold symmetry captured at a tuned wavelength of 615nm. The SPR peak, corresponding to this image, occurs at 621nm; the associated results are shown in Figure 57.

From Figure 56, it can be observed that edge regions of the metasurface exhibit stronger SPR responses compared to the central area. This variation is likely due to non-uniformities in the metasurface structure and grating depth across the fabrication area. While the central region maintains a 4-fold rotational symmetry, the edges deviate due to the uneven overlap of the interfering wavefronts that generate the pattern.

The intended 4-fold symmetric pattern requires the constructive overlap of all four refracted beams from the pyramidal prism. However, near the edges, not all wavefronts overlap fully, leading to variations in pattern geometry and depth. Specifically, at the triangular-shaped edges seen in Figure 56, the pattern transitions into linear gratings, resulting from the interference of only two overlapping beams. This shift from cross-gratings to linear gratings alters the structural symmetry but also introduces topographical changes, including variations in grating depth—both of which influence the observed SPR response. Research has shown that gratings depth can influence SPR response which may explain the changes in intensity across various regions of the fabricated surface [115].

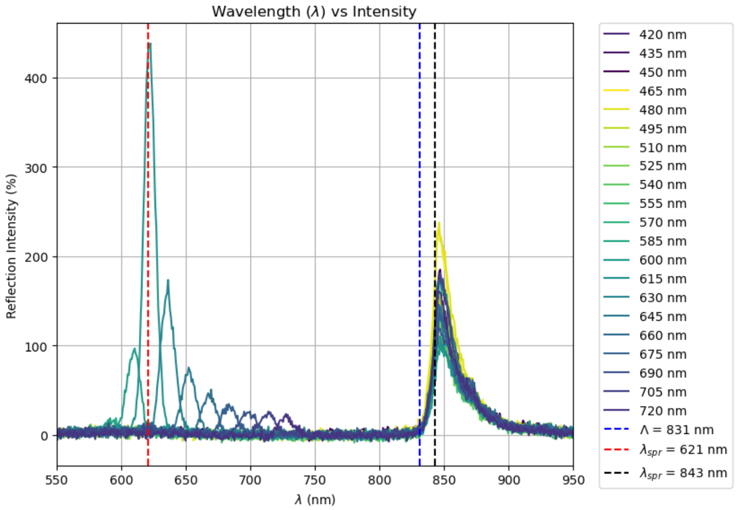

(a) Spectrographic readings across the full range of tuned wavelengths

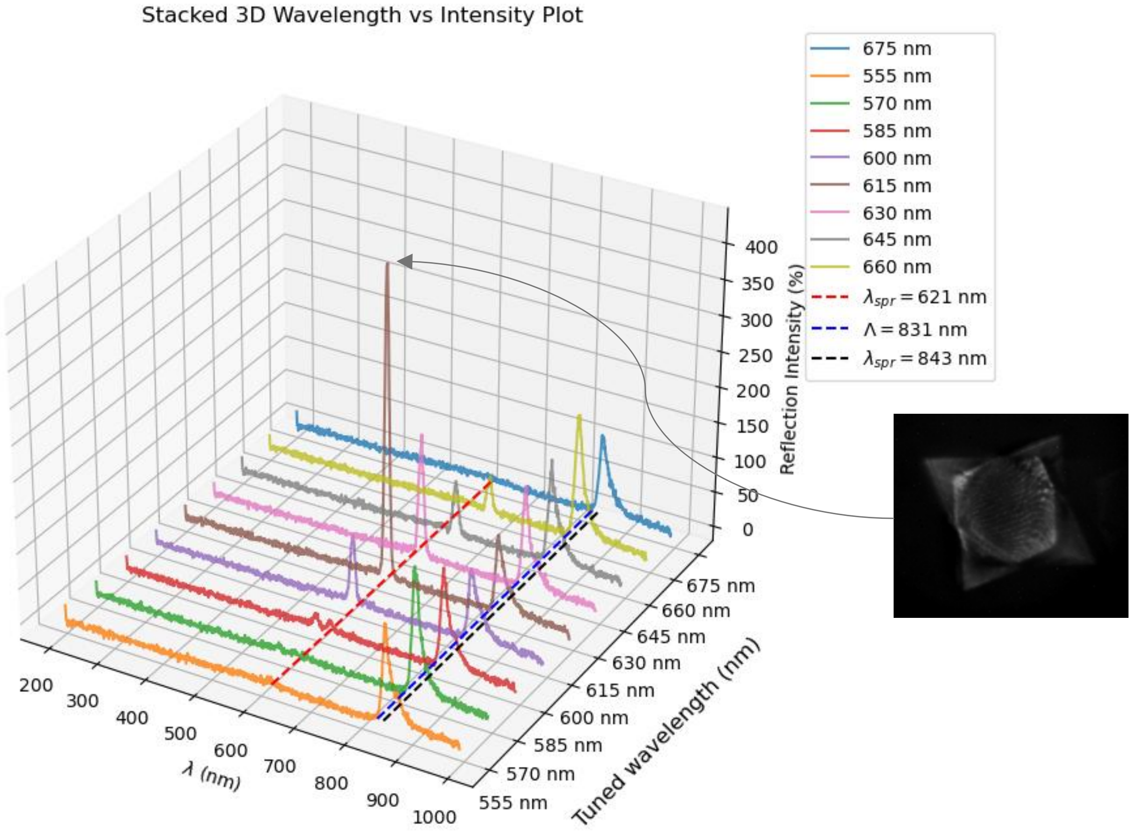

(b)

Figure 57. The spectrometer readings show the highest SPR peak when the tunable filter is set to a wavelength of 615 nm. (a) Shows the 2D spectrographic readings across the full range of tuned wavelengths. (b) Shows a 3D stacked wavelength vs intensity graphs for the selected range between 555 nm to 675 nm to better distinguish between spectrometer readings.

It can be noticed from Figure 57 that along with the SPR peak at 621nm (indicated by the red dashed line), there are also other peaks observed at 843 nm (indicated by the black dashed line) close to the pitch value of 831nm of the fabricated surface with 4-fold symmetry. The tunable filter used in this experiment allows selective observation of the SPR response within a wavelength range of 420 nm to 730 nm. However, the filter also permits light transmission beyond 800 nm, indicating that the crystal in the tunable filter allows near-infrared (NIR) light (wavelengths greater than 800 nm) to pass through. Consequently, SPR-related responses are still observed in this region, indicating that changes persist in the NIR range as the wavelength is tuned. To further isolate the signal around the 600nm range, it is required to filter out the NIR signals.

4.11 SPR imaging for metasurface with 4-fold symmetry with a bandpass filter

To determine which regions of the metasurface contribute to the SPR response at 615 nm, it is necessary to isolate the wavelength range where the most substantial SPR peak occurs. A bandpass filter was available in the lab, which permitted wavelengths between approximately 600 nm and 670 nm to pass through. The spectral transmission curve of this filter is presented below.

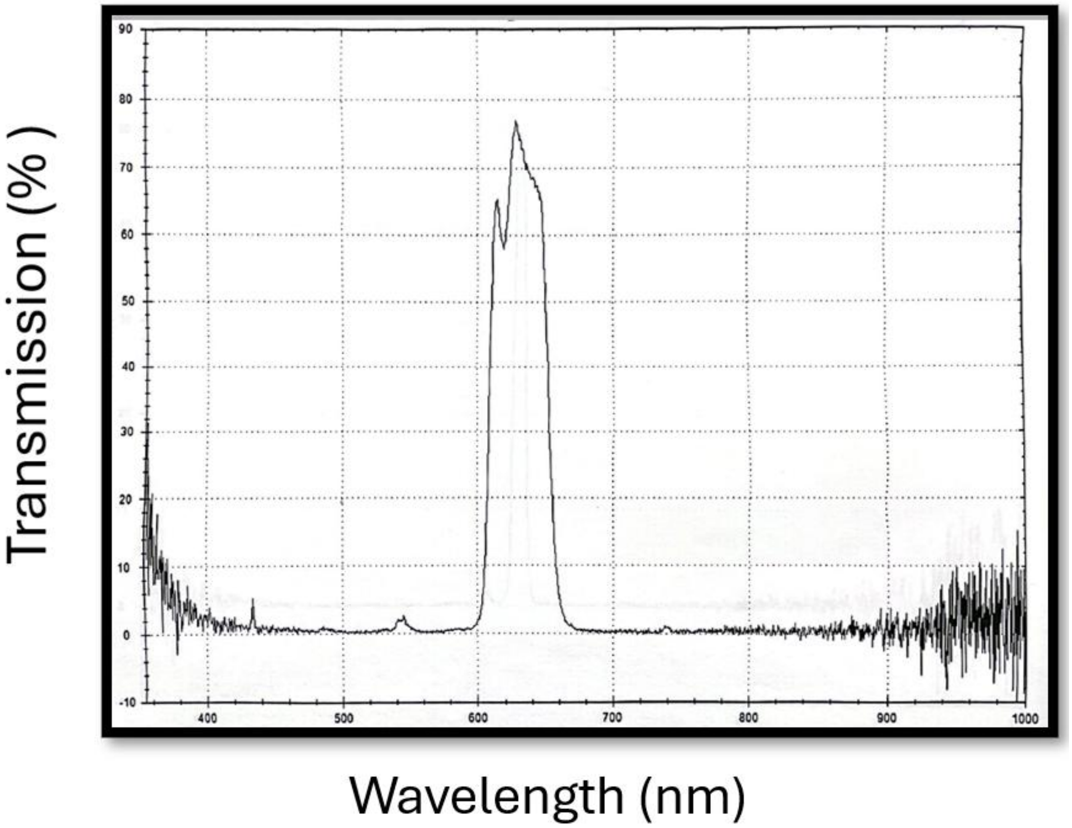

Figure 58. Spectral graph of the bandpass filter used to isolate transmission signal between 600nm to 670nm approximately.

As shown in Figure 58, the bandpass filter provided a sufficient spectral range, aligning with the data presented in Figures 57(a) and 57 (b), where the SPR response emerges around 590 nm and diminishes near 750 nm. This range effectively captures the highest SPR peaks, ensuring their inclusion in the experiment. In terms of the optical setup, this filter was placed in front of the tunable light filter, as shown in Figure 23 (provided in section 3.5.2). Under this setup, the results are presented in Figure 59.

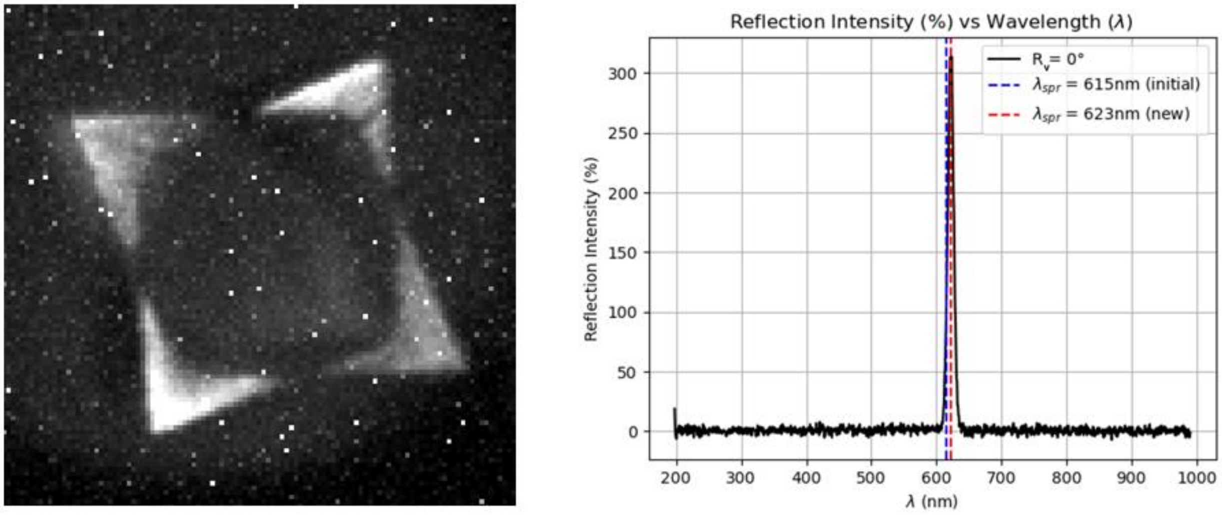

(a) (b)

Figure 59. (a) SPR image of metasurface with 4-fold symmetry using tunable filter in conjunction with bandpass filter. Confining the range to only be in between 590nm and 750nm. (b) Shows the SPR peak at 623nm (labeled new) when the visible light filter is tuned to 615nm (labeled initial).

Figure 59(a) shows the corresponding image to the spectrometer reading in Figure 59(b). The two figures indicate that when the wavelength was tuned to 615 nm, SPR excitation occurred at 623 nm along the edges of the structure. The activation of all four edges of the fabrication suggests that these edge structures are responsible for the peak observed at 615nm. Further results inspecting the edges of the fabrication are presented in Figure 60.

While it may be tempting to attribute the secondary absorption dip observed in Figure 40 (Section 4.3) to edge-related effects, this explanation is unlikely. In that experiment, the beam diameter was sufficiently small and positioned near the center of the sample, avoiding interaction with the edge structures. Provided the propagation length of SPW is between 10 and 100 microns [79], as previously mentioned in Section 2.1, this would not be possible unless the projected light on the sample is somehow reaching those edge regions. Additionally, it is worth noting that the secondary SPR responses differ between the two experiments: Figure 42 (Section 4.4) shows a resonance at 615 nm, whereas Figure 59(b) displays it at 623 nm. Further inspection of the edge structures through AFM is shown in Figure 60.

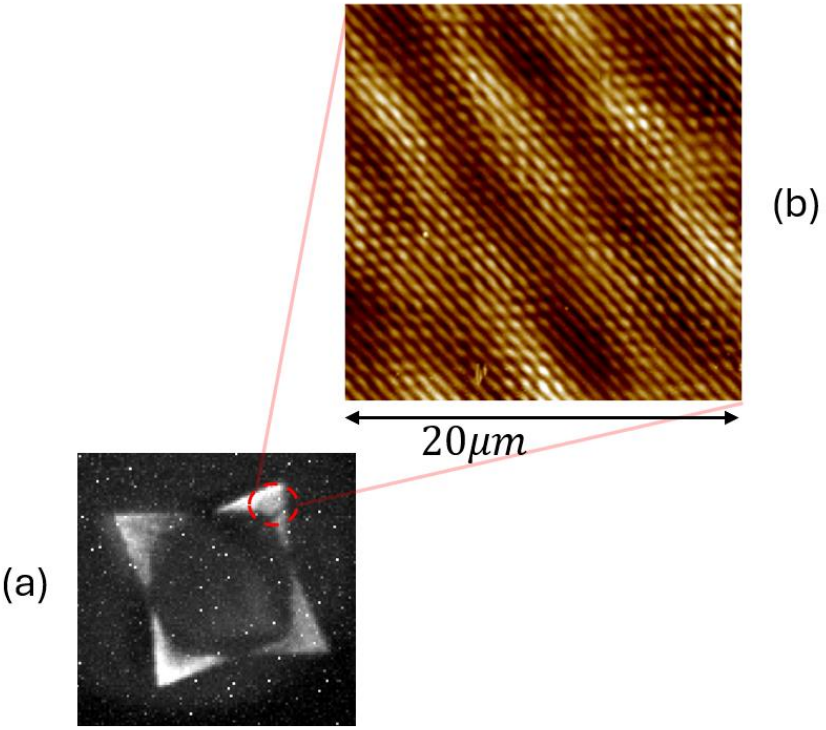

Figure 60. An inspection of the edge of the fabricated surface (a) reveals an SPR image of the metasurface with 4-fold symmetry (b), which indicates a pitch of 590 nm for the gratings, as determined by AFM imaging.

Based on Figure 60, which shows 590nm linear gratings at the edges, the corresponding λ_{SPR} can be calculated by equation (38) as the following,

$$\lambda_{SPR} = \Lambda\left(\sqrt{\frac{(\epsilon_{\mathrm{r},1}\epsilon_{\mathrm{r},2})}{(\epsilon_{\mathrm{r},2}+\epsilon_{\mathrm{r},1})}}\right) = 590\ nm(1.064620562) \approx 628\ nm$$

Comparing it to the observed value gives the following:

$$\%\ error = \frac{|Experimental\ - Expected|}{Expected} \times 100 = \frac{|\ 623 - 628|}{623} \times 100\ \approx 0.8\ \%$$

Based on the 0.8% deviation, it is hypothesized that the edge structures with a gratings pitch of 590 nm are causing the observed SPR response. To investigate whether similar phenomena occurred with other metasurfaces, the same experiment was conducted with a metasurface exhibiting 3-fold symmetry, which will be presented in the next section.

It should be noted that the tunable light filter can only tune wavelengths from approximately 450 nm to 720 nm, and no tunable filter was available for the NIR range to study the behavior of 845 nm pitch in a similar manner. Perhaps future research can investigate tuning into higher wavelengths to understand how a metasurface with 4-fold symmetry with an 845 nm pitch would behave.

4.12 SPR imaging for metasurface with 3-fold symmetry with non-filtered light

The optical set-up used for this experiment was the same as Figure 23 (see section 3.5.2), except that no filter was present. The results of this experiment are shown below.

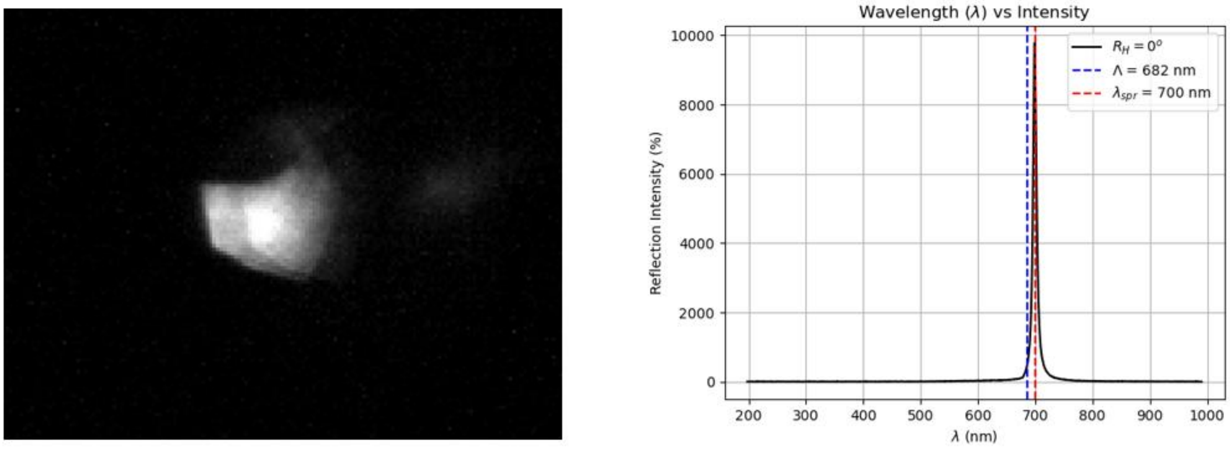

(a)

(b)

Figure 61. (a) SPR image of metasurface with 3-fold symmetry with non-filtered light. (b) Shows the SPR peak at 700 nm for a periodicity (pitch) of 682 nm.

From the above Figure 61(b), again —as mentioned in Section 4.8 — it should be noted that the extreme enhancement in reflection intensity of 10,000% are artificial and is not suggestive of something beyond standard SPR effects. Instead, it is most likely due to the intensity observed to the relative background.

In the context of the SPR response, the observed peak at 700 nm aligns with the expected result from Figure 35 (provided in Section 4.2). Again, to further investigate the area of the metasurface shown in Figure 35(a) that may be causing the response, a tunable filter is used. This is presented in the next section of the chapter.

4.13 SPR imaging for metasurface with 3-fold symmetry with Tunable light filter

Despite the reflection intensity shown in Figure 61(b), a visible light filter was used to gain further insight into which part of the metasurface structure was responsible for the observed peak and to verify the exact wavelength at which SPR excitation occurred. Thus, the optical setup used in this experiment was the same as that shown in Figure 23 (provided in Section 3.5.2), except that the band-pass filter was omitted. Scanning through different wavelengths in the visible region, the results of this experiment are presented below.

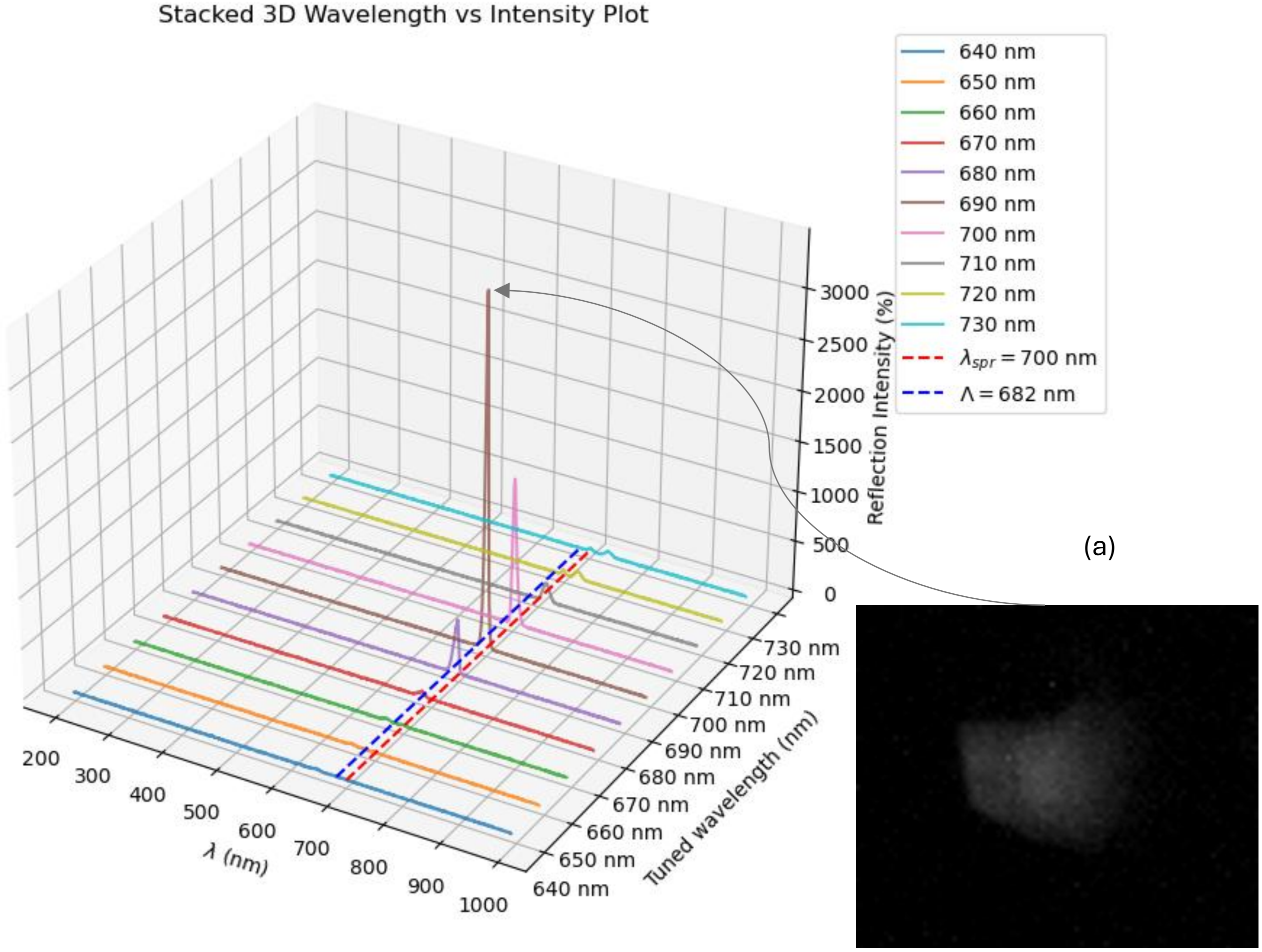

(b)

Figure 62. (a) SPR image of metasurface exhibiting 3-fold symmetry at a tuned wavelength of 690nm. (b) Shows the SPR peaks for varying tuned wavelengths, with an SPR wavelength of 700 nm shown by the red dashed line.

From Figure 62(b), the 690 nm tuned wavelength is responsible for the dominant SPR peak occurring at 700 nm. From figure 62(a), the areas that experience the highest enhancement in reflection intensity for the metasurface seem to be the entire fabricated surface without a clear distinction between certain regions activated over others on the fabricated structure. Thus, it is hypothesized that the whole surface is responsible for the SPR peaks observed in Figure 62(b).

4.14 Results for PIL using lens-pyramid system

As hinted at the end of chapter 4.1, the following demonstrates a proof of concept for the optical setup for PIL using a lens-pyramid system. This section also develops a curve-fitting equation to be used as a tool for future research in the fabrication of metasurfaces. The optical setup for the lens-pyramid system for PIL follows the theoretical formulation of equation (78) (provided in section 2.3.3), where a model was developed for a system in which the biconvex lens is positioned after the pyramid and before the focal point of the pyramid. The experiment was conducted using a 4-face pyramid and a lens with a focal length of 5 cm. The optical set-up for this experiment is shown in Figure 63.

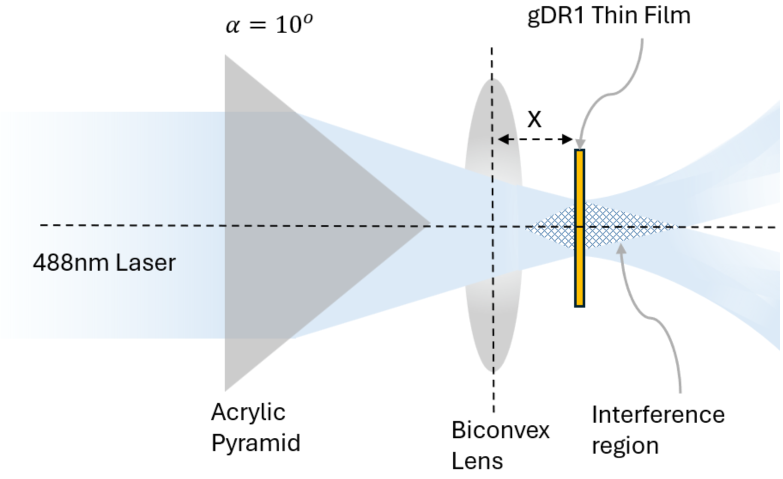

Figure 63. Optical set-up for pyramid lens system

In association with Figure 63, the following table shows the data that was collected measuring a range of pitches values Λ_{exp} over a distance x away from the lens:

x (mm)	Λ_{exp} (nm)
20	2056
23	2233
26	2473
29	2771

Table 2. Experimentally determined pitch Λ_{exp} over distance x

From Table 2, it can be observed that the pitch increases as the distance from the lens increases, showing an increasing trend. All fabrications to determine the experimental pitch data were produced with an irradiance of 167 $\frac{mW}{cm^2}$ and a 20s exposure. As per equation (85), the hypothesized function for the pitch is given by the following:

$$\Lambda_H = \frac{\lambda}{2\sin\left(\frac{1}{x^n}\right)}$$

The parameters used for this experiment are $\alpha = 10^o \left(\frac{\pi}{180^0}\right) \approx 0.1745$ and $\lambda = 488\ nm$. The material used for the pyramid is Acrylic; as such, the index of refraction is 1.49 ($n_2 = 1.49$). By equation (54), the theoretical pitch value Λ for a single pyramid system would yield the following:

$$\Lambda \approx \frac{\lambda}{2\sin(\sin^{-1}(n_2\, sin(\alpha)) - \alpha)} = \frac{488\ nm}{2\sin(\sin^{-1}(n_2\, sin(0.1745)) - 0.1745)} \approx 2790\ nm \tag{86}$$

Interestingly, the lens-pyramid system yields values for pitch that are smaller than those achieved with a single-pyramid system of 2802 nm. To get a model for this system, curve fitting was done by generating a value for n that minimizing the difference between the hypothesized pitch Λ_H values to the experimental value Λ_{exp} , keeping the experimental values fixed. This can be presented with the following algorithm:

$$\min_n \sum_{i=1}^{N} |\Lambda_H(n, x_i) - \Lambda_{exp}(x_i)| = \min_n \sum_{i=1}^{N} \left| \lambda \left(2\sin\left(\frac{1}{x^n}\right)\right)^{-1} - \Lambda_{exp}(x_i) \right| \tag{87}$$

Here n and x are input variables. The algorithm was implemented using the *scipy.optimize.minimize()* function in Python (see code in Appendix), which by default is set to the Nelder-Mead Simplex Method[110] [111]. The method minimizes the objective function ($2\sin\left(\frac{1}{x^n}\right) - \Lambda_{exp}(x_i)$) subject to constraints. As such, n was subject to be constrained in the range $0.1 \leq n \leq 5$.

In the optimization model, the range of $0.1 \leq n \leq 5$ was picked to maintain numerical stability. The lower bound of $n = 0.1$ was chosen to avoid division errors and ensure that n is neither zero nor negative. A value of $n = 0$ would yield a pitch size above 13000 nm (according to equation (85)), while negative values would cause the pitch to be in the submicron region; both scenarios are inconsistent with physical observations. Additionally, minimal values such as $n = 0.001$ would lead to a model that changes too slowly, again contradicting what's seen experimentally. For these reasons, it was reasonable to set the lower bound at 0.1.

The upper bound of $n \leq 5$ was chosen to prevent overfitting and ensure that the model remains within a reasonable range of experimental values. If n was too large, $\frac{1}{x^n}$ would decay rapidly, making $\theta(x)$ approach zero and leading to unrealistically large pitch values. This is again not what was observed experimentally, and as such, a reasonable assumption was made to choose 5. It should be noted that other values for the upper bound are possible to explore. However, this could be a matter of future exploration to have a better model.

Based on the data collected in Table 2, the model determined an optimal value of $n = 0.71$. Leading to the following expression for the hypothesised pitch:

$$\Lambda_H = \frac{\lambda}{2\sin\left(\frac{1}{x^{0.71}}\right)} \tag{88}$$

Furthermore, Figure 64 shows the comparison between the developed model and the experimental observations.

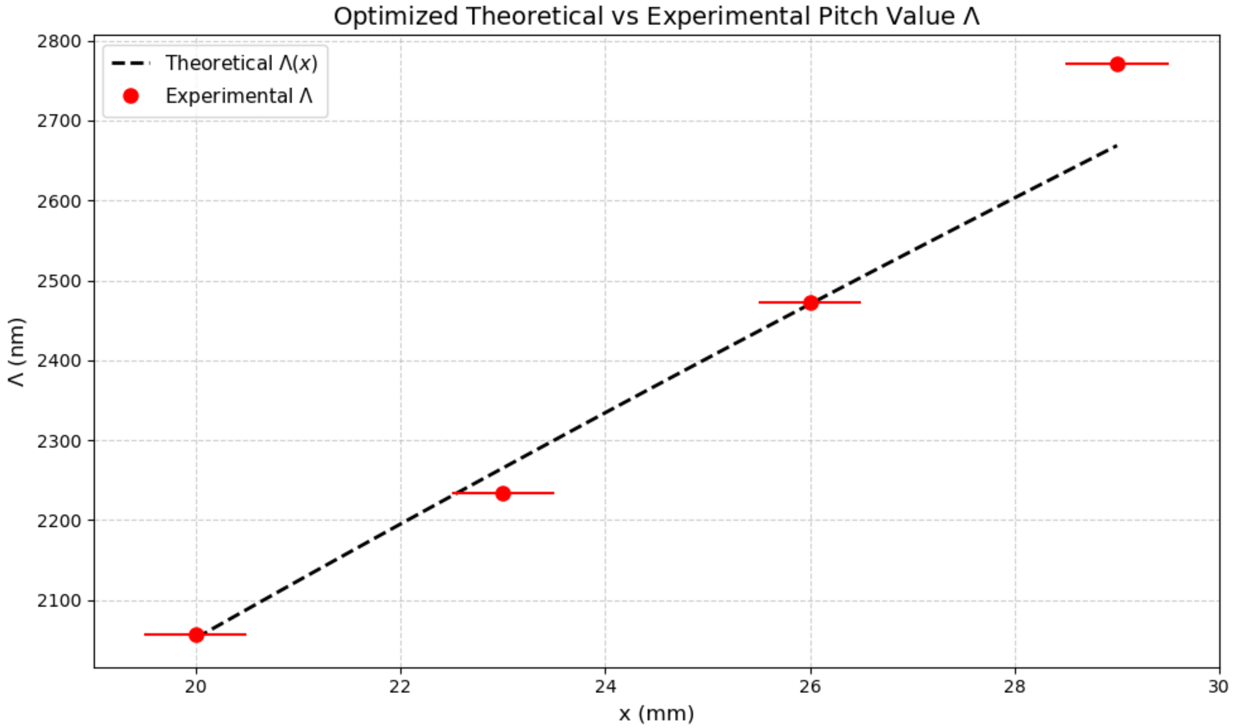

Figure 64. PIL with 4-faced pyramid (α = 10°) and a lens with a focal length of 5cm. All experimental values (red dots) were obtained with an irradiance of $167\frac{mW}{cm^2}$ *and a 20-second exposure, resulting in an approximate depth of 30 nm.*

From Figure 64, the data follows the hypothesized inverse relationship between $\theta(x)$ and x. As mentioned earlier, the experimental values are smaller than those generated by a single-pyramid system, as provided in Equation 86. This suggests that the lens increases the final refracted angles, thereby leading to lower pitch values that are not achievable by the pyramid alone. Furthermore, the pitch value changes as the sample moves greater distances away from the pyramid, thus validating the tunability of pitch. In addition, as per Figure 64, the error for the caliper readings to measure the distance between the biconvex lens and the sample of $\pm 0.05\ mm$ are included via red error bars. It is important to note that the last experimental data point should not be considered as an outlier since the fitting function itself can be further optimized.

It is essential to note that the hypothesized pitch equation can be utilized as an experimental tool to determine the sample position required to fabricate pitches of a desired size, and it is not an exact equation for the lens-pyramid system being analyzed.

Finally, Figure 65 provides an example of the metasurface with 4-fold rotational symmetry produced using the lens-pyramid system, where the lens was positioned after the pyramid.

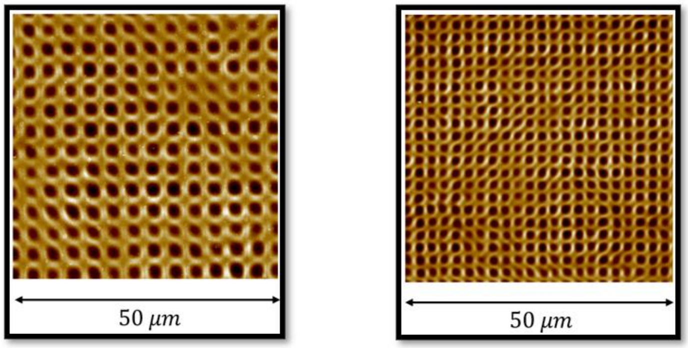

(a) (b)

Figure 65. Proof of concept for lens-pyramid system for pitch adjustability. (a) Shows the fabrication resulting from 4-face PIL (α =10°). Done at $160 \frac{mW}{cm^2}$ *and 120s exposure. With an approximate depth of 45 nm and pitch of 4 µm. (b) Shows the fabrication resulting from 4-face PIL (α =10°) with a biconvex lens (focal length of 5cm) positioned in front of the pyramid. Fabricated with* $160 \frac{mW}{cm^2}$ *and 20s exposure. With an approximate depth of 30 nm and a pitch of 2.3 µm.*

It is important to note that the pitch size observed in Figure (b) is approximately 1.7 times smaller than that in Figure (a). The results shown in Figures 64 and 65 demonstrate proof of concept for pitch reduction using a lens-pyramid system. Additionally, the figure highlights the potential to generate a tunable range of pitch sizes.

Future work could explore an exact or more optimized equation to model the lens-pyramid system or perhaps have a simulation for such as model in order to determine the pitch based on the distance between the sample and the lens-pyramid system.

Chapter 5: Conclusion

This study, for the first time, performed SPR imaging of plasmonic metasurfaces developed using the PIL technique. The research focuses on designing and fabricating plasmonic metasurfaces, followed by their structural characterization and analysis. To prepare the samples, azobenzene-based thin films were spin-coated onto cleaned glass substrates. These films were subsequently patterned using the PIL technique. Before fabrication, Python simulations were developed to help visualize and understand the multi-beam interference patterns responsible for the resulting metasurface structures. The simulated patterns closely resembled those observed experimentally.

The research further investigated the use of PIL to fabricate plasmonic metasurfaces with varying rotational symmetries and evaluated their SPR behavior. The PIL technique employed pyramids with different numbers of faces, including 3-face, 4-face, 6-face, and 8-face pyramids. These pyramids produced metasurfaces with patterned structures exhibiting 3-, 4-, 6-, and 8-fold rotational symmetries, respectively. Additionally, quasicrystal patterns were formed when 8-face PIL was used. Each patterned metasurface had its grating periodicity measured and characterized.

Plasmonic metasurfaces with 3-fold symmetric patterns were fabricated with two different pitch sizes—one in the visible region and one in the IR. The visible pitch was produced using a single-pyramid system, while the IR structure was fabricated using a dual-pyramid setup. For the patterned surface in the visible region, the SPR wavelength deviated by 2.5% from the expected value and the pitch by 0.58% from the intended design. For the metasurface exhibiting 3-fold rotational symmetry and periodicity in the IR range, the SPR wavelength deviated by 10% and the pitch by 4.8%.

Metasurfaces patterned with 4-fold rotational symmetry were also fabricated with periodicities in both visible and IR. In the visible range, the plasmonic metasurface was patterned using a single pyramid system, exhibiting an SPR deviation of 1.2% and a pitch deviation of 5.8%, as well as a secondary SPR response that deviated by 4.6%. The IR version of this metasurface was made using a dual pyramid system, exhibiting a 5.6% deviation in SPR wavelength from the expected value and a 6% deviation in pitch from the intended design.

Regarding plasmonic metasurfaces exhibiting 6-fold rotational symmetry, only periodicities in the IR were produced, and no successful patterning could be done for the visible. The metasurface was patterned in the IR range using a dual pyramid system. Furthermore, it showed excellent agreement with predictions, with its SPR wavelength deviating by only 0.4% and its pitch by 0.3%. A secondary SPR response was also observed, deviating 0.7% from the expected value.

Metasurfaces patterned with 8-fold rotational symmetry showed a quasicrystal pattern. Furthermore, the SPR wavelength and pitch deviated significantly—by 5% and 12%, respectively—highlighting the need for improved models designed to predict properties of metasurfaces with aperiodic structures.

Additionally, SPR imaging was performed on plasmonic metasurfaces exhibiting both 3-fold and 4-fold rotational symmetries. For the 4-fold symmetry, two distinct SPR responses were observed, with further analysis revealing that edge features contributed to the secondary peak. Regarding the metasurface with 3-fold rotational symmetry, no specific localized region was identified as being responsible for its SPR response.

Furthermore, this work demonstrated a proof of concept for dual-pyramid systems, which enable pitch sizes not achievable with single-pyramid setups. Finally, this work also demonstrated the potential of a lens-pyramid system to generate tunable pitch ranges.

Several observations made during this study present valuable opportunities for future investigation. Notably, the metasurface with 3-fold rotational symmetry with periodicities in the IR region exhibited a significant 10% deviation in its SPR response and a 4.8% deviation in pitch from the expected values. Understanding the exact cause of this substantial discrepancy could help improve the accuracy and consistency of metasurface fabrication.

Moreover, the metasurfaces produced using the 8-face PIL technique, which resulted in quasicrystal-structured patterns, showed substantial deviations from the predicted values -5 % for the SPR response and 12% for the pitch. Future work could consider developing and/or applying new theoretical models that account for the unique structural and optical characteristics of quasicrystal patterns to improve the predictive accuracy of periodicity and SPR wavelengths.

Furthermore, equipment limitations restricted further SPR imaging of the 831 nm pitch structures on the metasurface with 4-fold rotational symmetry, primarily due to the lack of a tunable filter capable of spanning both visible and near-infrared (NIR) wavelengths. Incorporating broader spectral imaging capabilities in future studies would enable a more comprehensive investigation of the light-matter interactions in these structures.

In addition, depending on the target application, plasmonic metasurfaces with tailored geometries and resonant properties can be engineered to support highly sensitive spectroscopic techniques such as Metasurface-Enhanced Infrared Spectroscopy (MEIRS), which enables real-time, label-free biosensing of live cells [112]. Previous research in our lab has successfully demonstrated the patterning of metasurfaces with various rotational symmetries at the micron scale [30]. Building on that foundation, future work could focus on fabricating metasurfaces with precisely tuned pitch and depth in the visible and near-infrared regimes using the PIL techniques explored in this thesis—specifically, the single-pyramid, dual-pyramid, and lens-pyramid systems. These fabrication techniques are scalable, cost-effective, and could eliminate the need for costly methods such as electron beam lithography (EBL). Leveraging PIL to produce metasurfaces could provide a more feasible approach for MEIRS and its use in biosensing platforms capable of extracting chemical information from cells in real time, drug testing, as well as provide analysis on how cells respond to stimuli [112].

The first successful implementation of SPR imaging on PIL-fabricated plasmonic metasurfaces is presented in this thesis. The study utilized azobenzene-based thin films and multi-beam interference to pattern rotationally symmetric metasurfaces, analyzing their depth and periodicity. Simulations of PIL were developed for visualization and displayed pattern formations that resembled those produced experimentally. SPR responses were observed for metasurfaces with 3-fold and 4-fold symmetries across both visible and infrared wavelengths. However, SPR responses were only observed in the infrared for metasurfaces with 6-fold and 8-fold symmetries. The deviations in SPR wavelengths and periodicities were generally within 10% error margins. Notably, the 6-fold symmetric metasurface in the IR demonstrated the highest accuracy, with SPR and pitch deviations of less than 1%. These findings highlight the versatility of PIL in producing plasmonic metasurfaces and their ability to be imaged through SPR.

Appendix A:

PIL simulation code:

```
# Sampling parameters
delta = 0.005  # spatial resolution
x = np.arange(-10.0, 10.0 + delta, delta)
y = np.arange(-10.0, 10.0 + delta, delta)
X, Y = np.meshgrid(x, y)

# Parameters
w = 1  # beam width (not used here but could be for Gaussian envelope)
lamda = 0.488  # wavelength in micrometers
f2 = 1 / lamda  # spatial frequency in micrometer^-1
radius = 50  # radius of the circle where sources are placed
N = 8  # number of point sources

# Generate sources on a circle
angles = np.linspace(0, 2 * np.pi, N, endpoint=False)
sources = [(radius * np.cos(theta), radius * np.sin(theta)) for theta in angles]

# Sum contributions from all sources
Z = np.zeros_like(X)
for i, (x0, y0) in enumerate(sources):
   Z += np.sin(2 * np.pi * f2 * np.sqrt((X - x0) ** 2 + (Y - y0) ** 2))

# Plotting
plt.figure(figsize=(8, 6))
plt.imshow(Z, extent=(x.min(), x.max(), y.max(), y.min()), origin='upper', cmap='YlOrRd')
plt.colorbar(label='Intensity')
plt.title(f"Interference Pattern from {N} Sources on a Circle")
plt.xlabel("x (μm)")
plt.ylabel("y (μm)")
plt.tight_layout()
plt.show()
```

Lens-pyramid system optimization Code:

```
import numpy as np
import matplotlib.pyplot as plt
from scipy.optimize import minimize

# Given experimental data
pitch1 = np.array([2056, 2233, 2473, 2771])  # Lambda (nm)
distance1 = np.array([20, 23, 26, 29])  # x (mm)

# Define the theoretical function for Lambda
def lambda_theoretical(n, x):
   theta_x = 1 / (x ** n)
   return (488 / (2 *np.sin(theta_x)))

# Define the objective function to minimize the sum of absolute differences
def objective(n):
   lambda_model = lambda_theoretical(n, distance1)
   return np.sum(np.abs(lambda_model - pitch1))  # Sum of absolute differences

# Optimize n to best fit the data
result = minimize(objective, x0=[1.5], bounds=[(0.1, 5)])  # Initial guess and reasonable bounds
optimal_n = result.x[0]

# Compute optimized theoretical values
lambda_optimal = lambda_theoretical(optimal_n, distance1)

# Output optimized parameter
optimal_n

print(optimal_n)
```

Bibliography:

[1] S. A. Maier, *Plasmonics: fundamentals and applications*. Springer, 2007.

[2] W. L. Barnes, A. Dereux, and T. W. Ebbesen, "Surface plasmon subwavelength optics," *nature,* vol. 424, no. 6950, pp. 824-830, 2003.

[3] D. Sarid and W. A. Challener, *Modern introduction to surface plasmons: theory, Mathematica modeling, and applications*. Cambridge university press, 2010.

[4] S. Bellucci, O. Vernyhor, A. Bendziak, I. Yaremchuk, V. Fitio, and Y. Bobitski, "Characteristics of the surface plasmon–polariton resonance in a metal grating, as a sensitive element of refractive index change," *Materials,* vol. 13, no. 8, p. 1882, 2020.

[5] Y. Liu, J. Liang, S. Xu, and Y. Geng, "Surface Plasmon Field-Enhanced Raman Scattering Co-Excited by P-Polarized and S-Polarized Light Based on Waveguide-Coupled Surface Plasmon Resonance Configuration," *ACS omega,* vol. 8, no. 44, pp. 41953-41959, 2023.

[6] P. Sarapukdee, D. Schulz, and S. Palzer, "Grating Structures for Silver-Based Surface Plasmon Resonance Sensors with Adjustable Excitation Angle," *Sensors,* vol. 24, no. 14, p. 4538, 2024.

[7] E. Hecht, *Optics*. Pearson Education India, 2012.

[8] H. Xu and B. S. Ham, "Investigation of extraordinary optical transmission and Faraday effect in one-dimensional metallic-magnetic gratings," *Optics express,* vol. 16, no. 26, pp. 21375-21382, 2008.

[9] Z. Huo, Y. Li, B. Chen, W. Zhang, X. Yang, and X. Yang, "Recent advances in surface plasmon resonance imaging and biological applications," *Talanta,* vol. 255, p. 124213, 2023.

[10] J. Ji, Z. Li, W. Sun, and H. Wang, "Surface plasmon resonance tuning in gold film on silver nanospheres through optical absorption," *Sensing and Bio-Sensing Research,* vol. 30, p. 100374, 2020.

[11] M. Naar, Y. Bdour, P. Julien, P. Rochon, and R. G. Sabat, "Enhanced Surface Plasmon Resonance Sensing via Kramers–Kronig Phase Extraction," *Analytical Chemistry,* vol. 96, no. 50, pp. 20033-20038, 2024.

[12] G. Pitruzzello, D. Conteduca, and T. F. Krauss, "Nanophotonics for bacterial detection and antimicrobial susceptibility testing," *Nanophotonics,* vol. 9, no. 15, pp. 4447-4472, 2020.

[13] S. B. Glybovski, S. A. Tretyakov, P. A. Belov, Y. S. Kivshar, and C. R. Simovski, "Metasurfaces: From microwaves to visible," *Physics reports,* vol. 634, pp. 1-72, 2016.

[14] Y. Wang, K. Chen, Y.-S. Lin, and B.-R. Yang, "Plasmonic metasurface with quadrilateral truncated cones for visible perfect absorber," *Physica E: Low-dimensional Systems and Nanostructures,* vol. 139, p. 115140, 2022.

[15] Y. Zhou, Y. Liu, Y. Wang, X. Hu, K. Koh, and H. Chen, "Tunable Au@ SiO2/Au film metasurface as surface plasmon resonance enhancer for direct and ultrasensitive detection of exosomes," *Analytical Chemistry,* vol. 95, no. 25, pp. 9663-9671, 2023.

[16] S. Nair, C. Escobedo, and R. G. Sabat, "Crossed surface relief gratings as nanoplasmonic biosensors," *ACS sensors,* vol. 2, no. 3, pp. 379-385, 2017.

[17] N. Yu and F. Capasso, "Flat optics with designer metasurfaces," *Nature materials,* vol. 13, no. 2, pp. 139-150, 2014.

[18] M. Mazloumi, P. Rochon, and R. Georges Sabat, "Dynamic resonant waveguide crossed gratings for wavelength-selective polarization conversion and optical modulation," *OSA Continuum,* vol. 4, no. 8, pp. 2284-2293, 2021.

[19] L. Qu *et al.*, "Beam shaping by nonlinear moir\'e metasurfaces," *arXiv preprint arXiv:2406.14133,* 2024.

[20] H. Boo, Y. S. Lee, H. Yang, B. Matthews, T. G. Lee, and C. W. Wong, "Metasurface wavefront control for high-performance user-natural augmented reality waveguide glasses," *Scientific reports,* vol. 12, no. 1, p. 5832, 2022.

[21] L. Guarneri, Q. Li, J.-H. Song, M. L. Brongersma, and J. van de Groep, "Exciton-Enhanced Light Scattering in Atomically-Thin Metasurfaces," in *CLEO: QELS_Fundamental Science*, 2022: Optica Publishing Group, p. FM4F. 3.

[22] L. Huang, K. Xu, D. Yuan, J. Hu, X. Wang, and S. Xu, "Sub-wavelength patterned pulse laser lithography for efficient fabrication of large-area metasurfaces," *Nature communications,* vol. 13, no. 1, p. 5823, 2022.

[23] X. Zhang, H. Cai, S. Daqiqeh Rezaei, D. Rosenmann, and D. Lopez, "A universal metasurface transfer technique for heterogeneous integration," *Nanophotonics,* vol. 12, no. 8, pp. 1633-1642, 2023.

[24] J. J. Nivas *et al.*, "Femtosecond laser direct writing of complementary THz metasurfaces using a structured vortex beam," *Optics & Laser Technology,* vol. 181, p. 111831, 2025.

[25] V.-C. Su, C. H. Chu, G. Sun, and D. P. Tsai, "Advances in optical metasurfaces: fabrication and applications," *Optics express,* vol. 26, no. 10, pp. 13148-13182, 2018.

[26] J. G. R. Sereni, "Reference module in materials science and materials engineering," 2016.

[27] R. Lipson and C. Lu, "Photonic crystals: a unique partnership between light and matter," *european journal of physics,* vol. 30, no. 4, p. S33, 2009.

[28] Z. V. Vardeny, A. Nahata, and A. Agrawal, "Optics of photonic quasicrystals," *Nature photonics,* vol. 7, no. 3, pp. 177-187, 2013.

[29] J. D. Joannopoulos, S. G. Johnson, J. N. Winn, and R. D. Meade, "Molding the flow of light," *Princet. Univ. Press. Princeton, NJ [ua],* vol. 12, 2008.

[30] M. Boxer, M. Mazloumi, P. Snell, P. Rochon, and R. G. Sabat, "Large-area photonic crystals, quasicrystals, and Moiré quasicrystals fabricated on azobenzene molecular glass films by pyramidal interference lithography," *Optical Materials Express,* vol. 12, no. 11, pp. 4362-4374, 2022.

[31] A. Akimov, A. Meluchev, D. Kurdyukov, A. Scherbakov, A. Holst, and V. Golubev, "Plasmonic effects and visible light diffraction in three-dimensional opal-metal photonic crystals," *Applied physics letters,* vol. 90, no. 17, 2007.

[32] H. Feng *et al.*, "Gradient nanoplasmonic imaging metasurface for rapid and label-free detection of SARS-CoV-2 sequences," *Talanta,* vol. 278, p. 126533, 2024.

[33] Q. Xu *et al.*, "Plasmonic metalens based on coupled resonators for focusing of surface plasmons," *Scientific Reports,* vol. 6, no. 1, p. 37861, 2016.

[34] M. Virji and A. Stefaniak, "A review of engineered nanomaterial manufacturing processes and associated exposures," 2014.

[35] M. Luo, *Controlling self-assembly and ordering of block polymer nanostructures in thin films*. University of Delaware, 2016.

[36] G. Tadeson and R. G. Sabat, "Enhancement of the power conversion efficiency of organic solar cells by surface patterning of azobenzene thin films," *ACS omega,* vol. 4, no. 26, pp. 21862-21872, 2019.

[37] I. Falcón Casas and W. Kautek, "Subwavelength nanostructuring of gold films by apertureless scanning probe lithography assisted by a femtosecond fiber laser oscillator," *Nanomaterials,* vol. 8, no. 7, p. 536, 2018.

[38] M. Mazloumi and R. G. Sabat, "Real-time imaging of plasmonic concentric circular gratings fabricated by lens–axicon laser interference lithography," *Micromachines,* vol. 14, no. 11, p. 1981, 2023.

[39] M. Mazloumi, E. Dawson, and R. G. Sabat, "Hierarchical concentric surface patterns and metasurfaces on azobenzene molecular glass films using axicon interference lithography," *Optical Materials,* vol. 136, p. 113428, 2023.

[40] U. Bog, K. Huska, F. Maerkle, A. Nesterov-Mueller, U. Lemmer, and T. Mappes, "Design of plasmonic grating structures towards optimum signal discrimination for biosensing applications," *Optics express,* vol. 20, no. 10, pp. 11357-11369, 2012.

[41] J. Homola, S. S. Yee, and G. Gauglitz, "Surface plasmon resonance sensors," *Sensors and actuators B: Chemical,* vol. 54, no. 1-2, pp. 3-15, 1999.

[42] N.-F. Chiu, S.-Y. Nien, C. Yu, J.-H. Lee, and C.-W. Lin, "Advanced metal nanostructure design for surface plasmon photonic bandgap biosensor device," in *2006 International Conference of the IEEE Engineering in Medicine and Biology Society*, 2006: IEEE, pp. 6521-6524.

[43] E. G. Loewen and E. Popov, *Diffraction gratings and applications*. CRC Press, 2018.

[44] V. Biswas and R. Vijaya, "Multi-modal flexible and inexpensive plasmonic metasurface for wide range of refractive index sensing," *Journal of Physics: Photonics,* vol. 6, no. 4, p. 045004, 2024.

[45] A. Pors and S. I. Bozhevolnyi, "Plasmonic metasurfaces for efficient phase control in reflection," *Optics express,* vol. 21, no. 22, pp. 27438-27451, 2013.

[46] A. Pahuja, M. S. Parihar, and D. Kumar, "Performance enhancement of thin film solar cell using two-dimensional plasmonic grating in rear electrode," *IEEE Transactions on Nanotechnology,* vol. 18, pp. 626-634, 2019.

[47] A. Prasad, J. Choi, Z. Jia, S. Park, and M. R. Gartia, "Nanohole array plasmonic biosensors: Emerging point-of-care applications," *Biosensors and Bioelectronics,* vol. 130, pp. 185-203, 2019.

[48] R. F. Balderas-Valadez and C. Pacholski, "Plasmonic nanohole arrays on top of porous silicon sensors: a win–win situation," *ACS applied materials & interfaces,* vol. 13, no. 30, pp. 36436-36444, 2021.

[49] Y. Bdour, C. Escobedo, and R. G. Sabat, "Wavelength-selective plasmonic sensor based on chirped-pitch crossed surface relief gratings," *Optics express,* vol. 27, no. 6, pp. 8429-8439, 2019.

[50] E. Bailey and R. G. Sabat, "Surface plasmon bandwidth increase using chirped-pitch linear diffraction gratings," *Optics express,* vol. 25, no. 6, pp. 6904-6913, 2017.

[51] P. Barman *et al.*, "Nonlinear optical signal generation mediated by a plasmonic azimuthally chirped grating," *Nano Letters,* vol. 22, no. 24, pp. 9914-9919, 2022.

[52] A. B. Taylor and P. Zijlstra, "Single-molecule plasmon sensing: current status and future prospects," *ACS sensors,* vol. 2, no. 8, pp. 1103-1122, 2017.

[53] X. Liu *et al.*, "Rapid wavelength interval selection technology for multi-channel intensity-interrogation surface plasmon resonance imaging sensing," *Applied Physics Letters,* vol. 125, no. 16, 2024.

[54] A. M. Shaltout, V. M. Shalaev, and M. L. Brongersma, "Spatiotemporal light control with active metasurfaces," *Science,* vol. 364, no. 6441, p. eaat3100, 2019.

[55] Y. Zhao *et al.*, "Mechanically reconfigurable metasurfaces: fabrications and applications," *npj Nanophotonics,* vol. 1, no. 1, p. 16, 2024.

[56] H. Yoo *et al.*, "Switching on versatility: recent advances in switchable plasmonic nanostructures," *Small Science,* vol. 3, no. 10, p. 2300048, 2023.

[57] Y. Liu and X. Zhang, "Metamaterials: a new frontier of science and technology," *Chemical Society Reviews,* vol. 40, no. 5, pp. 2494-2507, 2011.

[58] G. Lee, B. Son, D. K. Ko, S. M. Hong, S. Lee, and J. H. Jang, "Plasmonic grating assisted photo-absorption enhancement in terahertz photoconductive antenna," *Microwave and Optical Technology Letters,* vol. 65, no. 3, pp. 887-891, 2023.

[59] C. J. Barrett, J.-i. Mamiya, K. G. Yager, and T. Ikeda, "Photo-mechanical effects in azobenzene-containing soft materials," *Soft matter,* vol. 3, no. 10, pp. 1249-1261, 2007.

[60] N. S. Yadavalli, M. Saphiannikova, and S. Santer, "Photosensitive response of azobenzene containing films towards pure intensity or polarization interference patterns," *Applied Physics Letters,* vol. 105, no. 5, 2014.

[61] V. M. Kryshenik, Y. M. Azhniuk, and V. S. Kovtunenko, "All-optical patterning in azobenzene polymers and amorphous chalcogenides," *Journal of Non-Crystalline Solids,* vol. 512, pp. 112-131, 2019.

[62] B. Eynon and B. Wu, *Photomask fabrication technology*. McGraw-Hill, Inc., 2005.

[63] C. J. Barrett, A. L. Natansohn, and P. L. Rochon, "Mechanism of optically inscribed high-efficiency diffraction gratings in azo polymer films," *The Journal of Physical Chemistry,* vol. 100, no. 21, pp. 8836-8842, 1996.

[64] Y. S. Tan, H. Liu, Q. Ruan, H. Wang, and J. K. Yang, "Plasma-assisted filling electron beam lithography for high throughput patterning of large area closed polygon nanostructures," *Nanoscale,* vol. 12, no. 19, pp. 10584-10591, 2020.

[65] S. Liu *et al.*, "Multiscale fabrication of integrated photonic chips by electron beam lithography," in *10th International Symposium on Advanced Optical Manufacturing and Testing Technologies: Advanced and Extreme Micro-Nano Manufacturing Technologies*, 2021, vol. 12073: SPIE, pp. 38-45.

[66] C. Peeters *et al.*, "Photon scanning tunneling microscopy of tailor-made photonic structures," *Applied physics letters,* vol. 77, no. 1, pp. 142-144, 2000.

[67] S. Zhang *et al.*, "Fabrication of two-dimensional photonic crystal by soft lithography and measure of superprism phenomena," *Laser Physics Letters,* vol. 5, no. 1, pp. 59-62, 2008.

[68] G. Yoon, I. Kim, S. So, J. Mun, M. Kim, and J. Rho, "Fabrication of three-dimensional suspended, interlayered and hierarchical nanostructures by accuracy-improved electron beam lithography overlay," *Scientific reports,* vol. 7, no. 1, p. 6668, 2017.

[69] R. Sidharthan, F. Chollet, and V. Murukeshan, "Periodic patterning using multi-facet prism based laser interference lithography," *Laser physics,* vol. 19, pp. 505-510, 2009.

[70] A. K.-K. Wong, *Resolution enhancement techniques in optical lithography*. SPIE press, 2001.

[71] R. Sidharthan and V. Murukeshan, "Nano-scale patterning using pyramidal prism based wavefront interference lithography," *Physics Procedia,* vol. 19, pp. 416-421, 2011.

[72] M. Vala and J. Homola, "Multiple beam interference lithography: A tool for rapid fabrication of plasmonic arrays of arbitrary shaped nanomotifs," *Optics express,* vol. 24, no. 14, pp. 15656-15665, 2016.

[73] Q. Xie, M. Hong, H. Tan, G. Chen, L. Shi, and T. Chong, "Fabrication of nanostructures with laser interference lithography," *Journal of alloys and compounds,* vol. 449, no. 1-2, pp. 261-264, 2008.

[74] J. Chua and V. Murukeshan, "Patterning of two-dimensional nanoscale features using grating-based multiple beams interference lithography," *Physica Scripta,* vol. 80, no. 1, p. 015401, 2009.

[75] X. Wu, T. T. N. Nguyen, I. Ledoux-Rak, C. T. Nguyen, and N. D. Lai, "Optically Accelerated Formation of One-and Two-Dimensional Holographic Surface Relief," *Holography: Basic Principles and Contemporary Applications,* p. 147, 2013.

[76] J. Wekalao *et al.*, "Metasurface based surface plasmon resonance (SPR) biosensor for cervical cancer detection with behaviour prediction using machine learning optimization based on support vector regression," *Plasmonics,* pp. 1-24, 2024.

[77] W. Liu *et al.*, "Surface plasmon resonance chemical sensor composed of a microstructured optical fiber for the detection of an ultra-wide refractive index range and gas-liquid pollutants," *Optics Express,* vol. 29, no. 25, pp. 40734-40747, 2021.

[78] D. Xia, Q. Zhi, and J. Yang, "Designable optical differential operation based on surface plasmon resonance," *Optics Express,* vol. 30, no. 20, pp. 37015-37025, 2022.

[79] B. Snopok, "Theory and practical application of surface plasmon resonance for analytical purposes," *Theoretical and Experimental Chemistry,* vol. 48, no. 5, pp. 283-306, 2012.

[80] D. J. Griffiths, *Introduction to electrodynamics*. Cambridge University Press, 2023.

[81] A. M. Fox, *Quantum optics: an introduction*. Oxford university press, 2006.

[82] F. L. Pedrotti, L. M. Pedrotti, and L. S. Pedrotti, *Introduction to optics*. Cambridge University Press, 2018.

[83] E. Walla, C. Shaji, R. Vyas, and S. Singh, "Degeneracy in the diffraction of orbital angular momentum carrying beams," *Optics Letters,* vol. 43, no. 23, pp. 5833-5836, 2018.

[84] E. Bailey, "SURFACE PLASMON POLARITON BANDWIDTH INCREASE USING CHIRPED-PITCH LINEAR DIFFRACTION GRATINGS FABRICATED ON AZOBENZENE THIN FILMS," 2017.

[85] H. Faether, "Surface Plasmons on," *Smooth and Rough Surfaces and on Gratings (Springer Tracts in Modem Physics 111,* pp. 642-646, 1988.

[86] M. Vala, J. Dostálek, and J. Homola, "Diffraction grating-coupled surface plasmon resonance sensor based on spectroscopy of long-range and short-range surface plasmons," in *Optical Sensing Technology and Applications*, 2007, vol. 6585: SPIE, pp. 557-565.

[87] P. B. Johnson and R.-W. Christy, "Optical constants of the noble metals," *Physical review B,* vol. 6, no. 12, p. 4370, 1972.

[88] P. E. Ciddor, "Refractive index of air: new equations for the visible and near infrared," *Applied optics,* vol. 35, no. 9, pp. 1566-1573, 1996.

[89] H. H. Solak and C. David, "Patterning of circular structure arrays with interference lithography," *Journal of Vacuum Science & Technology B: Microelectronics and Nanometer Structures Processing, Measurement, and Phenomena,* vol. 21, no. 6, pp. 2883-2887, 2003.

[90] F. Chaussard, H. Rigneault, and C. Finot, "Two-wave interferences space-time duality: Young slits, Fresnel biprism and Billet bilens," *Optics communications,* vol. 397, pp. 31-38, 2017.

[91] B. Edlén, "The refractive index of air," *Metrologia,* vol. 2, no. 2, p. 71, 1966.

[92] O. Svelto, "Properties of laser beams," in *Principles of Lasers*: Springer, 2009, pp. 475-504.

[93] S. Lea, *Mathematics for physicists*. Brooks/Cole-Thomson Learning Belmont, CA, 2004.

[94] F. Aloui, L. Lecamp, P. Lebaudy, and F. Burel, "Refractive index evolution of various commercial acrylic resins during photopolymerization," *Express Polymer Letters,* vol. 12, no. 11, pp. 966-971, 2018.

[95] V. Perlick, *Ray optics, Fermat's principle, and applications to general relativity*. Springer Science & Business Media, 2000.

[96] R. Kirby, R. G. Sabat, J.-M. Nunzi, and O. Lebel, "Disperse and disordered: a mexylaminotriazine-substituted azobenzene derivative with superior glass and surface relief grating formation," *Journal of Materials Chemistry C,* vol. 2, no. 5, pp. 841-847, 2014.

[97] M. Dollar, Y. Bdour, P. Rochon, and R. G. Sabat, "Surface Plasmon Mediated Angular and Wavelength Tunable Retroreflectors Using Parallel-Superimposed Surface Relief Bi-Gratings," *Applied Sciences,* vol. 15, no. 1, p. 339, 2025.

[98] Y. Bdour and R. G. Sabat, "Real-Time Plasmonic Strain Sensors Based on Surface Relief Diffraction Gratings," *Micromachines,* vol. 15, no. 7, p. 863, 2024.

[99] A. Natansohn and P. Rochon, "Photoinduced motions in azo-containing polymers," *Chemical reviews,* vol. 102, no. 11, pp. 4139-4176, 2002.

[100] C. Cojocariu and P. Rochon, "Light-induced motions in azobenzene-containing polymers," *Pure and applied chemistry,* vol. 76, no. 7-8, pp. 1479-1497, 2004.

[101] C. Su, "Mapping quantitative mechanical properties at molecular scale using peak force tapping AFM," *Microscopy and Microanalysis,* vol. 16, no. S2, pp. 364-365, 2010.

[102] A. Smith, M. Mazloumi, L. Karperien, C. Escobedo, and R. G. Sabat, "Learning from Nature: Fighting Pathogenic Escherichia coli Bacteria Using Nanoplasmonic Metasurfaces," *Advanced Materials Interfaces,* vol. 10, no. 21, p. 2300269, 2023.

[103] E. Dawson, A. Novikova, Y. Bdour, and R. G. Sabat, "Surface plasmon resonance excitation and imaging in circular gratings: a study of non-polarized, radial and azimuthal polarization effects," *Journal of Physics D: Applied Physics,* vol. 58, no. 12, p. 125106, 2025.

[104] A. Samusev *et al.*, "Polarization-resolved characterization of plasmon waves supported by an anisotropic metasurface," *Optics Express,* vol. 25, no. 26, pp. 32631-32639, 2017.

[105] S. S. Kruk *et al.*, "Polarization properties of optical metasurfaces of different symmetries," *Physical Review B,* vol. 91, no. 19, p. 195401, 2015.

[106] L. Luo, S. Shan, and X. Li, "A review: Laser interference lithography for diffraction gratings and their applications in encoders and spectrometers," *Sensors,* vol. 24, no. 20, p. 6617, 2024.

[107] Q. Yang *et al.*, "Near-field surface plasmons on quasicrystal metasurfaces," *Scientific Reports,* vol. 6, no. 1, p. 26, 2016.

[108] N. Wang, H. Chen, and K. Kuo, "Two-dimensional quasicrystal with eightfold rotational symmetry," *Physical review letters,* vol. 59, no. 9, p. 1010, 1987.

[109] B. Cheng, Z. Jiang, Y. Zou, and G. Song, "A Highly Efficient Plasmonic Polarization Conversion Metasurface Supporting a Large Angle of Incidence," *Crystals,* vol. 14, no. 8, p. 694, 2024.

[110] E. Jones, T. Oliphant, and P. Peterson, "Optimization and root finding(scipy. optimize)," *SciPy. org,* pp. 1-8, 2018.

[111] J. H. Mathews and K. D. Fink, *Numerical methods using MATLAB*. Pearson prentice hall Upper Saddle River, NJ, 2004.

[112] S. H. Huang, J. Li, Z. Fan, R. Delgado, and G. Shvets, "Monitoring the effects of chemical stimuli on live cells with metasurface-enhanced infrared reflection spectroscopy," *Lab on a Chip,* vol. 21, no. 20, pp. 3991-4004, 2021.

[113] Yakubovsky, D. I., Arsenin, A. V., Stebunov, Y. V., Fedyanin, D. Y., & Volkov, V. S. (2017). Optical constants and structural properties of thin gold films. *Optics express*, *25*(21), 25574-25587.

[114] ThorLabs, I. (2024). Thorlabs. *ThorLab, Inc.,[Online]. Available: https://www.thorlabs.com/newgrouppage9.cfm?objectgroup_id=9301*.

[115] Rossi, S., Gazzola, E., Capaldo, P., Borile, G., & Romanato, F. (2018). Grating-coupled surface plasmon resonance (GC-SPR) optimization for phase-interrogation biosensing in a microfluidic chamber. *Sensors*, *18*(5), 1621.